UNIVERSITY OF CALIFORNIA SAN DIEGO

Mapping subsurface processes to surface expressions: geophysical observations and analyses for policy and science development

A dissertation submitted in partial satisfaction of the
requirements for the degree
Doctor of Philosophy

in

Earth Sciences

by

Wesley Randall Neely

Committee in charge:

Adrian A. Borsa, Chair
Jennifer A. Burney
Daniel R. Cayan
Morgan C. Levy
David T. Sandwell

2021

The dissertation of Wesley Randall Neely is approved, and it is acceptable in quality and form for publication on microfilm and electronically.

University of California San Diego

2021

EPIGRAPH

If there is magic on this planet, it is contained in water.

– Loren Eiseley

TABLE OF CONTENTS

LIST OF FIGURES

LIST OF TABLES

ACKNOWLEDGEMENTS

Given the choice between the truth and lies, it is my belief that the former is always preferable. And the truth is that this dissertation would not have been possible without all the amazing and encouraging people I have had the fortune to know. I will forever be indebted to them for the guidance and support they gave me while undertaking this endeavor.

First, I must thank my advisor, Adrian Borsa. Adrian's raw enthusiasm and excitement for science generates a sense of unexplored possibility just waiting to be tapped. After talking with him, I felt as if nothing was too unobtainable and only too eager to try. He always has time to talk about work, life, and everything in between. Thank you Adrian for indulging every "one more thing" I had and being the best mentor I could have ever wished for. I also thank my doctoral committee – Jennifer Burney, Daniel Cayan, Morgan Levy, and David Sandwell. Likewise to Adrian, Jen makes science fun and instills confidence. She is always full of good ideas and possible research directions. Dan has a wide knowledge range which allows him to "know enough to be dangerous". He has motivated me to broaden my perspective through his many probing questions. Morgan knows how to take an idea and run with it. Her interdisciplinary approach has already proven the value of my geodetic datasets for policy and management applications. David is an impressive force in the geodetic community. Both his technical and institutional knowledge have been invaluable to my development and what I have been able to accomplish.

I also need to thank both academic and administrative staff at IGPP and SIO. Classes with Duncan Agnew, Adrian Borsa, Cathy Constable, Yuri Fialko, Helen Fricker, Guy Masters, Davie Sandwell, Peter Shearer, and Dave Stegman provided me with the foundational knowledge of geophysics required to be a well-rounded geophysicist. Thank you NetOps (Wayne C., Andrew, Paul, Jeff), IGPP (Wanye F., Iris, Megan Strachan, Megan Smith, Maria, Victoria, and Chris C.), SIO communications (Lauren, Robert, Chase, and Brittany), and the SIO department (Denise, Josh, Shelley, Gilbert, Maureen, and Tim) that facilitated every last minute request I had and enabled me to present my work across the world. Here, I would also like to acknowledge my undergraduate advisor at UT Austin, Clark Wilson. Thank you for bringing me into the world of research and guiding me as I applied to graduate school.

Over the years I spent at SIO, I have made many connections and friends. I would like to thank all my collaborators (Adrian, Morgan, Jen, Francesca, Michelle, and Farhood). It has been a pleasure working with you and I hope we can continue to link up on future projects. Thank you to the 2014 cohort (Julia, Yuval, May, Daniel, Marah, and Georgie) for making the first year a blast. I especially want to thank Daniel for being one of my favorite friends at Scripps. While your excellence cut our time short, I had some of the best times climbing and playing tennis with you. I will always value your opinions and only wish the best for you in the future. I also would be remiss without mention of the fabulous officemates I've had over the years. I especially want to thank Katia, Adrian D., Wenyuan, and Dallas for all the antics and wine we have bonded over. To the members of the cohort above me (Jessie, Matt, John, Dara, and

Adrian D.) and below me (Maya, Drake, Chloe, and Susheel), thank you for all the wonderful times that I will cherish forever. Susheel, you are one of the most incredible people I know. Your boundless generosity and always-down-to-do-anything attitude has endeared yourself to me in ways I can never fully express. You are the definition of a true friend. And while I can't list everyone else, despite my best efforts, I want to thank all the postdocs, students, and members of the SIO Basketball league I have overlapped with (especially Nick L., Xiaohua, and Soli).

Finally, I would not be the person I am today without my family and life long friends. Through the ups and downs, you have been there to encourage me and comfort me. To Logan, Brenna, and Trent, thank you for believing in me and being friends with me all this time. To my sister Kelsey, I will always look up to you. You have been a role model to me longer than I can remember (whether I admit it or not). You are one of the most intelligent individuals I know, and I hardly miss an opportunity to take pride of you in front of others. Having a shared experience of navigating graduate school in California with you has truly made the whole process easier. Mom, I don't think I fully understood how exceptional you are until I moved away. Thank you for making me want to be the best version of myself. Your unwavering support and confidence in me is unparalleled. Thank you for all your sacrifices and teaching me to see beauty in the world. I also want to dedicate this dissertation to my dad, who passed away when I was 15. Not a day goes by that I don't think about him. I know he would be proud, and I wish he could be here to see the person I've grown into. Olivia, you are and will forever be my person. Thank you on taking a chance on me and sticking with me all

these years. I know it has not be easy on you and I am infinitely grateful for all your support, advice, and care-giving. I will forever be in awe of your beauty, humor, and drive. You have made me a better person and I cannot wait to spend the rest of my life with you. Lastly, but certainly not least, I thank Olivia's parents (Ed and Kathy) and sister (Marisa) for welcoming me into their family and supporting throughout my graduate studies.

Chapter 2, in full, is a reformatted version of material as it appears in IEEE Transactions on Geoscience and Remote Sensing: Neely, W. R., A. A. Borsa, and F. Silverii (2020), GInSAR: A cGPS Correction for Enhanced InSAR Time Series, *IEEE Transactions on Geoscience and Remote Sensing*, 58(1), 136–146, doi: 10.1109/TGRS.2019.2934118. I was the primary investigator and author of this paper.

Chapter 3, in full, is a reformatted version of material as it appears in Water Resources Research: Neely, W. R., A. A. Borsa, J. A. Burney, M. C. Levy, F. Silverii, and M. Sneed (2021), Characterization of groundwater recharge and flow in California's San Joaquin Valley from InSAR-observed surface deformation, *Water Resources Research*, 57(4), 1–20, doi:10.1029/2020WR028451. I was the primary investigator and author of this paper.

Chapter 4 is an active research project currently being prepared for publication, and is coauthored with Farhood Ensan and Adrian Borsa. I was the primary investigator and author of this research material.

VITA

2021	Ph. D. in Earth Sciences, University of California San Diego
2015	M. S. in Geophysics, University of California San Diego
2014	B. S. with Special Honors in Geophysics, University of Texas at Austin

PUBLICATIONS

Silverii, F., F. Pulvirenti, E. K. Montgomery-Brown, A. A. Borsa, **W. R. Neely** (2021), The 2011-2019 Long Valley Caldera inflation: New insights from separation of superimposed geodetic signals and 3D modeling, *Earth and Planetary Science Letters* 569, 117055, doi:10.1016/j.epsl.2021.117055.

Neely, W. R., A. A. Borsa, J. A. Burney, M. C. Levy, F. Silverii, M. Sneed (2021), Characterization of groundwater recharge and flow in California's San Joaquin Valley from InSAR-observed surface deformation, *Water Resources Research* 57(4), doi:10.1029/2020WR028451.

Levy, M. C., **W. R. Neely**, A. A. Borsa, J. A. Burney (2020), Fine-scale spatiotemporal variation in subsidence across California's San Joaquin Valley explained by groundwater demand, *Environmental Research Letters*, 15(10), 104083, doi:10.1088/1748-9326/abb55c.

Neely, W. R., A. A. Borsa, F. Silverii (2020), GInSAR: A cGPS correction for enhanced InSAR time series, *IEEE Transactions on Geoscience and Remote Sensing*, 58(1), 136–146, doi:10.1109/TGRS.2019.2934118.

ABSTRACT OF THE DISSERTATION

Mapping subsurface processes to surface expressions: geophysical observations and analyses for policy and science development

by

Wesley Randall Neely

Doctor of Philosophy in Earth Sciences

University of California San Diego, 2021

Adrian A. Borsa, Chair

The higher variability of surface-water supplies due to a changing climate has motivated an increased reliance on groundwater for urban, industrial, and agricultural purposes. This is particularly evident in California's San Joaquin Valley (SJV) where overexploitation of the underlying aquifer system threatens the quality and availability of future groundwater resources as well as lead to large magnitude land subsidence impacting critical infrastructure. Direct observation of these reservoirs on policy relevant scales, however, has remained elusive. The three principle chapters of this dissertation

explore the extent to which geodetic tools and data can be used to better characterize regional subsurface processes such as groundwater recharge, flow, and extraction. Chapter 1 provides the motivation of this research and an introduction to the data used in the subsequent chapters. Chapter 2 presents a new methodology for combining interferometric synthetic aperture radar (InSAR) and Global Positioning System (GPS) displacements. Chapter 3 explores the efficacy of seasonal surface displacement time series for characterizing locations of groundwater recharge and flow in the SJV. Chapter 4 describes a method for analyzing networks of groundwater level records and how they relate to an extension of Chapter 3 results.

Chapter 1

Introduction

1.1 Motivation

The story of life on Earth could not be told without mention of water. So critical is water for all organisms, more so than any other ingredient, it is the basis for life as we know it. Whether in the form of ice, liquid, or vapor, our planet's surface is mostly covered or underlain with this resource. While seemingly ubiquitous, less than a hundredth of a percent is non-saline and readily accessible (*Shiklomanov*, 1993). Limited by this access, the human species need for potable water directly influenced the development of civilizations, culture, and interactions with the environment (*Yevjevich*, 1992).

Our uses for water range from drinking to agriculture to sanitation to energy production. The presence of water (or the lack thereof) has influenced local to global transportation networks, determined the location of population centers, and played significant roles in major religions (*Conners*, 2013). With so many systems relying on

certain levels of water resources, extremes in availability can have harmful impacts. Droughts can disrupt food and energy production (*Below et al.*, 2007), limit the efficiency of shipping channels (*Carse*, 2017), and lead to losses on export/import earnings (*Benson and Clay*, 1998). On the other end of the spectrum, too much water may result in natural disasters such as flooding which similarly can have devastating social, economic, and environmental impacts. While these phenomena have always presented threats, changes in global climate can exacerbate their effects and may make their occurrence more frequent (*Van Aalst*, 2006).

In order to mitigate the effects of water variability, humankind has developed a range of technologies to control and store water resources. So important is a stable supply of water that it's likely that the earliest engineering accomplishments were systems of water conveyance and storage (*Conners*, 2013). From the ancient canals and dams in Egypt and Mesopotamia to the Roman aqueducts to complex systems of cisterns in northern India, humans have been adapting to their environments and ensuring they have access to water since the Neolithic era (*Galili and Nir*, 1993). A key component of this adaptation has been the utilization of groundwater resources.

Groundwater is the largest source of freshwater resources excluding glaciers and ice caps (*Shiklomanov*, 1993). A subsurface region of sufficient permeability (ability to transmit a fluid) and porosity (ratio of open space in the host material) to support a usable supply of groundwater is referred to as an aquifer. Aquifer systems are fairly ubiquitous and often considered a "stable" source of water to be used when demand cannot be met by surface water alone. Globally, groundwater accounts for roughly a third

of all freshwater withdrawals (*Taylor et al.*, 2013). With a growing global population (projected to rise to 9.7 billion by 2050 (*United Nations et al.*, 2019)) and more variable surface water supplies due to climate change, increased importance will likely fall on groundwater resources (*Hanson et al.*, 2012). While previously thought that these reservoirs were near inexhaustible, their limits are now in sight and action to monitor and protect these resources need to be taken. Overexploitation of aquifer systems may lead to irreversible damage, threatening these water sources for future use (*Scanlon et al.*, 2012). Improved monitoring, characterization, and management of aquifer systems need to be developed in order to balance the water needs of today with the protection for use in the generations to come.

1.2 Tools for Groundwater Monitoring

Despite so much reliance on these resources, the state of aquifer systems remains relatively unknown. Aquifer systems can be challenging to efficiently and synoptically monitor due in part to the large spatial extent they can span (up to hundreds of thousands of square kilometers (*McGuire*, 2017)) and because they are hidden underground. However, there are tools and techniques that can be used to better understand these systems. Briefly, the advantages and disadvantages of a few of these methods are outlined below.

Monitoring wells provide a direct measurement of groundwater levels and are used extensively in groundwater management (*Kim et al.*, 2020). However, a single well

can be costly to install and only samples at the station location and perforation depth. Additionally, many of these wells need to be physically sampled, reducing the temporal resolution to often just a few times a year. For large aquifer systems that are heterogeneous both laterally and vertically, the utility of these wells may be limited. In addition to providing direct estimates of groundwater levels, the drilling of the well allows for hydrostratigraphic characterization via well completion records and induction electrical logs. Well completion records typically provide descriptions of the subsurface material with depth. They must be used with caution as they are subject to interpretation by the person providing the description and are often times very general. Electrical logs make use of the relationship between a material's composition and how well that material conducts an electrical current (*Conners*, 2013). With electrical logs, one can have a near continuous record of resistivity with depth which can suggest not only the type of material but also the percentage of water content. Completion records and electrical records can provide a much better understanding of the underlying lithology when used together rather than individually, though as with groundwater level data, they are limited to the locations of the stations.

Imaging techniques can provide much higher spatial resolution than *in-situ* observations. These techniques include but are not limited to electromagnetic (EM) methods, seismic surveying, and ground penetrating radar. EM methods, whether airborne or terrestrial, map out the electrical resistivity of the subsurface which can be used to determine the underlying sediment type. This technique works by transmitting a primary magnetic field that generates eddy currents at various depths in the subsurface

which consequently produce secondary magnetic fields that are recorded by a receiver (*Kirsch*, 2009). Magnetic data can then be inverted for resistivity and subsequently sediment type. Airborne EM surveying can have a vertical resolution on the order of meters and extend to depths of 500 m (*Knight et al.*, 2018) while towed systems only extend to depths of 10s of meters. Lateral resolution depends on the survey design and system type but can span 10s of meters to kilometers. Alternatively, seismic methods make use of acoustic sources of energy. Vibrations sent into the earth reflect (bounce) or refract (bend) as they travel through the subsurface. These vibrations are then recorded at strategically placed geophones which can then be used to map out subsurface structure. Seismic methods tend to have higher structural resolution and penetration depth than EM techniques but at greater acquisition and interpretation costs (*Kirsch*, 2009). Ground penetrating radar makes use of the reflection of electromagnetic waves, similar to seismic techniques, to map out subsurface structure based on variations in the electrical properties. These surveys are generally higher resolution but limited in depth. For all the various imaging techniques, they are constrained by the survey design and can be costly to operate.

Variations in mass related to groundwater extraction or recharge can also be measured by repeat microgravity surveys and, if a large enough signal, by satellite gravimetry. Microgravity surveys use relative and/or absolute gravimeters to estimate local groundwater storage and specific yield (*Pool and Eychaner*, 1995; *Gehman et al.*, 2009). However, these instruments can be expensive and require delicate care in order to obtain quality measurements. Like other pointwise measurements these studies are

often limited in scope and temporal frequency. The Gravity Recovery and Climate Experiment (GRACE) satellites (as well as the GRACE Follow-On mission) ushered us into a new age of global hydrological observation. These pair of low orbit ($\sim$ 400 km) twin satellites use microwave k-band ranging technology to precisely measure the along-track distance between each other as the trailing satellite "chases" the leading satellite (average separation of $\sim$ 200km) (*Tapley et al.*, 2004). Changes in this distance are then mapped to gravitational anomalies on/in the Earth. While these missions provide regular estimates of regional to global scale mass changes, they lack the fine spatial resolution needed to understand the heterogeneity of aquifer systems.

Changes in groundwater can also induce surface displacements. Data from continuous Global Positioning System (GPS) networks and interferometric synthetic aperture radar (InSAR) can detect this motion at sub-centimeter precision. GPS uses a constellation of satellites which transmit radio signals encoded with a precise time. Ground receivers coupled to the Earth's surface take the satellite signal and compute the time difference relative to its local clock. These differences are then used to determine the range between the satellites and receiver and thus the change in position through time. Using the positioning, surface motion related to geophysical processes can be estimated at frequent intervals (daily or better)(*Bock and Melgar*, 2016). However, the spatial resolution is limited to the station spacing (often 10s of km for a "dense" network). InSAR makes use of the difference in the carrier signal phase to estimate relative displacements over wide areas between two synthetic aperture radar (SAR) images (*Massonnet and Feigl*, 1998). Using a suite of these differences, referred to as interferograms, a time

series of surface displacements can be constructed (*Berardino et al.*, 2002). While there are different modes of SAR acquisitions, many missions offer images 100s of km wide allowing for large spatial coverage and spatial resolution on the order of 10s of meters. While revisit times are not as frequent as GPS sampling, missions such as Sentinel-1A/B have repeat intervals as little as 6 days (*Torres et al.*, 2012). Displacements can reflect either or a combination of elastic loading and poroelastic effects. In the case of elastic loading, variations in surface loads (or near surface loads) induce instantaneous displacements related to elastic deformation (*Farrell*, 1972). For example, the addition of mass during wet periods (i.e. increases in water volumes) depresses the solid earth. During dry periods, the solid earth rebounds as water is removed (*Borsa et al.*, 2014). Using this principle, the volume of water change can be "weighed" using surface displacements. This has been proven to work well and is consistent with mass change observations from GRACE (*Adusumilli et al.*, 2019). Conversely the land surface can move via poroelastic displacements. Changes in groundwater levels can increase or decrease pore pressure leading to uplift or subsidence (*Poland and Davis*, 1969) and is described in more detail below (Section 1.3). This process responds inversely to elastic loading effects and can be orders of magnitude larger (*Argus et al.*, 2017). This relationship has been used to estimate aquifer parameters and loss of groundwater storage (*Ojha et al.*, 2018; *Smith et al.*, 2017). However, it is important to remember that surface displacements can be a combination of hydrologic, volcanic, and tectonic processes and that they represent integrated effects (*Silverii et al.*, 2021).

1.3 Link between Surface Motion and Groundwater changes

For confined aquifer systems, we generally assess groundwater through hydraulic head, a measurement of liquid pressure relative to a vertical datum. Changes in hydraulic head may induce aquifer system compaction or expansion. This is based on the relationship between pore pressure and effective stress which can be described following the Principle of Effective Stress (*Terzaghi*, 1925)

$$\sigma_e = \sigma_T - P_p \tag{1.1}$$

where σ_e is the effective stress, σ_T is the total stress, and P_p is the pore pressure. As the total stress is related to the overburden weight and is assumed constant for confined systems, we can express changes in effective stress as

$$\Delta\sigma_e = -\Delta P_p = -\rho_w g \Delta h \tag{1.2}$$

where ρ_w is the density of water, g is the gravitational constant, and h is the hydraulic head. Using the expression for specific storage, S_s, which relates the volume of water produced for a aquifer system volume and change in head (*Jacob*, 1940), we can begin to describe the link between head and ground deformation. S_s can take the form of

$$S_s = S_{sk} + S_{sf} = \rho_w g(\alpha + \eta\beta) \tag{1.3}$$

where S_{sk} is the skeletal-specific storage, S_{sf} is related to the deformation of the fluid to a change in effective stress. η is the porosity, β is the compressibility of the fluid, and α is the compressibility of the sediment (or aquifer skeleton). α can be described by the ratio of vertical strain to effective stress

$$\alpha = \frac{-\Delta b}{\Delta \sigma_e b_0} \tag{1.4}$$

where Δb is the change in volume thickness for an initial thickness b_0. Assuming that the component of deformation related to the compressibility of water is negligible, we can combine equations 1.2 and 1.4 to demonstrate the link between head and deformation

$$S_{sk} b_0 = S_k = \frac{\Delta b}{\Delta h} \tag{1.5}$$

where S_k is the skeletal storage coefficient. Further, S_k is the sum of the inelastic and elastic coefficients

$$S_k = S_{kv} + S_{ke} \tag{1.6}$$

where S_{kv} and S_{ke} the inelastic and elastic skeletal storage coefficients, respectively. It is generally assumed that this poroelastic deformation behaves inelastically (i.e. permanent deformation) whenever the effective stress, σ_e, exceeds the preconsolidation stress, typically taken to be the lowest previous hydraulic head. This type of deformation results from the realignment of the grains constituting the aquifer system skeletal matrix with reduced capacity for water storage (*Leake*, 1990). This is more typical for fine grained

deposits such as clay and silt, resulting in permanent land subsidence. Changes in pore pressure that do not lead to the effect stress exceeding preconsolidation stress manifest as elastic deformation (i.e., reversible deformation) in the form of land subsidence or uplift (Figure 1.1).

1.4 Dissertation Structure

This dissertation describes the improvement and use of geodetic observations from satellite radar and Global Positioning System stations for better observing and characterizing surface displacements as they relate to groundwater changes using California's San Joaquin Valley as a case study. This dissertation is structured as follows. The three principal Chapters (2 through 4) were originally written for individual publication and can be read independently. In Chapter 2 (*Neely et al.*, 2020), I present a method for correcting long spatial wavelength error in InSAR data using GPS time series data. I also detail a new method for InSAR time series inversion that retains more data coverage than traditional algorithms. In Chapter 3 (*Neely et al.*, 2021), I use combined InSAR and GPS observations to characterize seasonal surface displacements over the San Joaquin Valley for the dry 2016 and wet 2017 water years. Finally, chapter 4 focuses on the potential application of a state-wide network of monitoring wells to assess monthly and seasonal conditions of groundwater levels and how they relate to the displacement record.

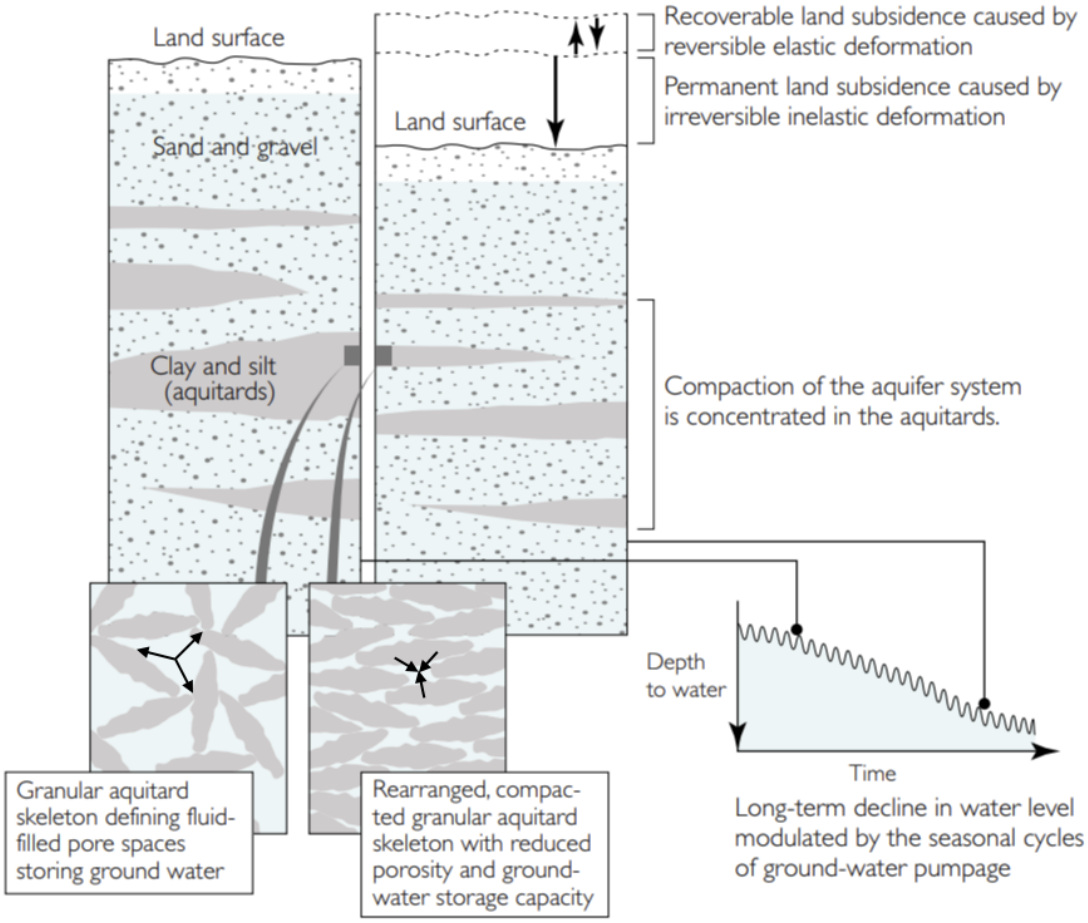

Figure 1.1: Diagram of land surface deformation over an alluvial sediment aquifer system in response to changes in pore pressure. Clay and silt packages (aquitards) are more susceptible to the permanent rearrangement (inelastic deformation) of grain alignment through compaction. Changes in pore pressure that do not exceed the preconsolidation stress result in reversible deformation. Image modified from *Galloway et al.* (1999).

References

Adusumilli, S., A. A. Borsa, M. A. Fish, H. K. McMillan, and F. Silverii (2019), A Decade of Water Storage Changes Across the Contiguous United States From GPS and Satellite Gravity, *Geophysical Research Letters*, *46*(22), 13,006–13,015, doi:10.1029/2019GL085370.

Argus, D. F., Landerer Felix W., Wiese David N., Martens Hilary R., Fu Yuning, Famiglietti James S., Thomas Brian F., Farr Thomas G., Moore Angelyn W., and Watkins Michael M. (2017), Sustained Water Loss in California's Mountain Ranges During Severe Drought From 2012 to 2015 Inferred From GPS, *Journal of Geophysical Research: Solid Earth*, *122*(12), 10,559–10,585, doi:10.1002/2017JB014424.

Below, R., E. Grover-Kopec, and M. Dilley (2007), Documenting Drought-Related Disasters: A Global Reassessment, *The Journal of Environment & Development*, *16*(3), 328–344, doi:10.1177/1070496507306222.

Benson, C., and E. J. Clay (1998), *The impact of drought on Sub-Saharan African economies: a preliminary examination*, no. 401 in World Bank technical paper, World Bank, Washington, D.C.

Berardino, P., G. Fornaro, R. Lanari, and E. Sansosti (2002), A new algorithm for surface deformation monitoring based on small baseline differential SAR interferograms, *IEEE Transactions on Geoscience and Remote Sensing*, *40*(11), 2375–2383, doi:10.1109/TGRS.2002.803792.

Bock, Y., and D. Melgar (2016), Physical applications of GPS geodesy: a review, *Reports on Progress in Physics*, *79*(10), 106,801, doi:10.1088/0034-4885/79/10/106801.

Borsa, A. A., D. C. Agnew, and D. R. Cayan (2014), Ongoing drought-induced uplift in the western United States, *Science*, *345*(6204), 1587–1590, doi:10.1126/science.1260279.

Carse, A. (2017), An infrastructural event: Making sense of Panama's drought, *Water Alternatives*, *10*(3), 888.

Conners, J. A. (2013), *Groundwater for the 21st century: a primer for citizens of planet earth*, McDonald & Woodward Pub. Co, Granville, Ohio.

Farrell, W. E. (1972), Deformation of the Earth by surface loads, *Reviews of Geophysics*, *10*(3), 761–797, doi:10.1029/RG010i003p00761.

Galili, E., and Y. Nir (1993), The submerged Pre-Pottery Neolithic water well of Atlit-Yam, northern Israel, and its palaeoenvironmental implications, *The Holocene*, *3*(3), 265–270, doi:10.1177/095968369300300309.

Galloway, D. L., D. R. Jones, and S. E. Ingebritsen (Eds.) (1999), *Land subsidence in the United States*, no. 1182 in U.S. Geological Survey circular, U.S. Geological Survey, Reston, VA.

Gehman, C. L., D. L. Harry, W. E. Sanford, J. D. Stednick, and N. A. Beckman (2009), Estimating specific yield and storage change in an unconfined aquifer using temporal gravity surveys, *Water Resources Research*, *45*(4), doi:10.1029/2007WR006096.

Hanson, R. T., L. E. Flint, A. L. Flint, M. D. Dettinger, C. C. Faunt, D. Cayan, and W. Schmid (2012), A method for physically based model analysis of conjunctive use in response to potential climate changes, *Water Resources Research*, *48*(6), W00L08, doi:10.1029/2011WR010774.

Jacob, C. E. (1940), On the flow of water in an elastic artesian aquifer, *Eos, Transactions American Geophysical Union*, *21*(2), 574–586, doi:10.1029/TR021i002p00574.

Kim, K. H., Z. Liu, M. Rodell, H. Beaudoing, E. Massoud, J. Kitchens, M. Dudek, P. Saylor, F. Corcoran, and J. T. Reager (2020), An Evaluation of Remotely Sensed and In Situ Data Sufficiency for SGMA-Scale Groundwater Studies in the Central Valley, California, *JAWRA Journal of the American Water Resources Association*, doi:https://doi.org/10.1111/1752-1688.12898.

Kirsch, R. (Ed.) (2009), *Groundwater geophysics: a tool for hydrogeology*, 2nd ed., Springer, Berlin.

Knight, R., R. Smith, T. Asch, J. Abraham, J. Cannia, A. Viezzoli, and G. Fogg (2018), Mapping Aquifer Systems with Airborne Electromagnetics in the Central Valley of California, *Groundwater*, *56*(6), 893–908, doi:https://doi.org/10.1111/gwat.12656.

Leake, S. A. (1990), Interbed storage changes and compaction in models of regional groundwater flow, *Water Resources Research*, *26*(9), 1939–1950, doi:10.1029/WR026i009p01939.

Massonnet, D., and K. L. Feigl (1998), Radar interferometry and its application to changes in the Earth's surface, *Reviews of Geophysics*, *36*(4), 441–500, doi:10.1029/97RG03139.

McGuire, V. L. (2017), Water-level and recoverable water in storage changes, High Plains aquifer, predevelopment to 2015 and 2013–15, *USGS Numbered Series 2017-5040*, U.S. Geological Survey, Reston, VA.

Neely, W. R., A. A. Borsa, and F. Silverii (2020), GInSAR: A cGPS Correction for Enhanced InSAR Time Series, *IEEE Transactions on Geoscience and Remote Sensing*, *58*(1), 136–146, doi:10.1109/TGRS.2019.2934118.

Neely, W. R., A. A. Borsa, J. A. Burney, M. C. Levy, F. Silverii, and M. Sneed (2021), Characterization of Groundwater Recharge and Flow in California's San Joaquin Valley From InSAR-Observed Surface Deformation, *Water Resources Research*, *57*(4), e2020WR028,451, doi:https://doi.org/10.1029/2020WR028451.

Ojha, C., M. Shirzaei, S. Werth, D. F. Argus, and T. G. Farr (2018), Sustained Groundwater Loss in California's Central Valley Exacerbated by Intense Drought Periods, *Water Resources Research*, *54*(7), 4449–4460, doi:10.1029/2017WR022250.

Poland, J. F., and G. H. Davis (1969), Land Subsidence Due To Withdrawal Of Fluids, in *Reviews in Engineering Geology*, vol. 2, pp. 187–270, Geological Society of America, doi:10.1130/REG2-p187.

Pool, D. R., and J. H. Eychaner (1995), Measurements of Aquifer-Storage Change and Specific Yield Using Gravity Surveys, *Ground Water*, *33*(3), 425–432, doi:10.1111/j.1745-6584.1995.tb00299.x.

Scanlon, B. R., C. C. Faunt, L. Longuevergne, R. C. Reedy, W. M. Alley, V. L. McGuire, and P. B. McMahon (2012), Groundwater depletion and sustainability of irrigation in the US High Plains and Central Valley, *Proceedings of the National Academy of Sciences*, *109*(24), 9320–9325, doi:10.1073/pnas.1200311109.

Shiklomanov, I. (1993), World fresh water resources, in *Water in Crisis: A Guide to the World's Fresh Water Resources*, Oxford University Press.

Silverii, F., F. Pulvirenti, E. K. Montgomery-Brown, A. A. Borsa, and W. R. Neely (2021), The 2011-2019 Long Valley Caldera inflation: New insights from separation of superimposed geodetic signals and 3D modeling, *Earth and Planetary Science Letters*, *569*, 117,055, doi:10.1016/j.epsl.2021.117055.

Smith, R. G., R. Knight, J. Chen, J. A. Reeves, H. A. Zebker, T. Farr, and Z. Liu (2017), Estimating the permanent loss of groundwater storage in the southern San Joaquin Valley, California, *Water Resources Research*, *53*(3), 2133–2148, doi:10.1002/2016WR019861.

Tapley, B. D., S. Bettadpur, J. C. Ries, P. F. Thompson, and M. M. Watkins (2004), GRACE Measurements of Mass Variability in the Earth System, *Science*, *305*(5683), 503–505, doi:10.1126/science.1099192.

Taylor, R. G., B. Scanlon, P. Döll, M. Rodell, R. van Beek, Y. Wada, L. Longuevergne, M. Leblanc, J. S. Famiglietti, M. Edmunds, L. Konikow, T. R. Green, J. Chen, M. Taniguchi, M. F. P. Bierkens, A. MacDonald, Y. Fan, R. M. Maxwell, Y. Yechieli, J. J. Gurdak, D. M. Allen, M. Shamsudduha, K. Hiscock, P. J.-F. Yeh, I. Holman, and H. Treidel (2013), Ground water and climate change, *Nature Climate Change*, *3*(4), 322–329, doi:10.1038/nclimate1744.

Terzaghi, K. (1925), Structure and Volume of voids in soils, translated from Erdbaumechanik auf bodenphysikalischer grundlage, in *From Theory to Practice in Soil Mechanics*, John Wiley, New York.

Torres, R., P. Snoeij, D. Geudtner, D. Bibby, M. Davidson, E. Attema, P. Potin, B. Rommen, N. Floury, M. Brown, I. N. Traver, P. Deghaye, B. Duesmann, B. Rosich, N. Miranda, C. Bruno, M. L'Abbate, R. Croci, A. Pietropaolo, M. Huchler, and F. Rostan (2012), GMES Sentinel-1 mission, *Remote Sensing of Environment*, *120*, 9–24, doi: 10.1016/j.rse.2011.05.028.

United Nations, Department of Economic and Social Affairs, and Population Division (2019), *World population prospects Highlights, 2019 revision*.

Van Aalst, M. K. (2006), The impacts of climate change on the risk of natural disasters, *Disasters*, *30*(1), 5–18, doi:10.1111/j.1467-9523.2006.00303.x.

Yevjevich, V. (1992), Water and Civilization, *Water International*, *17*(4), 163–171, doi: 10.1080/02508069208686135.

Chapter 2

GInSAR: A cGPS Correction for Enhanced InSAR Time Series

Abstract

Earth surface displacements from interferometric synthetic aperture radar (InSAR) have long been used to study deformation from a wide range of geophysical processes. Whereas deformation rates can be robustly estimated from InSAR by averaging many individual deformation observations, noise in these observations has limited their utility for generating deformation time series. In this article, we introduce a novel combination of InSAR and Global Positioning System (GPS) data that align InSAR displacements to an absolute reference and reduces long-wavelength spatial errors prior to InSAR time series construction. We test our GInSAR (GPS-enhanced InSAR) methodology on Sentinel-1 data over the southern Central Valley, CA, USA, comparing GInSAR dis-

placement velocities and time series with those from three other referencing techniques. We find that the GInSAR approach outperforms alternative methods, yielding mm-level displacement differences with respect to collocated cGPS. By contrast, other referencing methods can overestimate peak subsidence velocities in the Central Valley by upwards of 10%, deviate by tens of millimeters relative to cGPS validation time series, and contain spatial biases absent in the GInSAR methodology. We also present a modification to the widely used small baseline subset (SBAS) technique for time series estimation, whereby we use a temporal connectedness constraint to regularize the mathematical inversion and increase the number of InSAR pixels with valid time series estimates.

2.1 Introduction

The use of interferometric synthetic aperture radar (InSAR) to measure and observe Earth surface deformation from space represented a paradigm shift in geodetic remote sensing when it came into wide use over 20 years ago (*Massonnet and Feigl*, 1998). InSAR techniques, which use the difference in the carrier signal phase between SAR images to recover relative displacements over wide areas, have been used to study secular deformation related to tectonic processes (*Fialko*, 2006), volcanic activity (*Hooper et al.*, 2004), groundwater storage changes (*Amelung et al.*, 1999), glacial flow (*Fatland and Lingle*, 2002), and permafrost evolution (*Liu et al.*, 2012). With the availability of open source rapid-repeat SAR data, particularly from the European Space Agency's (ESA) Sentinel-1 missions and the upcoming joint National Aeronautics and Space Ad-

ministration (NASA) and Indian Space Research Organisation (ISRO) NISAR mission, InSAR's potential for recovering the temporal evolution of surface deformation is rapidly growing.

Despite this potential, InSAR accuracy is degraded by phenomena such as unmodeled atmospheric phase delay, satellite orbit uncertainty, and errors in interferometric processing (e.g., image resampling and phase unwrapping errors) (*Zebker et al.*, 1997; *Hanssen*, 2001), the effects of which can be of the same magnitude or larger than the deformation signal of interest. Additionally, since InSAR yields relative surface change, there is a benefit to linking collections of InSAR displacements via a common absolute reference (*Berardino et al.*, 2002), especially across multiple missions.

Various methods have been used to overcome these twin challenges, with much focus on incorporating displacement data from independent sources such as continuously operating Global Positioning System (cGPS) stations. Previous studies have jointly leveraged cGPS and InSAR data in several ways, which include combining short-wavelength secular deformation from InSAR with long-wavelength velocities from cGPS (*Wei et al.*, 2010; *Tong et al.*, 2013), using GPS horizontal velocities to decompose the three-component displacement time series (*Shirzaei and Bürgmann*, 2018), estimating along-track orbital errors using a priori deformation information from cGPS (*Gourmelen et al.*, 2010), or simply by referencing a single location in the InSAR scene to the motion of a collocated GPS station [e.g., (*Chaussard et al.*, 2014)]. While these approaches result in an improvement over using InSAR data alone, some challenges still remain. For example, the combination of short-wavelength InSAR deformation with cGPS ve-

locities is effective for constraining the horizontal velocity field where vertical motion is minimal and cGPS station density is high, but it can lead to biases if short-wavelength changes in velocities are spatially aliased into the long-wavelength cGPS velocity field. The estimation of along-track orbital errors from cGPS time series is useful, but only corrects errors in azimuth and not in range. Finally, referencing InSAR displacements to the contemporaneous motion of a single GPS station gives every interferometric pair a common absolute reference at the station location, but it also projects any positioning error specific to that station into the entire interferogram. It also neglects gradients in the plate motion across the scene, which is an important consideration near plate boundaries.

In this article, we introduce a simple methodology for estimating and correcting long-wavelength errors in InSAR displacements using continuous GPS time series data. Our approach, which we call GPS-enhanced InSAR (or GInSAR), assumes that differences primarily reflect errors in the InSAR observable (e.g., unmodeled tropospheric and/or ionospheric signal propagation delay, impact of soil moisture on surface height, and scattering properties (*Hanssen*, 2001)) that are mitigated in cGPS by design (deeply anchored monuments that are insensitive to near-surface changes (*Wyatt*, 1989), dual frequencies for removing ionospheric delay (*Melbourne*, 1985; *Wubbena*, 1985), and multiple satellite signal paths to constrain tropospheric effects (*Herring*, 1992)). GInSAR models the long-wavelength spatial structure in the cGPS-InSAR differences and removes it from the InSAR deformation field on an interferogram-by-interferogram basis prior to the estimation of InSAR time series. We apply our methodology to California's

southern Central Valley Aquifer System (CVAS) and environs, with particular focus on agricultural fields where we wish to improve our understanding of subsidence related to groundwater extraction (Figure 2.1). While our methodology does not seek to correct short-wavelength errors in InSAR (e.g., the turbulent component of atmospheric phase delay and changes in dielectric properties of the surface), it does offer several benefits relative to other approaches, as we will show.

2.2 InSAR Data and Processing

We estimated surface displacements in and around the southern CVAS from a suite of Sentinel-1 interferograms spanning November 2014 to February 2017. Our raw data set consisted of 49 Single Look Complex, Interferometric Wide swath acquisitions from descending track 144 of the Sentinel-1A/B missions (Table 2.S1 in Supplementary Material). Sentinel-1 satellites use a burst radar acquisition mode known as "terrain observation by progressive scans" (or TOPS) (*De Zan and Guarnieri*, 2006), which results in wide image swaths (250 km) and high geometric resolution (5 m $\times$ 20 m pixel dimensions) (*Torres et al.*, 2012). From these 49 scenes, we used the GMTSAR software package (*Sandwell et al.*, 2011; *Xu et al.*, 2017) to generate 276 interferograms. For our processing, we geometrically aligned our SAR scenes to a common master image (*Xu et al.*, 2017) from November 8, 2014 and used postprocessed precise orbits. We opted not to apply enhanced spectral diversity (ESD) because we observed that phase discontinuities at burst boundaries were infrequent and of relatively low magnitude (*Xu*

et al., 2017; *Shirzaei et al.*, 2017). We removed the topographic phase from these interferograms using the 1 arcsecond digital elevation model (DEM) from the Shuttle Radar Topography Mission (SRTM) (*Farr et al.*, 2007), and we imposed a maximum temporal separation of 100 days and a perpendicular baseline of 250 m between satellite orbits to maintain sufficient coherence between interferometric pairs (Figure 2.S1 in the Supplementary Material). GMTSAR uses the phase unwrapping algorithm Snaphu (*Chen and Zebker*, 2001) to convert wrapped interferograms into line of sight (LOS) displacements, for which we set a pixel correlation threshold of 0.1. A full description of GMTSAR processing steps and parameter options is outlined in *Xu et al.* (2017) and the GMTSAR manual (*Sandwell et al.*, 2011).

The fundamental InSAR observable is the difference in topography-corrected radar phase $\Delta\phi_{\text{obs}}(t_i, t_j)$ between times t_i and t_j at discrete ground locations (or pixels) (*Massonnet and Feigl*, 1998). The observed change in phase

$$\Delta\phi_{\text{obs}}(t_i, t_j) = \Delta\phi_{\text{def}}(t_i, t_j) + \Delta\phi_{\text{atm}}(t_i, t_j) + \Delta\phi_{\text{orb}}(t_i, t_j) + \Delta\phi_{\text{noise}}(t_i, t_j) \tag{2.1}$$

is a superposition of signals that includes the phase shift due to the surface deformation of interest $\Delta\phi_{\text{def}}(t_i, t_j)$ and the contribution of various nuisance signals, including atmospheric phase delay $\Delta\phi_{\text{atm}}(t_i, t_j)$, orbital errors $\Delta\phi_{\text{orb}}(t_i, t_j)$, and noise $\Delta\phi_{\text{noise}}(t_i, t_j)$ from changes in surface dielectric properties, phase decorrelation, residual topography, processing errors, etc. (*Hanssen*, 2001). Minimizing these nuisance terms results in a better estimate of surface deformation.

2.3 Continuous GPS Data and Processing

In the western USA, continuous Global Positioning System (cGPS) stations provide estimates of surface displacement at low spatial resolution (5–50 km) but relatively high temporal resolution (1 day). For this article, we used daily positions for the 122 continuous GPS stations from the National Science Foundation's Plate Boundary Observatory (PBO) network that lie within our InSAR footprint. These positions are provided in the global IGS08 (International GNSS Services 2008 (*Rebischung et al.*, 2012)) reference frame, are produced by the Geodesy Advancing Geoscience and EarthScope (GAGE) analysis centers (*Herring et al.*, 2016), and are publicly available from UNAVCO (ftp://data-out.unavco.org/pub/products).

We made three adjustments to the cGPS position time series to ensure compatibility between cGPS and InSAR observations. First, we removed offsets in the cGPS position time series due to documented equipment changes by estimating and removing displacement medians for 30 days on either side of the change date. We then smoothed the offset-corrected East/North/Vertical components for each station using a 6-day (2σ) Gaussian filter. This minimized power in the time series at periods shorter than $\sim$ 2 weeks, which we assume to be dominated by GPS multipath and tropospheric effects rather than true surface motion (*Borsa et al.*, 2007). Finally, we projected the three-component cGPS displacements into the satellite LOS direction using the SAR look angle, which is unique for every station location (Figure 2.S2 in the Supplementary Material).

We divided the 122 cGPS stations into three nonoverlapping sets for our analysis. The first ("*correction*") set consisted of the 54 stations used in the GInSAR correction (Figures 2.1 and 2.2, black squares). We ensured that these stations were distributed across the SAR footprint by binning the region into a grid of equal-area ($\sim 400\text{km}^2$) cells and selecting a cGPS station at random from each cell with at least one station. From the remaining stations, we used the same procedure to choose a second ("*validation*") set of 23 stations (Figures 2.1 and 2.2, red squares) for algorithm parameter selection and validation. The third ("*other*") set contained the remaining 45 stations, several of which were used to validate velocity profiles (see Section 2.6.1 and Figures 2.1 and 2.2, blue squares).

2.4 Correction of Long-Wavelength InSAR Displacements

GInSAR is an extension of a technique introduced by *Argus et al.* (2005) to correct long-wavelength errors attributed to unmodeled atmospheric delay. *Argus et al.* (2005) estimated surface displacements at GPS station locations from a simple velocity and seasonal sinusoid model that they fit to each GPS time series (hereafter referred to as modeled GPS). They differenced modeled GPS values over three interferometric pairs spanning 6 to 24 months to obtain a set of reference displacements, fit a minimum-curvature surface to the residuals between the reference and InSAR displacements, and added the fitted surface to each interferogram. They demonstrated that this technique

improves the 95% confidence limits of the vertical InSAR estimates by a factor of three, from approximately ±15 to ±5 mm.

We expand on the *Argus et al.* (2005) technique in three ways as follows.

1. We apply it to 276 interferometric pairs spanning 6 to 96 days, representing nearly a 100-fold increase in the size of the corrected InSAR data set.

2. We use the actual cGPS time series data rather than the modeled GPS for the correction, which allows us to capture the significant short-period and interannual surface deformation that exists within the InSAR footprint.

3. We search for an optimal functional form for the surface fit, with an emphasis on long-wavelength errors.

We applied the GInSAR algorithm described below to each interferogram independently, with InSAR and cGPS displacements evaluated in LOS coordinates and the cGPS positions offset-corrected and smoothed as described in Section 2.3:

1. For each interferogram n and cGPS correction station k, we calculated the cGPS LOS displacement as

$$d_{nk}^{\mathrm{GPS}} = s_k^{\mathrm{GPS}}(t_j) - s_k^{\mathrm{GPS}}(t_i) \tag{2.2}$$

from the cGPS position time series $s_k^{\mathrm{GPS}}(t)$ evaluated at SAR acquisition t_j and t_i, which are unique to each interferogram.

2. We took the difference between the InSAR and cGPS LOS displacements at each

correction station to form the residual

$$r_{nk} = d_{nk}^{\mathrm{GPS}} - d_{nk}^{\mathrm{InSAR}} \tag{2.3}$$

where d_{nk} is the displacement at station k for interferogram n. To minimize pixel-scale noise (e.g., unwrapping errors or short-wavelength changes in scattering properties (*Hanssen*, 2001)), we took d^{InSAR} to be median InSAR displacement value within a 30-pixel-wide box centered on each station location.

3. We fit a second-order polynomial surface to r_{nk} using the "fit" function in MATLAB, generating a residual (or correction) model $r_n(lat, lon)$ from which we estimated the long-wavelength error at each InSAR pixel (see Figure 2.S3 in the Supplementary Material for our choice of the functional form of the polynomial fit). Since the r_{nk} are distributed across the InSAR scene because of how we selected the cGPS correction stations, they provide a strong spatial constraint on the polynomial fit.

4. Finally, we estimated the GInSAR-corrected interferometric displacement $d_n^{\mathrm{GInSAR}}(lat, lon)$ for each interferogram n by adding the residual model back to the InSAR displacement field

$$d_n^{\mathrm{GInSAR}}(lat, lon) = d_n^{\mathrm{InSAR}}(lat, lon) + r_n(lat, lon). \tag{2.4}$$

We used the resulting suite of GInSAR-corrected interferograms as input into our InSAR time series generation workflow.

2.5 Generation of Deformation Time Series: CS-BAS

The Small Baseline Subset (SBAS) method (*Berardino et al.*, 2002) is an inversion algorithm for reconstructing deformation time series from a set of coregistered interferograms with small orbital separations. SBAS is well suited for data sets in urban or rocky regions, where correlation of the phase observable between SAR scenes is high. In regions with heavy vegetation or periodic resurfacing (e.g., from plowing/harvesting or seasonal snowfall), points on the ground can exhibit low or variable coherence (*Wei and Sandwell*, 2010). Pixels with low correlation (low signal-to-noise) values in any of the interferograms are typically excluded from standard SBAS processing (*Tong and Schmidt*, 2016). To the extent that redundant temporal overlaps in other InSAR pairs can provide information spanning the low-correlation interval, this processing strategy has the effect of unnecessarily reducing data coverage within the InSAR footprint. The problem is particularly acute where large InSAR data sets are processed with SBAS, since the likelihood of random single-interferogram decorrelation at any given pixel increases with the number of interferograms used.

Several modifications to SBAS have been proposed to incorporate phase information from pixels with intermittent correlation (e.g., *Sowter et al.* (2013); *Tong and Schmidt* (2016)). One approach, the Intermittent SBAS method (ISBAS), relaxes the criterion that a pixel must be coherent in all interferograms and instead sets a threshold for the number of interferograms in which the pixel is coherent (e.g., 60% of the total)

(*Sowter et al.*, 2013; *Bateson et al.*, 2015). Here, we implement our own version of ISBAS that instead imposes a temporal connectedness criterion for each pixel. Our algorithm, which we call CSBAS (temporally Connected SBAS; Figure 2.S4 in the Supplementary Material), considers only pixels for which there is at least one valid displacement estimate spanning every interval of the time series. This avoids the potential problem (inherent in other SBAS implementations) of estimating time series across periods for which there is no observational constraint.

SBAS methods solve for the instantaneous velocity at each SAR acquisition time t_i (*Berardino et al.*, 2002) and integrate these velocities to produce a time series of LOS displacements. For a single pixel, the problem can be written as

$$B\mathbf{v} - \mathbf{d} = 0 \tag{2.5}$$

$$\begin{bmatrix} t_2 - t_1 & 0 & 0 & \dots & 0 \\ t_2 - t_1 & t_3 - t_2 & t_4 - t_3 & \dots & 0 \\ 0 & t_3 - t_2 & t_4 - t_3 & \dots & 0 \\ \vdots & \vdots & \vdots & \vdots & \vdots \\ \vdots & \vdots & \vdots & \vdots & \vdots \\ 0 & \dots & \dots & \dots & t_P - t_{P-1} \end{bmatrix} \begin{bmatrix} v_1 \\ v_2 \\ v_3 \\ \vdots \\ v_{P-1} \end{bmatrix} - \begin{bmatrix} d_1 \\ d_2 \\ d_3 \\ \vdots \\ \vdots \\ d_N \end{bmatrix} = 0 \tag{2.6}$$

where $\mathbf{v}$ is a $(P-1) \times 1$ vector of velocities between the P sequential SAR acquisition times, $\mathbf{d}$ is an $N \times 1$ vector of observed interferometric displacements, and B is an $N \times P$

matrix that integrates the velocity solution into displacement estimates corresponding to each of the N interferograms. The structure of B depends on the specific interferograms used in our CSBAS inversion, although in all cases there will be at least one displacement observation constraining the value of each element of $\mathbf{v}$. In the hypothetical example shown in (2.6), this pixel did not have a valid SAR phase measurement at time t_3; however, however, displacements from two spanning interferograms (between t_4 and t_1 in row 2 of B, and t_4 and t_2 in row 3) constrain the velocity for this epoch.

In addition to requiring temporal connectedness for $\mathbf{v}$, CSBAS also minimizes large changes in velocity between SAR acquisitions (often attributed to the turbulent component of atmospheric noise $\Delta\phi_{\text{atm}}$) by imposing a first-order (smoothness) Tikhonov regularization on (2.5). The regularized form of the problem is

$$\begin{bmatrix} B \\ \\ \lambda L_1 \end{bmatrix} \mathbf{v} - \begin{bmatrix} \mathbf{d} \\ \\ 0 \end{bmatrix} = 0 \tag{2.7}$$

where L_1 is the $P \times P$ first-difference matrix

$$L_1 = \begin{bmatrix} -1 & 1 & & & & \\ & -1 & 1 & & & \\ & & \ddots & \ddots & & \\ & & & -1 & 1 & \\ & & & & -1 & 1 \end{bmatrix} \tag{2.8}$$

and λ is a weighting parameter that determines the degree of temporal smoothing for $\mathbf{v}$.

For our analysis, we substituted d^{GInSAR} in place of $\mathbf{d}$ in (2.7) and chose $\lambda = 150$, which resulted in a close fit between the GInSAR and validation cGPS displacements without over-smoothing the time series (see L-curve analysis in Figure 2.S5 in the Supplementary Material). To solve for velocity, we minimized the left-hand side in (2.7) using a least-squares inversion with the Moore-Penrose pseudoinverse of our extended B matrix (*Ben-Israel and Greville*, 2003). After inverting, we integrated the velocity vector for each pixel over time to generate the displacement time series $s^{\mathrm{GInSAR}}(lat, lon, t)$.

2.6 Validation and Comparison With Other InSAR Correction Approaches

We assessed the performance of GInSAR by validating both the velocities and time series of InSAR deformation with respect to independent estimates from cGPS. We used two different approaches for the validation: an *absolute* referencing approach that directly compared InSAR and cGPS estimates at individual cGPS station locations, and a *relative* referencing approach that compared InSAR and cGPS differences between pairs of station locations. Unlike the absolute approach, the relative approach is insensitive to reference frame shifts between InSAR and cGPS, which would manifest almost entirely as uniform translations across our study region.

2.6.1 Velocity Validation

For the absolute validation of the GInSAR velocity field, we analyzed the residuals between cGPS and GInSAR velocities at the locations of the 23 validation cGPS stations described in Section 2.3. We estimated the reference cGPS velocities by fitting a straight line to cGPS displacements at each station, using a robust least-squares technique that iteratively reweights outliers with a bisquare weighting function. We similarly estimated GInSAR velocities from the GInSAR displacement time iseries at all pixels in our study area. For the GInSAR velocity at the validation stations themselves, we took the median value within a 30-pixel-wide box centered on each station location. We differenced these two sets of velocities to form a collection of 23 velocity residuals, for which we calculated the median and the robust standard deviation σ_r (defined as the median absolute deviation scaled by 1.4826). Assuming the cGPS velocities represent "truth," the better the InSAR correction is, the closer the median and σ_r would be to zero.

We evaluated GInSAR's performance with respect to three alternative referencing schemes: 1) "Uncorrected," which simply uses the raw InSAR LOS displacements without correction; 2) "Pinned to ground," which zero-references each interferogram to a single pixel at a location assumed to have minimal deformation; and 3) "Pinned to GPS," which references each interferogram to cGPS displacements at a single station. For each scheme, we applied the same CSBAS algorithm and smoothing parameters that we used to obtain our GInSAR results. We tested the "Pinned to ground" and "Pinned to GPS" schemes at eleven cGPS station locations, but used P560, which is in a region

of the Mojave Desert with minimal vertical deformation relative to the rest of the scene, to illustrate our technique (Figures 2.2-2.5).

In addition to point validation at cGPS locations, we also examined the spatial characteristics of the velocity fields generated using each of the referencing schemes. Specifically, we extracted two velocity profiles across our study area (A-A′ and B-B′, shown in Figure 2.2) along which we compared results between the four referencing schemes. Profile A-A′ strikes predominately west to east, while B-B′ strikes northwest to southeast and intersects the "Pinned to ground" and "Pinned to GPS" station locations. Both cover a range of horizontal tectonic and vertical hydrologic deformation signals. We obtained reference velocity profiles from the Southern California Earthquake Center (SCEC) Community Geodetic Model (CGM) Horizontal Velocity Grid (*Sandwell et al.*, 2016), which we transformed from the Stable North American Reference Frame (SNARF) to the IGS08 reference frame and projected into LOS for comparison with eight cGPS stations near A-A′ and six stations near B-B′. While the SCEC model contains only the horizontal components of motion, it provides important validation for regions where we expect minimal vertical signal.

2.6.2 Time Series Validation

We followed a similar methodology to validate shorter period variability in the InSAR time series. First, we estimated and removed a linear trend from the 23 validation cGPS time series and from the corresponding InSAR deformation time series for each of the four referencing schemes. We then differenced the detrended cGPS and InSAR

time series to form displacement residuals (whose mean and median values are nominally zero by construction).We report the robust standard deviation, σ_r, of the residuals as a measure of time series variance for the various referencing schemes (Tables 2.1 and 2.2). For the relative validation, we differenced the cGPS time series between station pairs, then differenced the corresponding InSAR time series for those same pairs. We report the median and robust standard deviation of the residuals between the differenced InSAR and cGPS time series in Table 2.1.

2.7 Results and Discussion

Our validation results show that the inclusion of position information from multiple cGPS stations in GInSAR improves InSAR displacement estimates in two key ways: 1) it removes biases in the InSAR velocities with respect to independent cGPS estimates and 2) it removes large excursions in InSAR displacement time series that we assume to be related to errors in the InSAR observable in one or more individual interferograms.

2.7.1 InSAR Velocity Improvement

Application of the GInSAR methodology to Sentinel-1 interferograms over the southern Central Valley significantly reduces the residuals between InSAR velocity estimates and those from cGPS (Table 2.1). Relative to "Uncorrected" InSAR, GInSAR results in an order of magnitude reduction in the velocity residual median (from 12.3 to -1.0 mm/yr) and a 42% reduction in σ_r (from 6.0 to 3.5 mm/yr).

GInSAR also outperforms the two schemes that pin each interferogram to a single location within the SAR footprint ("Pinned to ground" and "Pinned to GPS"). Relative to those schemes, GInSAR results in reduction by a factor of 10 and 3 (respectively) in the residual median and a 24% and 45% reduction in σ_r (Tables 2.1 and 2.2), highlighting the benefit of using multiple cGPS stations to model long-wavelength errors across the SAR scene.

The "Pinned to GPS" scheme at station P560 does better than "Pinned to ground" in terms of reducing the residual median velocity, but worse in terms of σ_r (Table 2.1). When we consider a suite of pinning locations at various cGPS station locations across the scene (Table 2.2), we find that "Pinned to GPS" systematically outperforms "Pinned to ground" in terms of residual median, while the two perform similarly in terms of σ_r . However, the variability we observe from using different GPS station locations for pinning in either scheme, including GPS stations that are near each other (e.g., ETLN and P560), underscores the risk of pinning to a single location when InSAR errors are likely to vary differentially over the entire scene.

GInSAR performs even better with respect to the alternative referencing schemes in the relative validation (Table 2.1). GInSAR achieves a reduction in the velocity residual median by a factor of 38 to 62, along with a 49% to 53% reduction in σ_r. Comparing results between the absolute and relative validations, all four referencing schemes produce a smaller residual median in the relative validation, which is expected due to the fact that double-differencing removes the effect of expected reference frame differences between cGPS and InSAR. The increase in the velocity residual σ_r between

the absolute and relative validations is also expected. Because variances are additive under subtraction (assuming roughly Gaussian-distributed uncertainties), the double-differencing operation in the relative validation amplifies noise inherent in the cGPS and InSAR estimates, thereby increasing σ_r.

The secular velocity fields for each of the four schemes (Figure 2.2) all identify similar locations of surface deformation (e.g., the large subsidence bowls in agricultural areas and more compact regions of hydrocarbon production on the periphery of the southern Central Valley), but they give different quantitative estimates of deformation magnitude. For example, peak subsidence values near Corcoran relative to a nonagricultural area to the east of the Central Valley [marked by a red star in Figure 2.2a] range from -334.3 mm/yr (GInSAR) to -381.9 mm/yr ("Pinned to GPS"), with intermediate values of -360.3 mm/yr ("Pinned to ground") and -369.7 mm/yr ("Uncorrected"). The 35.4 mm/yr difference between GInSAR and "Uncorrected" InSAR represents an 11% overestimation of peak subsidence when no correction is applied. Additionally, the median displacement outside the high-deformation agricultural areas is different between schemes, as can be seen in the various panels of Figure 2.2 (e.g., the Sierra foothills are deeper blue, indicating more uplift, in the schemes excluding GPS). These differences are largely a result of how the reference frame is handled by the different schemes. Since raw InSAR data only provide relative displacements, the "Uncorrected" and "Pinned to ground" results are blind to average secular motion across the scene due to long-wavelength phenomena such as plate tectonics. This motion is partly restored as a static shift when absolute position information is provided by GPS, as evidenced in the

"Pinned to GPS" and GInSAR schemes.

Differences between velocity fields become even more evident when we examine profiles A-A′ and B-B′ (Figures 2.3 and 2.4). For both profiles, the most notable difference between the schemes is an offset of 15–20 mm/yr in nondeforming regions between results without some form of GPS correction ("Uncorrected" and "Pinned to ground" lines) and results incorporating information from GPS ("Pinned to GPS" and GInSAR lines). This shift is consistent with the average local velocity of LOS-projected GPS in the IGS08 reference frame.

Short-wavelength noise is markedly reduced in the GInSAR result compared to other referencing schemes. For example, the GInSAR velocity profile shows a clear jump across the San Andreas Fault [Figure 2.3 (inset)] that is consistent with independent cGPS velocities and the SCEC CGM. While the jump is also apparent in the non-GInSAR profiles, those profiles have higher variability to the east and west, which increases the uncertainty in any estimation of jump magnitude. Additionally, GInSAR estimates are the most consistent with SCEC's CGM in locations with little to no vertical deformation, and they are the most consistent with cGPS velocities in general. This agreement instills confidence in the GInSAR results. By contrast, the "Pinned to GPS" case performs well near the station to which it is referenced to (e.g., P560 in Figure 2.4), but can deviate from cGPS stations that are further away (e.g., Figure 2.3, west of -120 longitude; Figure 2.S6). The strength of the GInSAR method is that it performs comparably to the "Pinned at GPS" near the pinning location, in addition to performing well elsewhere in the scene. GInSAR velocities do exhibit occasional mm-level discrepancies

with respect to individual cGPS station velocities, but these are typically much smaller than the case with other schemes. We attribute some of these differences to the spatial and temporal smoothing applied to the InSAR time series used to generate our velocity fields.

2.7.2 Time Series Improvement

In addition to improving velocity estimates, the GInSAR methodology is also effective in correcting short-period errors in InSAR time series. The absolute validation shows that relative to the other referencing schemes, GInSAR results in a 69%–71% reduction in the robust standard deviation of time series residuals with respect to the 23 cGPS validation stations (Table 2.1). Also, the GInSAR results do not show a spatial dependence in residual variance across the study region. This is not the case with the "Pinned to ground" and "Pinned to GPS" schemes, where variance reduction is the strongest near the pinning location. For example, in the case of pinning at P560, residual variance is reduced in the southeast of the scene near P560, but remains high at stations near Parkfield to the northwest (Figure 2.S6 in Supplementary Material). Furthermore, the time series performance of the two pinning schemes is affected by the choice of the pinning location, as it is with velocities (Table 2.2).

GInSAR also performs well in the relative validation, providing a 49% to 53% reduction in the standard deviation of double-difference time series residuals (Table 2.1). Similar to the case with velocity residuals, the robust standard deviation of the time series residuals is considerably higher ($\sim$ 50%) for the relative validation than for the

absolute validation. As we explained in Section 2.7.1, this is consistent with the increase in variance expected from double-differencing in the relative validation.

We compared the displacement time series from each referencing scheme with cGPS time series at three stations: ARM1 (located in the subsidence bowl south of Bakersfield and used in the GInSAR correction), P560 (located to the southeast and used as the reference point for "Pinned to ground" and "Pinned to GPS," but not used in the GInSAR correction), and P530 (located to the west and fully independent of all referencing schemes) (Figure 2.5).

For these stations, all GInSAR time series show a close agreement with those from cGPS, with differences rarely exceeding 10 mm. At P560, which is the pinning location for both pinning schemes, "Pinned to GPS" slightly outperforms the GInSAR time series. This is expected since the correction is optimized for the pinning location. At ARM1, "Pinned to GPS" does almost as well as GInSAR, consistent with the fact that ARM1 is only 50 km from the pinning location and likely experiences similar atmospheric effects. At P530, which is 200 km from the pinning location, all the non-GInSAR schemes perform poorly, deviating by up to 40 mm from the cGPS. In all cases, "Pinned to ground" performs about as poorly as "Uncorrected," underscoring the fact that even in a relatively stable location like the western Mojave Desert (where P560 is located) there is often significant surface motion or phase error.

2.7.3 Effect of cGPS Station Coverage

A key consideration for the utility of the GInSAR method is the spatial distribution of cGPS stations available for interferometric correction. To test the dependence of GInSAR on the geometry of the cGPS network, we evaluated the performance of the GInSAR correction for varying numbers and locations of cGPS correction stations. Our goal was to assess the minimum number and distribution of stations needed to: 1) constrain the correction model r_n (Section 2.4) and 2) ensure a good agreement between cGPS and GInSAR displacements.

For our test, we selected groups of at least six cGPS stations (the minimum needed to constrain a second-order polynomial surface) corresponding to every possible combination of stations in our cGPS correction set. For each of these station groups, we performed the GInSAR correction procedure on 13 randomly selected interferograms (e.g., Figure 2.S10).

For the interferogram spanning March 2–June 6, 2016, we calculated the root-mean-square (rms) of the residuals between cGPS and GInSAR displacement time series at the validation station locations (the "validation residuals"). Smaller rms values indicate a closer agreement between cGPS and GInSAR, and thus better performance of the GInSAR correction for a given station configuration (Figure 2.S9). Additionally, for all interferograms, we calculated the robust standard deviation of all pixels in the residual model r_n to assess the model size (Figure 2.S10). In general, larger models result from "clumpy" station distributions that provide insufficient spatial constraints

on the polynomial fit in Section 2.4, Step 3.

On average, increasing the number of correction stations (i.e., adding constraints for the determination of r_n) resulted in smaller validation residuals (Figure 2.S9) and smaller correction models (Figure 2.S10). However, performance did not uniformly improve with higher numbers of stations. We found diminishing returns on GInSAR performance beyond 15 stations (spacing of $\sim$ 50 km), and some configurations with many stations yielded high rms values. These configurations tend to be those with "clumpy" station distributions that did not sample the full SAR footprint. Finally, we found that the minimum rms is fairly constant at $\sim$ 14 mm, indicating that even minimal station coverage (e.g., six stations at a spacing of $\sim$ 85 km) is sufficient to support the GInSAR correction, provided that the stations are in an optimal spatial configuration (Figure 2.S8).

Our results from the southern Central Valley are encouraging from the standpoint of using GInSAR in areas without the dense cGPS coverage of California. Even a modest cGPS station spacing of 75 km can support the optimal correction of long-wavelength InSAR errors, provided the stations are distributed across the SAR footprint. In all cases, we recommend that potential users of GInSAR validate the correction in their region of interest, using Section 2.6 as a guide.

2.7.4 Errors Uncorrected by GInSAR

While the GInSAR correction is a promising approach for correcting long-wavelength InSAR error in areas with adequate cGPS coverage, it is limited in several

ways. For example, short-wavelength noise, which is often correlated with high gradients in topography or in atmospheric properties (*Hanssen*, 2001), cannot be removed using the GInSAR methodology. We apply smoothing in the CSBAS time series estimation in part to mitigate the impact of this noise, but we note that GInSAR corrects a significant component of short-period noise even without smoothing (compare Figure 2.5 and Figure 2.S11). Compared to alternative correction schemes with their greater short-period noise (Figure 2.S11), GInSAR should improve the detectability of transients in the InSAR time series.

While smoothing may be appropriate for observing slowly varying processes such as changes in groundwater, we recognize that it may not be ideal for time series that include impulsive processes such as earthquakes. However, the GInSAR correction is compatible with other interferogram-correcting techniques that are better suited to removing short-wavelength noise (such as those incorporating atmospheric models or empirical noise estimates (*Tymofyeyeva and Fialko*, 2015; *Yu et al.*, 2018), filtered to exclude the long-wavelength components supplied by GInSAR). These alternatives can be used instead of smoothing in cases where the signals of interest are transient.

2.8 Conclusions

The expansion of SAR data catalogs from ESA's Sentinel-1 and the prospect of the upcoming NISAR mission offer new opportunities for studying earth's surface deformation at high spatial resolution (10s of meters) and low latency (1–2 weeks). However,

error terms in the InSAR observable and a need to link collections of interferograms via a common absolute reference inhibit the reconstruction of detailed deformation time series. Using our GInSAR methodology, we obviate many of these limitations by leveraging the observed differences between InSAR and cGPS displacements to model and remove long-wavelength spatial errors from each SAR interferogram, while imposing an absolute reference frame common to the cGPS displacements. In short, we minimize long-wavelength components of the nuisance terms in (2.1) while preserving signal common to independent data sets. Further, we retain a denser collection of coherent InSAR pixels than traditional SBAS methods through the use of our temporally Connected SBAS (CSBAS) algorithm, which only excludes pixels for which there are temporal gaps in observational constraints. Finally, since our GInSAR operates on individual interferograms, it is compatible with a variety of SAR data, interferometric product generation methods, time series construction algorithms (*Berardino et al.*, 2002; *Hooper et al.*, 2004), and additional interferometric corrections (e.g., (*Tymofyeyeva and Fialko*, 2015; *Yu et al.*, 2018)).

We tested our GInSAR methodology against three other referencing techniques using Sentinel-1 SAR data over the southern Central Valley. We found that GInSAR significantly outperformed the "Uncorrected," "Pinned to ground," and "Pinned to GPS" schemes for estimating both secular surface velocities and displacement time series, consistent with results reported by *Argus et al.* (2005).

We attribute most of the differences in velocity estimates between each scheme to how the displacement reference frame is handled. Methodologies that include cGPS time-

series information ("Pinned to GPS" and GInSAR) contain average plate velocity in the LOS-projected IGS08 reference frame, which improves velocity estimates with respect to cGPS. Near the North American and Pacific Plate boundary, where the relative velocity between the two plates is on the order of 45 mm/yr (*DeMets et al.*, 1990, 1994), plate motion is an important consideration in the context of total deformation and discrepancies between referencing methods. While pinning to a single GPS may improve results near the pinning location, velocity gradients across large-swath SAR scenes can yield comparisons at distant cGPS stations that are as poor as when no correction is applied.

Typical InSAR time series generation techniques often apply heavy smoothing to reduce noise, at the expense of important short-period signals that may be relevant for low-latency monitoring. Our GInSAR methodology, on the other hand, is capable of reducing noise without smoothing over shortperiod variability that is independently observed in cGPS time series. We find that using a single pinning location ("Pinned to ground" and "Pinned to GPS") cannot resolve this short-period variability across the entire SAR footprint.

With more InSAR and cGPS data becoming openly available, this new methodology bridges the two observational data sets, establishes an absolute reference frame between interferograms, and improves our confidence in spatially dense time series of surface deformation.

Acknowledgements

The authors would like to thank the three reviewers for their insightful suggestions that helped improve the quality of the manuscript. This work was made possible in part by the open data policies of ESA (Sentinel-1), GAGE analysis centers with data archived by UNAVCO (cGPS), SCEC CGM, and USGS (fault traces). They would also like to thank X. Xu, E. Tymofyeyeva, and D. T. Sandwell for the many enlightening internal discussions. Maps and plots were made using the Generic Mapping Tools and MATLAB.

Chapter 2, in full, is a reformatted version of material as it appears in IEEE Transactions on Geoscience and Remote Sensing: Neely, W. R., A. A. Borsa, and F. Silverii (2020), GInSAR: A cGPS Correction for Enhanced InSAR Time Series, *IEEE Transactions on Geoscience and Remote Sensing*, 58(1), 136–146, doi: 10.1109/TGRS.2019.2934118. I was the primary investigator and author of this paper.

Table 2.1: Validation summary for pinning schemes.

	Absolute			Relative		
Scheme	Velocity Residual Median (mm/yr)	Velocity Residual σ_r (mm/yr)	Time Series Residual σ_r (mm)	Velocity Residual Median (mm/yr)	Velocity Residual σ_r (mm/yr)	Time Series Residual σ_r (mm)
Uncorrected	12.3	6.0	11.4	6.2	9.8	23.4
Pinned to ground*	11.9	4.6	11.4	3.8	9.9	21.6
Pinned to GPS*	-2.2	6.4	10.5	6.1	10.6	22.4
GInSAR	**-1.0**	**3.5**	**3.3**	**0.1**	**5.4**	**11.0**

* The pinning location used is P560, which is representative of a low-deformation region of the interferogram.

Table 2.2: Absolute validation summary for pinning locations.

Station Location Name	Velocity Residual Median (mm/yr)		Velocity Residual σ_r (mm/yr)		Time Series Residual σ_r (mm)	
	Ground	GPS	Ground	GPS	Ground	GPS
BEPK	10.5	-2.0	6.5	5.5	17.8	17.4
ELTN	12.9	-3.3	4.6	4.0	11.0	10.5
P056	111.6	-8.7	5.1	9.8	10.1	10.3
P280	24.4	18.6	4.0	4.2	8.3	9.1
P299	23.8	32.6	3.9	7.4	11.4	11.4
P518	25.4	-6.8	3.2	4.2	8.5	8.1
P522	18.6	-0.3	4.5	4.4	9.5	8.6
P545	30.8	2.1	5.4	5.4	9.1	8.1
P550	18.6	0.7	3.0	4.7	13.2	9.9
P560*	**11.9**	**-2.2**	**4.6**	**6.4**	**11.4**	**10.5**
P570	13.2	-0.5	4.9	5.9	12.2	10.8
Median	**18.6**	**-0.5**	**4.6**	**5.4**	**11.0**	**10.3**

* Station location used in Table 2.1 and Figs. 2.2-2.5.

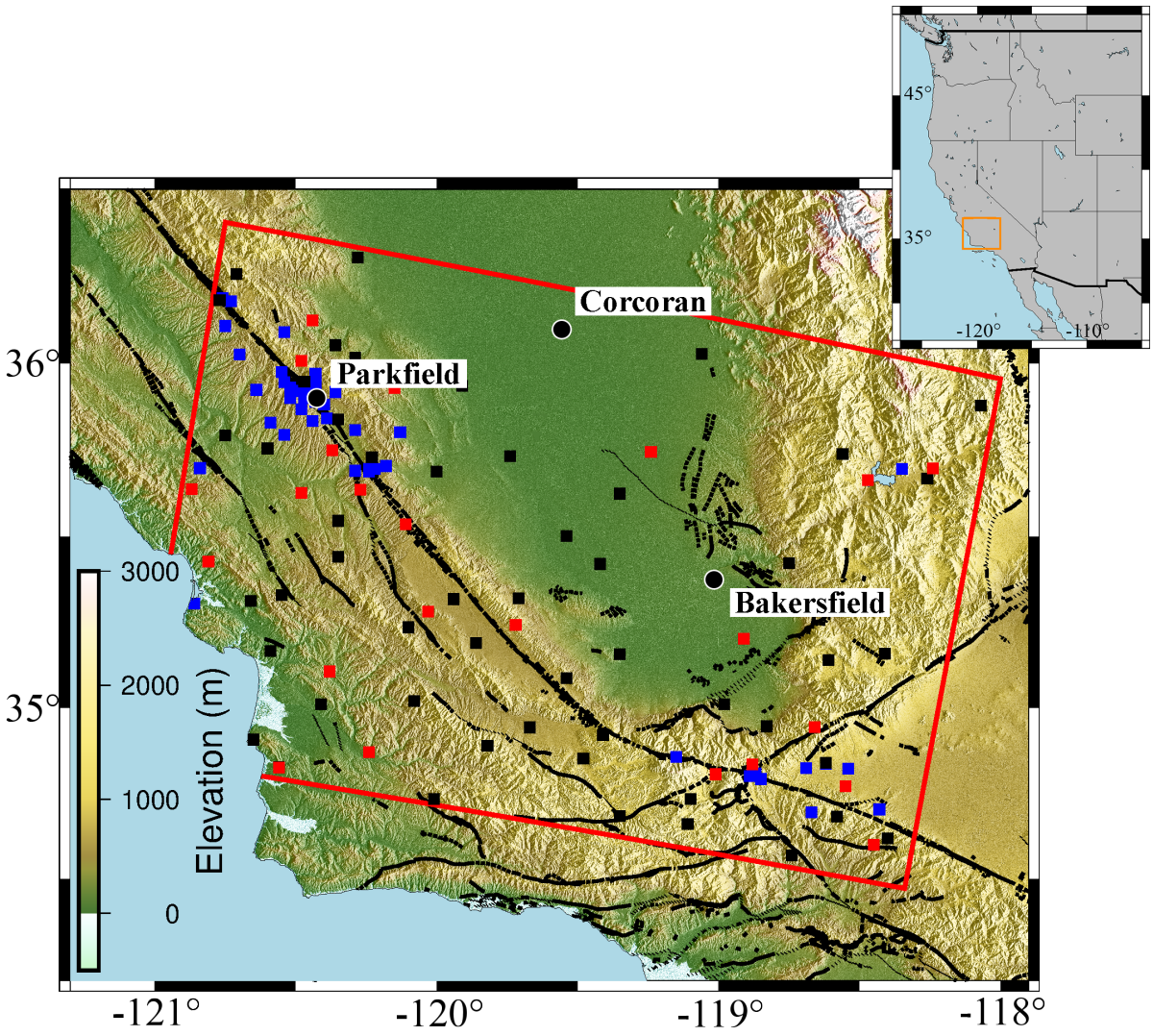

Figure 2.1: Topographic map of the southern Central Valley, CA and environs. The inset shows the western United States with the orange box delineating the mapped area. The red box marks the boundary for our InSAR footprint. Square symbols represent the available cGPS stations from the Geodesy Advancing Geoscience and EarthScope (GAGE) network inside the SAR footprint. Black squares indicate stations used in our correction process. Red squares are locations of the validation cGPS stations. Blue squares are the remaining available cGPS stations. The black lines indicate fault traces in the region (from the USGS). Different line types correspond to how well constrained the fault locations are: solid lines are well constrained, dashed lines are moderately constrained, and thinly dotted lines are inferred locations. Black circles mark notable population centers in the region.

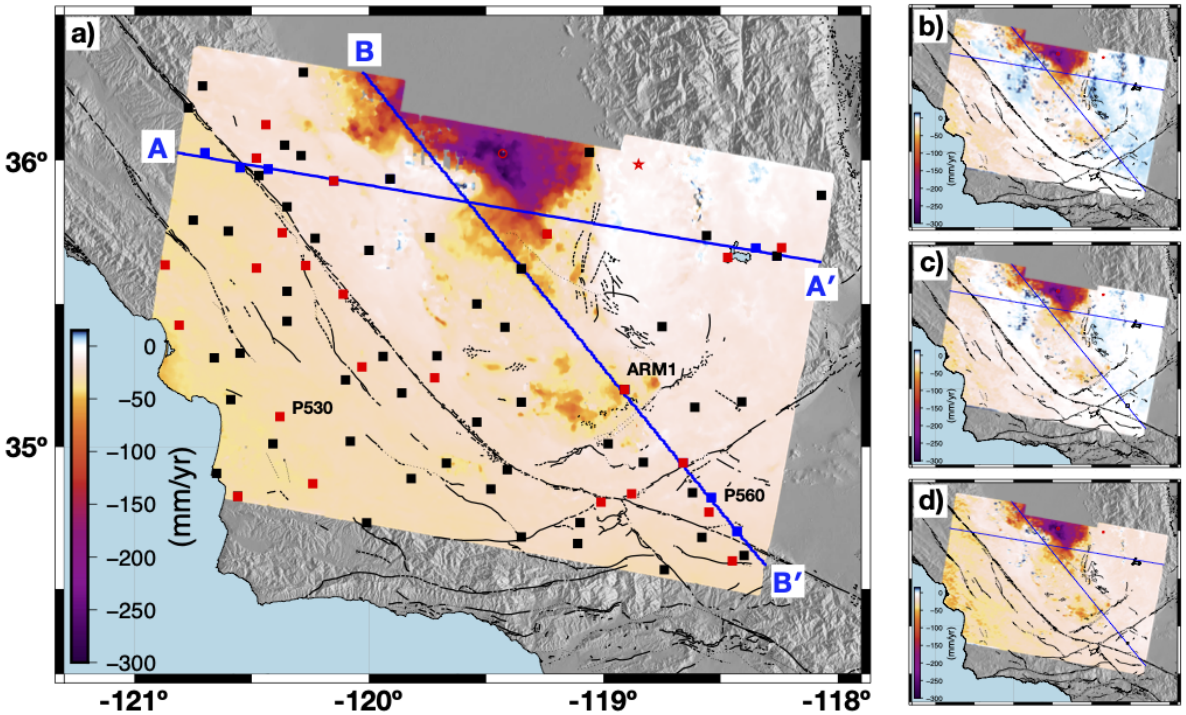

Figure 2.2: Velocity maps of inverted InSAR data for the four interferogram referencing techniques over the same region shown in Figure 1.1. The results are in LOS velocity (mm/yr) and are median filtered (1-km radius). Blue lines are profile transects used in Figures 2.3 and 2.4. The red circle marks peak subsidence and the red star denotes the nonagricultural reference location used in Section 2.7.1. (a) GInSAR deformation with cGPS stations used in the correction (black squares), cGPS validation station locations (red squares), additional cGPS stations used in the profile comparison (blue squares), and time series locations labeled. The remaining panels show (b) "Uncorrected" results, (c) "Pinned to ground" (at P560 site location), and (d) "Pinned to GPS" (at P560).

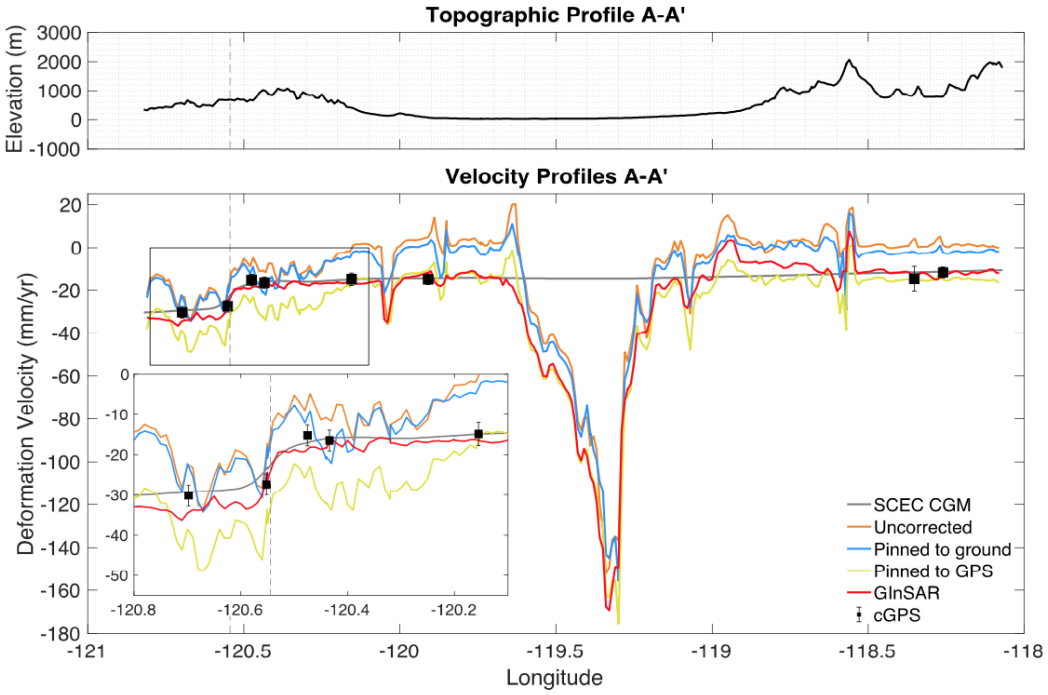

Figure 2.3: Velocity profiles along the transect A-A′ shown in Figure 2.2, with corresponding topography. Colored lines are different pinning schemes. The solid gray line is the horizontal velocity from the South California Earthquake Center's Community Geodetic model. Black squares are cGPS velocities with 3σ error bars. The dashed gray line marks the location of the San Andreas Fault. Inset shows a closer view of the section near the fault.

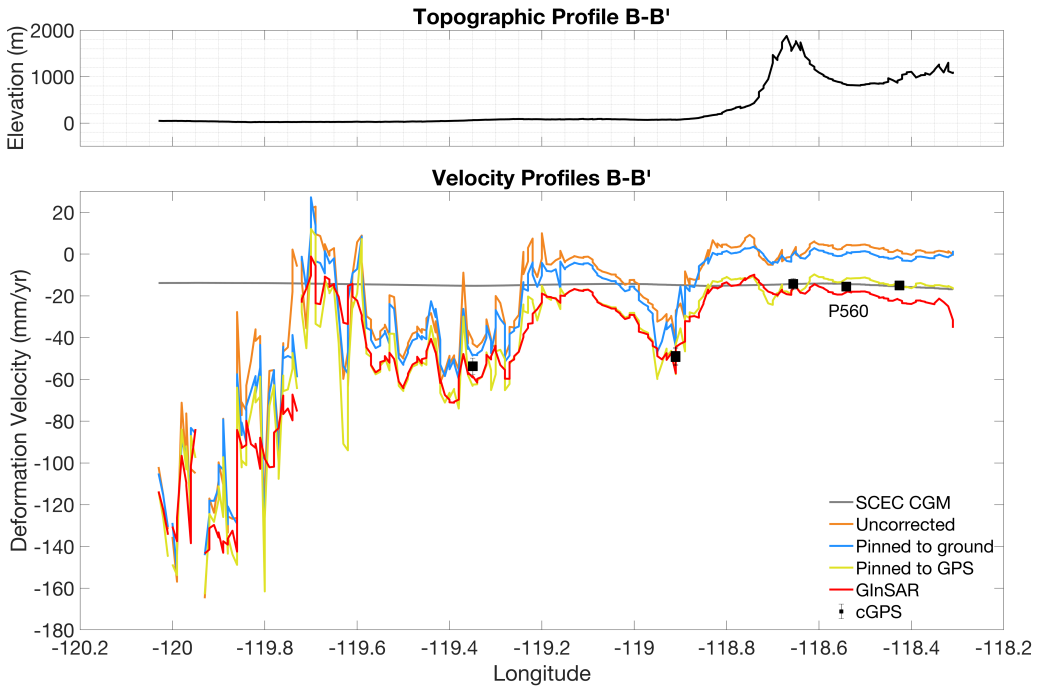

Figure 2.4: Same as Figure 2.3, but for the transect B-B′.

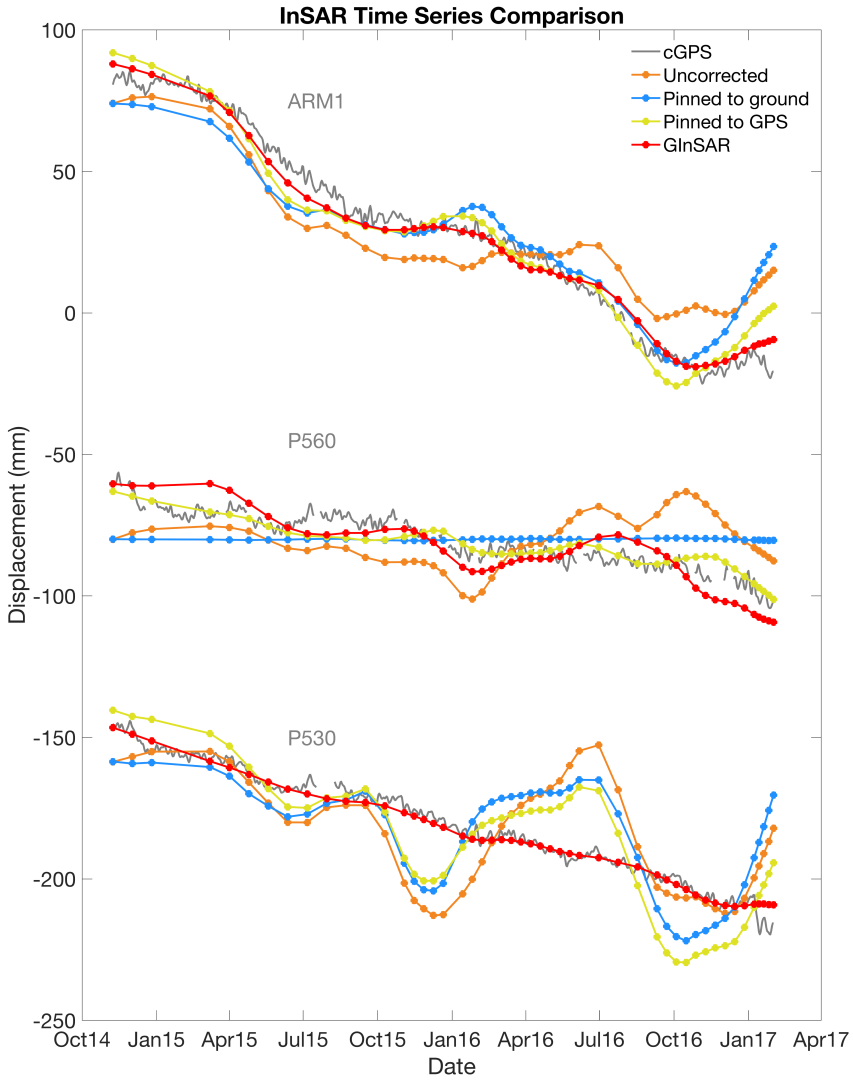

Figure 2.5: Time-series comparisons (offset for clarity) of the four tested referencing techniques and collocated cGPS time series at stations ARM1, P560, and P530. ARM1 is one of the stations used in the correction for GInSAR and is located in a region of subsidence. P560 is used as the pinning location for "Pinned to Ground" and "Pinned to cGPS." P530 is a cGPS location independent of the pinning schemes and is used in the validation.

2.9 Supplementary Materials

Introduction

This Supplementary Material contains the Supplementary Table 2.S1 and Supplementary Figures 2.S1 through 2.S11 (with associated captions). The Supplementary Table and Figures are preceded with text briefly providing context.

Tables

Table 2.S1: SAR Data

Table 2.S1 list the dates and perpendicular baselines ($B_\perp$) of Sentinel-1 SAR data used in this study. Sentinel-1 data is accessible via the European Space Agency's Copernicus Open Access Hub (scihub.copernicus.eu).

Figures

Figure 2.S1: Interferometric Baseline Plot

Figure 2.S1 shows the perpendicular baseline of the Sentinel-1 SAR (synthetic aperture radar) image acquisitions along track 144, referenced to November 8, 2014, and the interferometric pair connections. We limited the generation of interferograms to a temporal separation of 100 days and an orbital baseline of 250 meters.

Figure 2.S2: Line-of-Sight Three Component Scaling Factors

Figure 2.S2 shows how the East, North, and Vertical components of displacement contribute to a Line-of-Sight (LOS) observation. These scaling factors are computed using the look angles for Sentinel-1 satellites, descending track 144. Sentinel-1 is sensitive to the East and Vertical components of displacement and insensitive to the North component. We use these relations to project the cGPS time series into LOS.

Figure 2.S3: Surface Fit Parameter Misfits

We searched for and selected our correction surface fit by evaluating the misfit of the residuals between GInSAR and the validation cGPS time series as a function of polynomial fit order complexities. We define the misfit to be the L_2 norm of the epoch-by-epoch differences between InSAR and LOS-projected cGPS time series for each of the 23 cGPS validation stations (Section 2.3). From these results and those in Figure 2.S5, we selected $\lambda = 150$ and Poly22 for the analysis described in this paper.

Figure 2.S4: CSBAS Connectivity Map

We implement a variation of the Small Baseline Subset algorithm (SBAS), similar to Intermittent SBAS, which we called temporally Connected SBAS (CSBAS). That is, unlike SBAS, we do not exclude pixels that exhibit a loss coherence but rather only exclude pixels if there are no valid displacement estimates spanning any particular epoch. This allows us to retain a higher density of data over regions with intermittent surface cover while avoiding the estimation time series across periods for which there is no observational constraint (Section 2.5).

Figure 2.S5: Temporal Smoothing Parameter Selection.

We searched for and selected our temporal smoothing parameter λ by evaluating the root-mean-square of the residuals between GInSAR and the 23 validation cGPS time series (Section 2.3). The RMS values were computed from a GInSAR time series using a second-order polynomial surface for interferogram correction (see Figure 2.S3) and our CSBAS inversion method. From this analysis, we selected a λ value of 150, which falls nears the region of highest curvature.

Figure 2.S6: Residual Time Series Variance

We assess the variance of the residuals between the tested referencing schemes and 23 validation cGPS time series (Section 2.3). The InSAR and cGPS time series are detrended using a robust least squares technique that iteratively reweights outliers with a bisquare weighting function. We compute the variance of the residuals between InSAR derived displacements and the validation cGPS displacements at each validation location.

Figure 2.S7: Velocity Fit Uncertainty

Using the CSBAS technique, we estimate displacement time series for each viable pixel. Using a robust least squares technique that iteratively reweights outliers with a bisquare weighting function ('robustfit' in MATLAB), we estimate the velocity for each pixel. We report the standard error associated with each velocity fit spatially. This

map demonstrates the regions with the greatest magnitude velocities (i.e. agricultural regions exhibiting subsidence) have the largest standard errors.

Figure 2.S8: Example GInSAR Corrections for Varying Numbers of cGPS Stations

We tested how the cGPS station density and configuration affected our GInSAR correction. Using a representative interferogram with noise, we compute the RMS of the residuals between the GInSAR corrected interferogram and validation cGPS displacements for tens of thousands of cGPS configurations with varying numbers of correction stations. Below are three examples of low RMS values for an input of 6, 16, and 46 stations. Their RMS values are plotted as magenta circles in Figure 2.S11.

Figure 2.S9: RMS of GInSAR Corrections for Varying Numbers of cGPS Stations

Using a representative interferogram with noise, we compute the RMS of the residuals between the GInSAR corrected interferogram and validation cGPS displacements for tens of thousands of cGPS configurations with varying numbers of input stations. For each number of allowable stations, we test all possible or up to 1000 randomly selected configurations.

Figure 2.S10: Correction Surface Convergence

Using the polynomial coefficients computed for each tested cGPS configuration

for Figure 2.S11, we estimate the robust standard deviation of the correction surfaces (second order polynomial). A lower standard deviation indicates similarity between the correction surfaces. We test this for 13 randomly selected interferograms and found a similar relationship between standard deviation and the number of cGPS stations included.

Figure 2.S11: Non-temporally Smoothed Time Series

Using the locations shown in Figure 2.5, we plot the non-temporally smoothed InSAR time series. This shows how the GInSAR method (red lines) reduce variability in the time series compared to the alternative referencing schemes.

Table 2.S1: Dates and perpendicular baselines for SAR data

Mission	Absolute Orbit	Day	Month	Year	$B_\perp$
Sentinel-1A	3191	8	11	2014	0
Sentinel-1A	3541	2	12	2014	-17.9
Sentinel-1A	3891	26	12	2014	-24.8
Sentinel-1A	4941	8	3	2015	6.4
Sentinel-1A	5291	1	4	2015	-84.2
Sentinel-1A	5641	25	4	2015	-144.1
Sentinel-1A	5991	19	5	2015	-44.8
Sentinel-1A	6341	12	6	2015	2.3
Sentinel-1A	6691	6	7	2015	-120.2
Sentinel-1A	7041	30	7	2015	4.2
Sentinel-1A	7391	23	8	2015	-27.2
Sentinel-1A	7741	16	9	2015	-116.9
Sentinel-1A	8091	10	10	2015	-50
Sentinel-1A	8441	3	11	2015	-47.1
Sentinel-1A	8616	15	11	2015	-10
Sentinel-1A	8791	27	11	2015	23.1
Sentinel-1A	8966	9	12	2015	65
Sentinel-1A	9141	21	12	2015	-50.3
Sentinel-1A	9491	14	1	2016	-82.1
Sentinel-1A	9666	26	1	2016	-94.5
Sentinel-1A	9841	7	2	2016	42.7
Sentinel-1A	10016	19	2	2016	-16.3
Sentinel-1A	10191	2	3	2016	-85.6
Sentinel-1A	10366	14	3	2016	-122
Sentinel-1A	10541	26	3	2016	-17.4
Sentinel-1A	10716	7	4	2016	-0.1
Sentinel-1A	10891	19	4	2016	-33.3
Sentinel-1A	11066	1	5	2016	-65
Sentinel-1A	11241	13	5	2016	-95.6
Sentinel-1A	11416	25	5	2016	-75.3
Sentinel-1A	11591	6	6	2016	-22.5
Sentinel-1A	11941	30	6	2016	-33.2
Sentinel-1A	12291	24	7	2016	-88
Sentinel-1A	12641	17	8	2016	-29.8
Sentinel-1A	12991	10	9	2016	-99.7
Sentinel-1A	13166	22	9	2016	-49.7
Sentinel-1A	13341	4	10	2016	-12.4
Sentinel-1A	13516	16	10	2016	-32
Sentinel-1A	13691	28	10	2016	1
Sentinel-1A	13866	9	11	2016	-45.5
Sentinel-1A	14041	21	11	2016	-50.4
Sentinel-1A	14216	3	12	2016	20.8
Sentinel-1A	14391	15	12	2016	25.1
Sentinel-1A	14566	27	12	2016	60.3
Sentinel-1A	14741	8	1	2017	-62.2
Sentinel-1B	3845	14	1	2017	39.3
Sentinel-1A	14916	20	1	2017	-124.7
Sentinel-1B	4020	26	1	2017	-1.8
Sentinel-1A	15091	1	2	2017	-92.3

The last column is the perpendicular baseline in meters relative to the November 8, 2014 reference image.

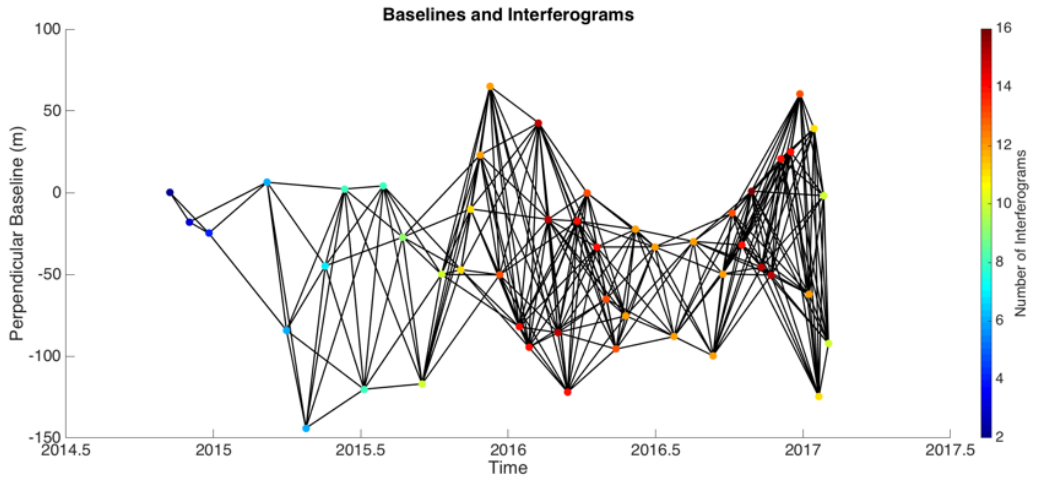

Figure 2.S1: Plot of the perpendicular baselines between acquisitions and the number of interferometric pairs each time contributes to. Circle symbols indicate the acquisition times with a perpendicular baseline using the November 8, 2014 acquisition as our master image. Color values denote number of interferograms each time contributes to where warmer colors (yellows, oranges, and reds) signify more pairs and cooler colors (blues) denote relatively fewer pairs. Black lines indicate interferometric connection between two acquisitions.

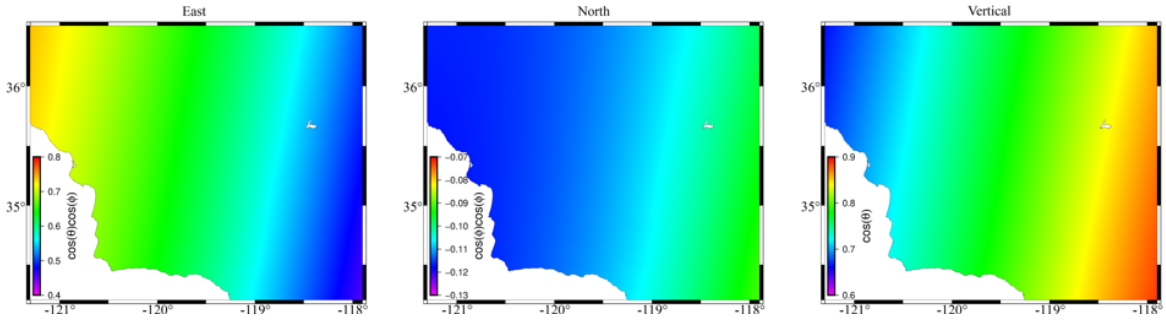

Figure 2.S2: Maps of the scaling factor for the East, North, and Vertical components of signal as seen by the Sentinel-1 satellites for track 144. The off-zenith and azimuth angles for the line of sight look vector are given by θ and ϕ respectively.

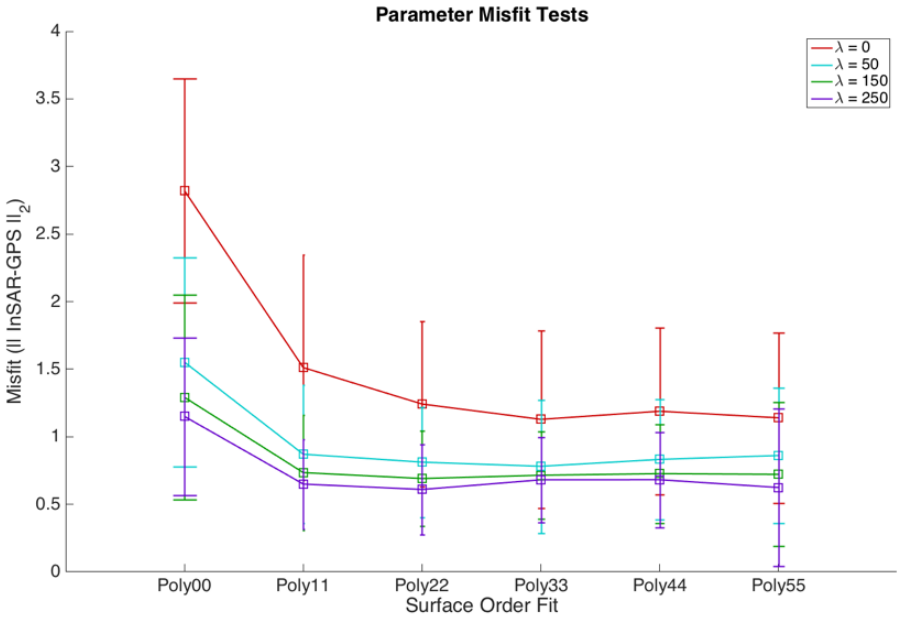

Figure 2.S3: Statistics of InSAR-cGPS time series residuals for different GInSAR polynomial fitting functions and various values of temporal smoothing (λ) for CSBAS. Square symbols indicate the median value of these norms and error bars show the interquartile range. The X-axis shows results for different surface fits with complexity increasing to the right (Poly00 corresponds to a zeroth order polynomial in latitude and longitude while Poly 55 is a fifth order polynomial in each direction). Colors correspond to the temporal smoothing value applied.

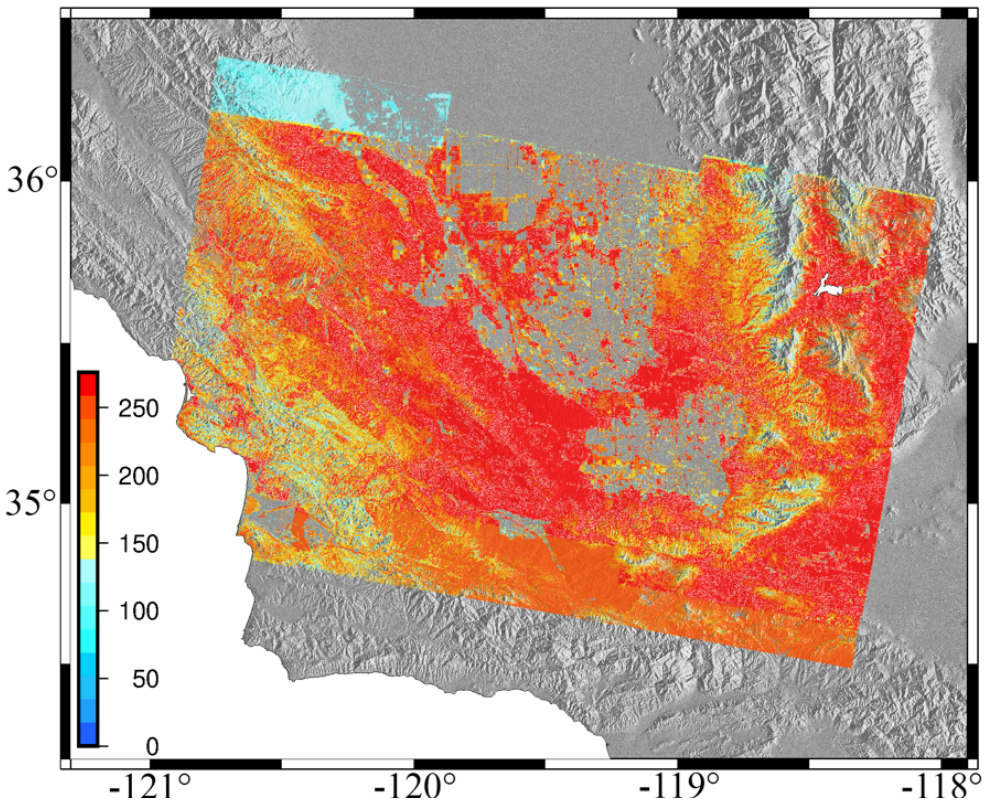

Figure 2.S4: Connectivity Map showing the data density and pixels used for time series construction. Pixels with color values indicate locations where there is no temporal gap in data coverage. Color values show the number of interferometric pairs that were used for time series construction at each pixel.

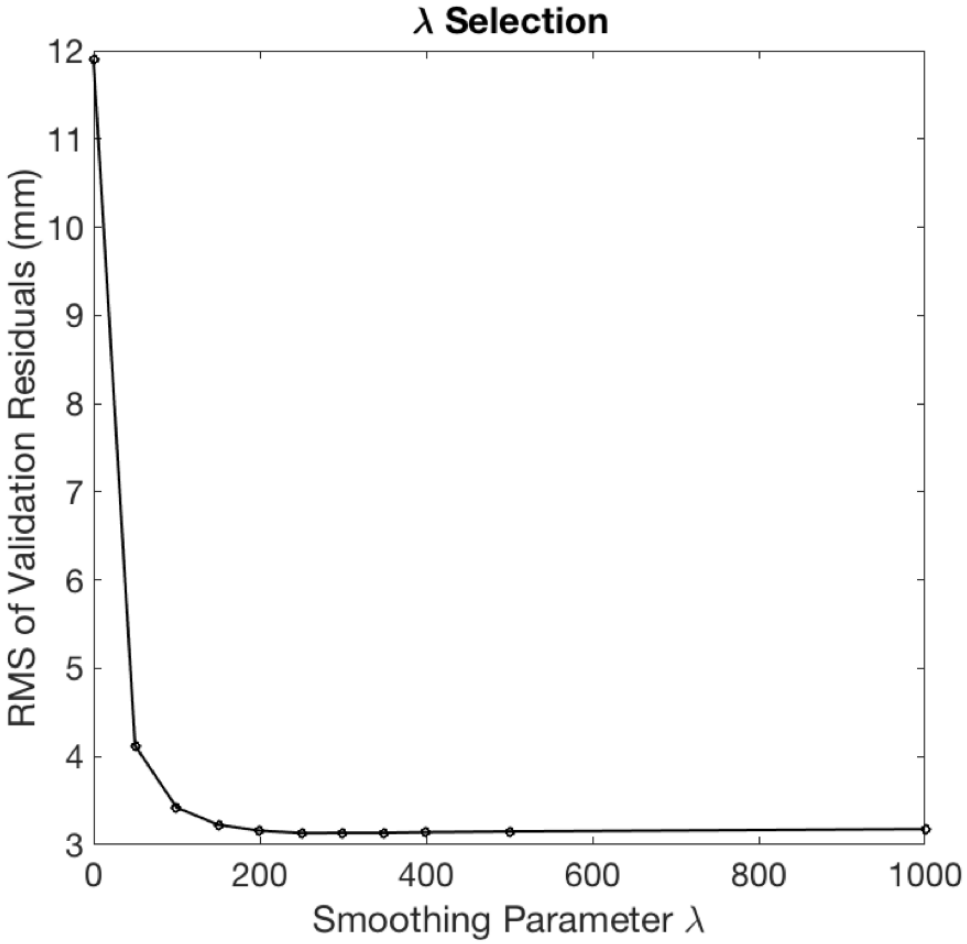

Figure 2.S5: Root-mean-square of the residuals between GInSAR displacement time series and LOS-projected position time series of the validation cGPS stations as a function of smoothing parameter λ.

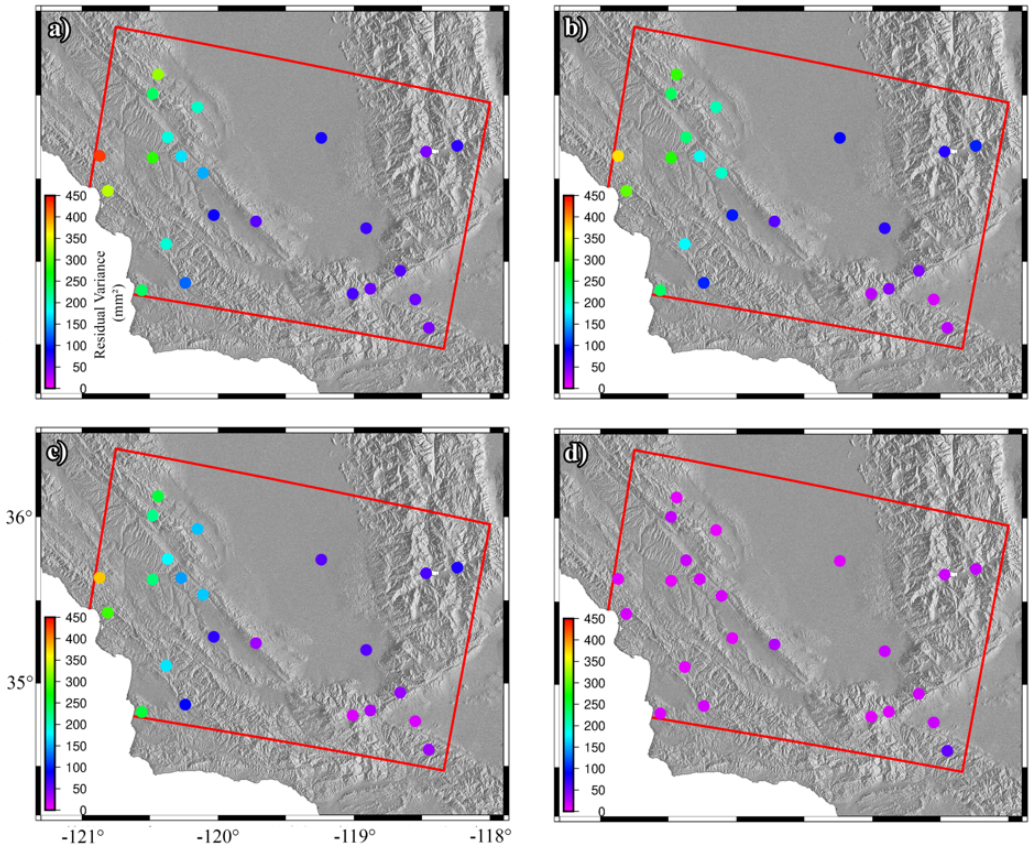

Figure 2.S6: Residual Maps at cGPS validation stations. Maps show the residual variance between detrended InSAR and cGPS time series at validation cGPS station locations (circle symbols) for the a) "Uncorrected," b) "Pinned at ground" (at P560), c) "Pinned at GPS" (at P560), and d) GInSAR results. Colors represent the residual variance (mm^2) with warm colors (reds and yellows) indicate poor agreement between the two datasets and cool colors (blues and purples) suggest closer agreement.

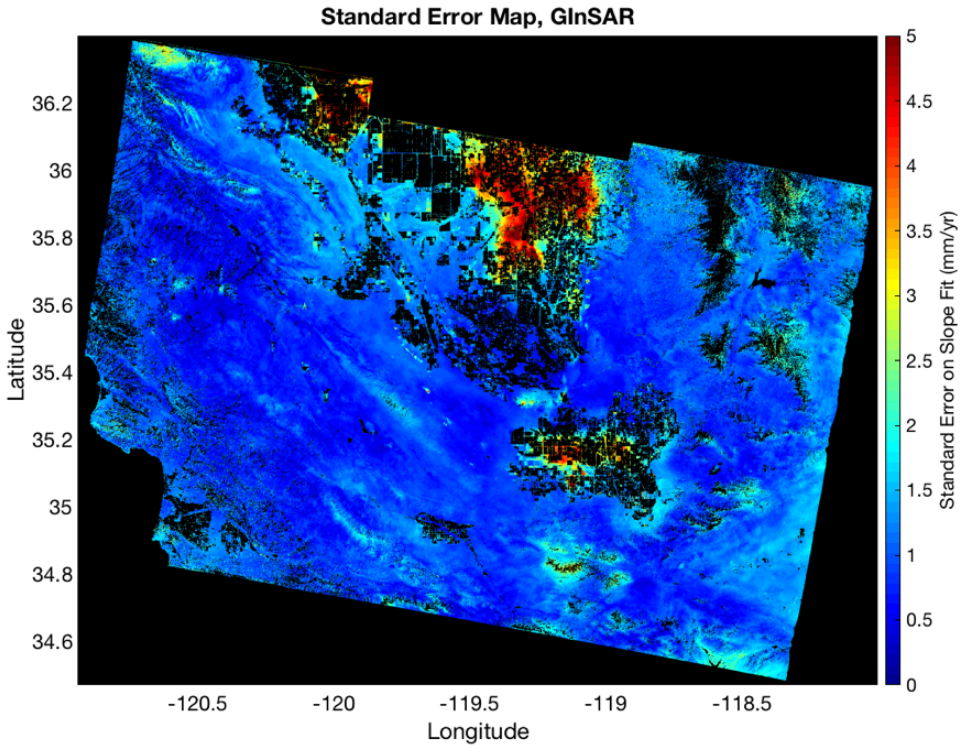

Figure 2.S7: Spatial map of the standard error associated to the linear velocity estimation.

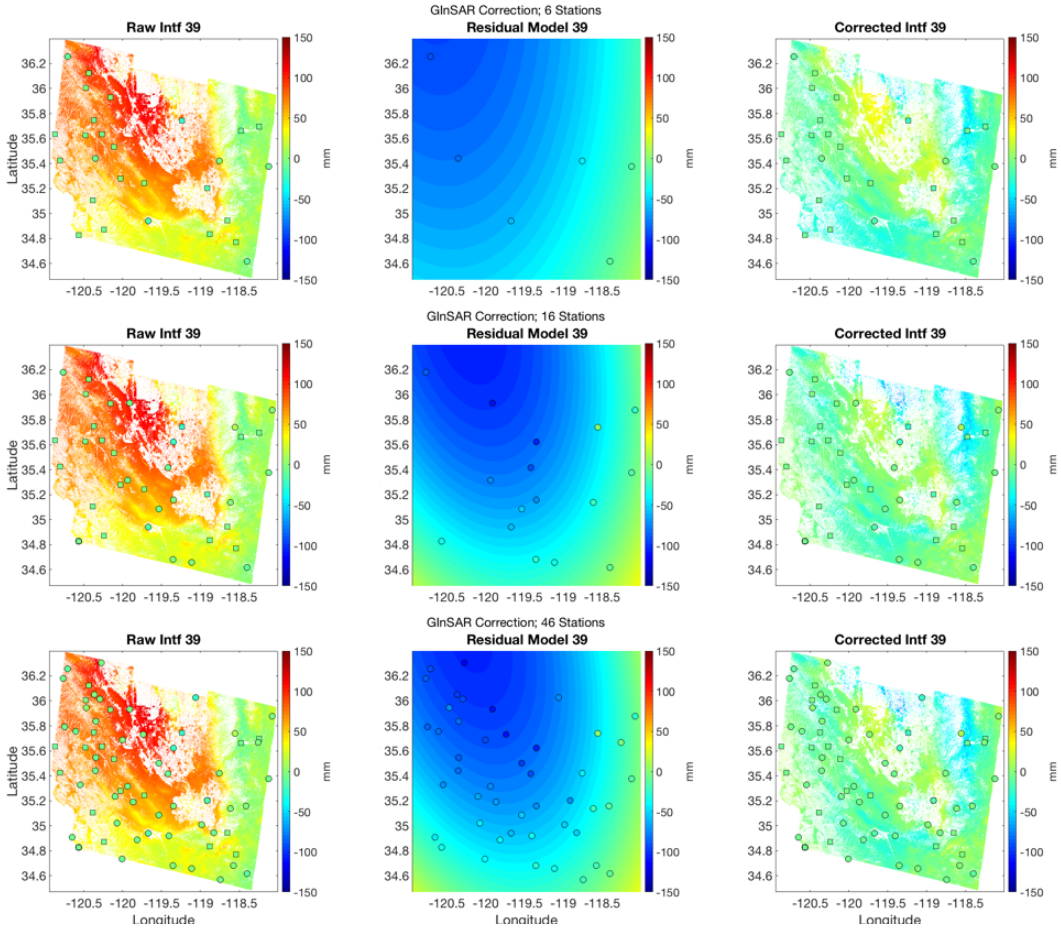

Figure 2.S8: Maps of GInSAR correction using 6, 16, and 46 cGPS stations. The left panels show the raw interferogram spanning the times March 2 – June 6, 2016. Symbols indicate cGPS locations and displacement values. Circles correspond to the cGPS stations used in the correction and squares are the validation cGPS stations. The center panels show the second order polynomial fit to the residuals between InSAR and cGPS. Colors indicate residual values. The right panels show the corrected interferogram, symbols same as left pane

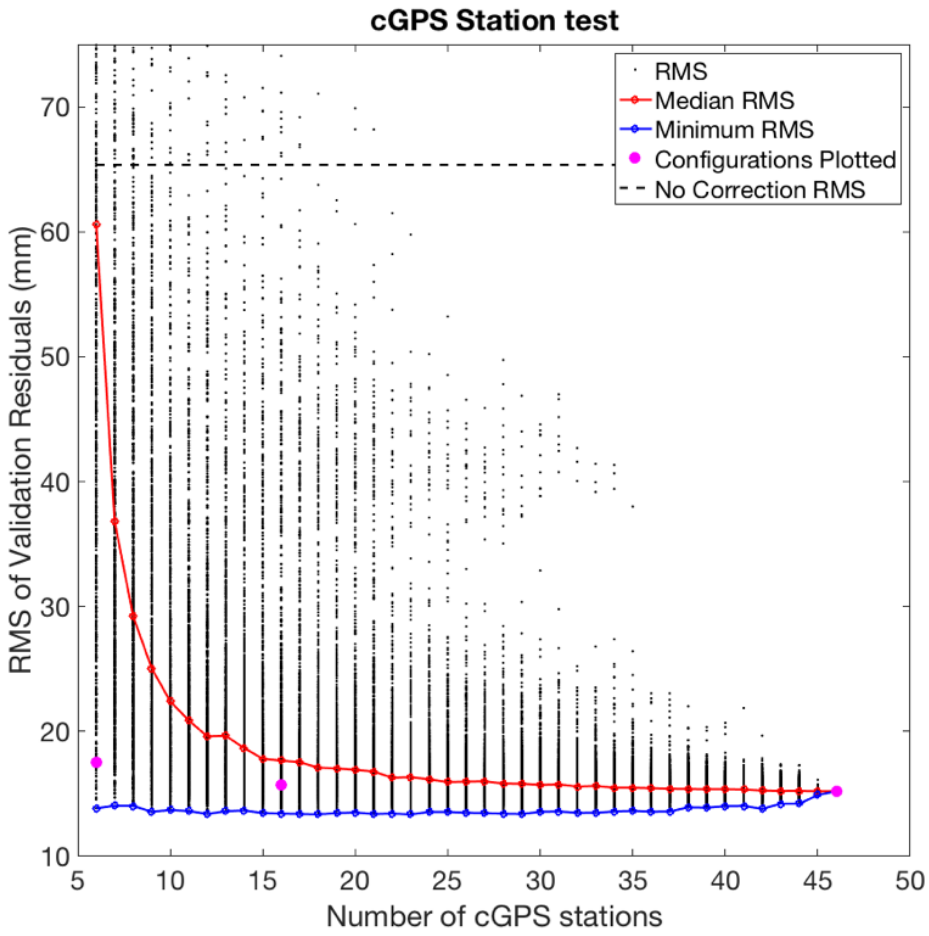

Figure 2.S9: Plot of root-mean-square of residuals between validation cGPS and GInSAR for different configurations of stations as a function of number of stations for interferogram 39 (spanning March 2 – June 6, 2016). Black dots are the RMS for different cGPS configurations used to correct the interferogram. Dashed black line is the RMS for when no correction applied. Red line is the median RMS for each number of stations. Blue line is the minimum RMS per number of stations. Magenta circles are values of RMS for the configurations using 6, 16, and 46 cGPS stations plotted in Figure 2.S10.

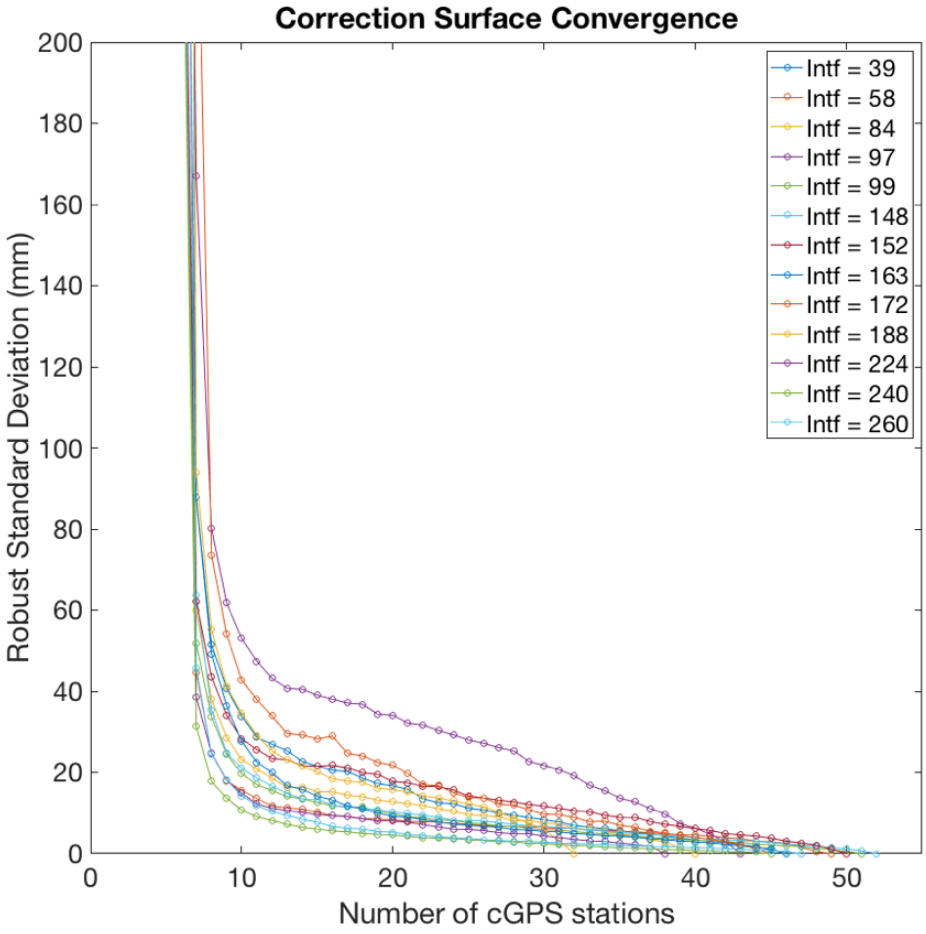

Figure 2.S10: Plot of the robust standard deviations for correction surfaces (residual models) as a function of number of cGPS stations used. Different colored lines correspond to different interferograms tested (randomly selected).

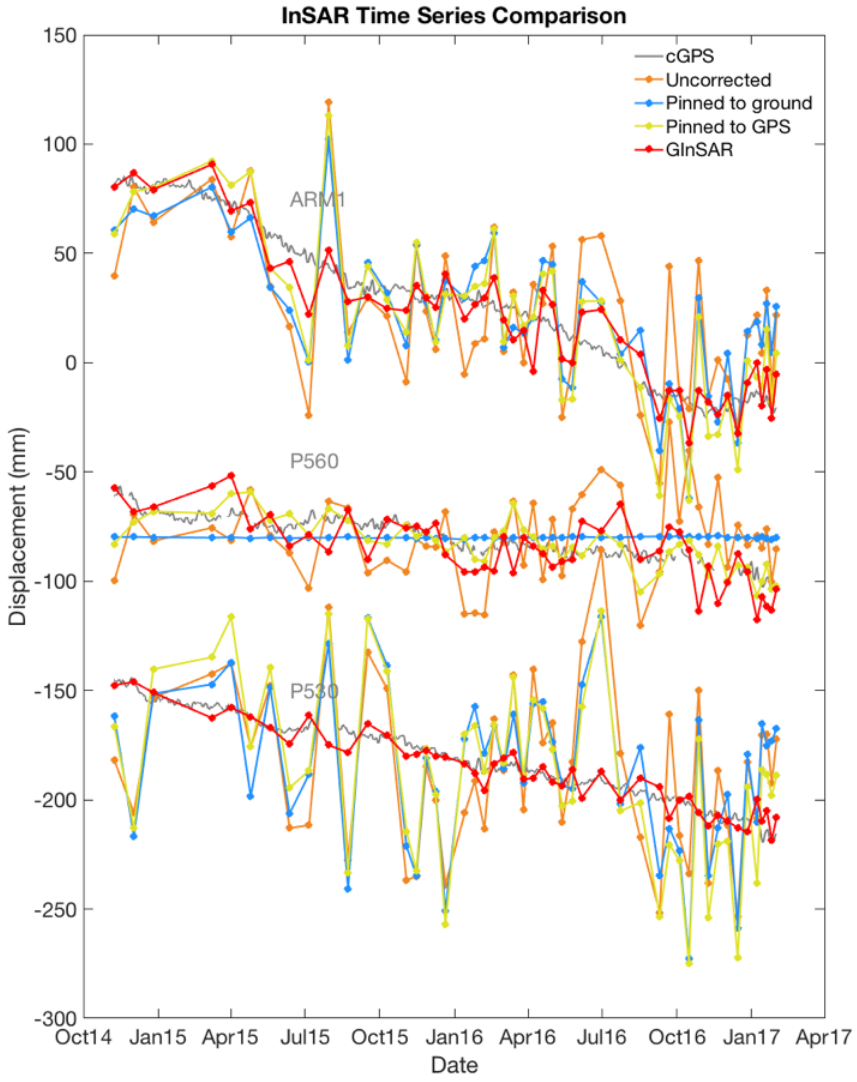

Figure 2.S11: Time series comparisons of the four tested referencing techniques and collocated cGPS time series at stations ARM1, P560, and P530 with no temporal smoothing applied. Same time series locations as Figure 2.5 in main text. ARM1 is one of the stations used in the correction for GInSAR and is located in a region of subsidence. P560 is used as the pinning location for "Pinned to Ground" and "Pinned to cGPS". P530 is a cGPS location independent from the pinning schemes and is used in the validation.

References

Amelung, F., D. L. Galloway, J. W. Bell, H. A. Zebker, and R. J. Laczniak (1999), Sensing the ups and downs of Las Vegas: InSAR reveals structural control of land subsidence and aquifer-system deformation, *Geology*, *27*(6), 483–486, doi:10.1130/0091-7613(1999)027⟨0483:STUADO⟩2.3.CO;2.

Argus, D. F., M. B. Heflin, G. Peltzer, F. Crampé, and F. H. Webb (2005), Interseismic strain accumulation and anthropogenic motion in metropolitan Los Angeles, *Journal of Geophysical Research: Solid Earth*, *110*(B4), B04,401, doi:10.1029/2003JB002934.

Bateson, L., F. Cigna, D. Boon, and A. Sowter (2015), The application of the Intermittent SBAS (ISBAS) InSAR method to the South Wales Coalfield, UK, *International Journal of Applied Earth Observation and Geoinformation*, *34*, 249–257, doi:10.1016/j.jag.2014.08.018.

Ben-Israel, A., and T. N. E. Greville (2003), *Generalized Inverses: Theory and Applications*, Springer Science & Business Media.

Berardino, P., G. Fornaro, R. Lanari, and E. Sansosti (2002), A new algorithm for surface deformation monitoring based on small baseline differential SAR interferograms, *IEEE Transactions on Geoscience and Remote Sensing*, *40*(11), 2375–2383, doi:10.1109/TGRS.2002.803792.

Borsa, A. A., J.-B. Minster, B. G. Bills, and H. A. Fricker (2007), Modeling long-period noise in kinematic GPS applications, *Journal of Geodesy*, *81*(2), 157–170, doi:10.1007/s00190-006-0097-x.

Chaussard, E., R. Bürgmann, M. Shirzaei, E. J. Fielding, and B. Baker (2014), Predictability of hydraulic head changes and characterization of aquifer-system and fault properties from InSAR-derived ground deformation, *Journal of Geophysical Research: Solid Earth*, *119*(8), 2014JB011,266, doi:10.1002/2014JB011266.

Chen, C. W., and H. A. Zebker (2001), Two-dimensional phase unwrapping with use of statistical models for cost functions in nonlinear optimization, *Journal of the Optical Society of America A*, *18*(2), 338–351, doi:10.1364/JOSAA.18.000338.

De Zan, F., and A. M. Guarnieri (2006), TOPSAR: Terrain Observation by Progressive Scans, *IEEE Transactions on Geoscience and Remote Sensing*, *44*(9), 2352–2360, doi:10.1109/TGRS.2006.873853.

DeMets, C., R. G. Gordon, D. F. Argus, and S. Stein (1990), Current plate motions, *Geophysical Journal International*, *101*(2), 425–478, doi:10.1111/j.1365-246X.1990.tb06579.x.

DeMets, C., R. G. Gordon, D. F. Argus, and S. Stein (1994), Effect of recent revisions to the geomagnetic reversal time scale on estimates of current plate motions, *Geophysical Research Letters*, *21*(20), 2191–2194, doi:10.1029/94GL02118.

Farr, T. G., P. A. Rosen, E. Caro, R. Crippen, R. Duren, S. Hensley, M. Kobrick, M. Paller, E. Rodriguez, L. Roth, D. Seal, S. Shaffer, J. Shimada, J. Umland, M. Werner, M. Oskin, D. Burbank, and D. Alsdorf (2007), The Shuttle Radar Topography Mission, *Reviews of Geophysics*, *45*(2), RG2004, doi:10.1029/2005RG000183.

Fatland, D. R., and C. S. Lingle (2002), InSAR observations of the 1993–95 Bering Glacier (Alaska, U.S.A.) surge and a surge hypothesis, *Journal of Glaciology*, *48*(162), 439–451, doi:10.3189/172756502781831296.

Fialko, Y. (2006), Interseismic strain accumulation and the earthquake potential on the southern San Andreas fault system, *Nature*, *441*(7096), 968–971, doi:10.1038/nature04797.

Gourmelen, N., F. Amelung, and R. Lanari (2010), Interferometric synthetic aperture radar–GPS integration: Interseismic strain accumulation across the Hunter Mountain fault in the eastern California shear zone, *Journal of Geophysical Research: Solid Earth*, *115*(B9), B09,408, doi:10.1029/2009JB007064.

Hanssen, R. F. (2001), *Radar Interferometry: Data Interpretation and Error Analysis*, Springer Science & Business Media.

Herring, T. A. (1992), Modeling atmospheric delays in the analysis of space geodetic data, in *Proceedings of the Symposium: Refraction of Transatmospheric Signals in Geodesy*, pp. 157–164.

Herring, T. A., T. I. Melbourne, M. H. Murray, M. A. Floyd, W. M. Szeliga, R. W. King, D. A. Phillips, C. M. Puskas, M. Santillan, and L. Wang (2016), Plate Boundary Observatory and related networks: GPS data analysis methods and geodetic products, *Reviews of Geophysics*, *54*(4), 2016RG000,529, doi:10.1002/2016RG000529.

Hooper, A., H. Zebker, P. Segall, and B. Kampes (2004), A new method for measuring deformation on volcanoes and other natural terrains using InSAR persistent scatterers, *Geophysical Research Letters*, *31*(23), doi:10.1029/2004GL021737.

Liu, L., K. Schaefer, T. Zhang, and J. Wahr (2012), Estimating 1992–2000 average active layer thickness on the Alaskan North Slope from remotely sensed surface subsidence, *Journal of Geophysical Research: Earth Surface*, *117*(F1), F01,005, doi:10.1029/2011JF002041.

Massonnet, D., and K. L. Feigl (1998), Radar interferometry and its application to changes in the Earth's surface, *Reviews of Geophysics*, *36*(4), 441–500, doi:10.1029/97RG03139.

Melbourne, W. (1985), The case for ranging in GPS-based geodetic systems, in *Proc. 1st Symp. Precise Positioning Global Positioning Syst. Positioning (GPS)*, pp. 373–386.

Rebischung, P., J. Griffiths, J. Ray, R. Schmid, X. Collilieux, and B. Garayt (2012), IGS08: the IGS realization of ITRF2008, *GPS Solutions*, *16*(4), 483–494, doi:10.1007/s10291-011-0248-2.

Sandwell, D., R. Mellors, X. Tong, M. Wei, and P. Wessel (2011), Open radar interferometry software for mapping surface Deformation, *Eos, Transactions American Geophysical Union*, *92*(28), 234–234, doi:10.1029/2011EO280002.

Sandwell, D. T., Y. Zeng, Z.-K. Shen, B. Crowell, J. Murray, R. McCaffrey, and X. Xu (2016), The SCEC community geodetic model V1: Horizontal velocity grid, *SCEC Annu. Meeting*.

Shirzaei, M., and R. Bürgmann (2018), Global climate change and local land subsidence exacerbate inundation risk to the San Francisco Bay Area, *Science Advances*, *4*(3), eaap9234, doi:10.1126/sciadv.aap9234.

Shirzaei, M., R. Bürgmann, and E. J. Fielding (2017), Applicability of Sentinel-1 Terrain Observation by Progressive Scans multitemporal interferometry for monitoring slow ground motions in the San Francisco Bay Area, *Geophysical Research Letters*, *44*(6), 2733–2742, doi:10.1002/2017GL072663.

Sowter, A., L. Bateson, P. Strange, K. Ambrose, and M. F. Syafiudin (2013), DInSAR estimation of land motion using intermittent coherence with application to the South Derbyshire and Leicestershire coalfields, *Remote Sensing Letters*, *4*(10), 979–987, doi:10.1080/2150704X.2013.823673.

Tong, X., and D. Schmidt (2016), Active movement of the Cascade landslide complex in Washington from a coherence-based InSAR time series method, *Remote Sensing of Environment*, *186*, 405–415, doi:10.1016/j.rse.2016.09.008.

Tong, X., D. T. Sandwell, and B. Smith-Konter (2013), High-resolution interseismic velocity data along the San Andreas Fault from GPS and InSAR, *Journal of Geophysical Research: Solid Earth*, *118*(1), 369–389, doi:10.1029/2012JB009442.

Torres, R., P. Snoeij, D. Geudtner, D. Bibby, M. Davidson, E. Attema, P. Potin, B. Rommen, N. Floury, M. Brown, I. N. Traver, P. Deghaye, B. Duesmann, B. Rosich, N. Miranda, C. Bruno, M. L'Abbate, R. Croci, A. Pietropaolo, M. Huchler, and F. Rostan (2012), GMES Sentinel-1 mission, *Remote Sensing of Environment*, *120*, 9–24, doi:10.1016/j.rse.2011.05.028.

Tymofyeyeva, E., and Y. Fialko (2015), Mitigation of atmospheric phase delays in InSAR data, with application to the eastern California shear zone, *Journal of Geophysical Research: Solid Earth*, *120*(8), 2015JB011,886, doi:10.1002/2015JB011886.

Wei, M., and D. T. Sandwell (2010), Decorrelation of L-Band and C-Band Interferometry Over Vegetated Areas in California, *IEEE Transactions on Geoscience and Remote Sensing*, *48*(7), 2942–2952, doi:10.1109/TGRS.2010.2043442.

Wei, M., D. Sandwell, and B. Smith-Konter (2010), Optimal combination of InSAR and GPS for measuring interseismic crustal deformation, *Advances in Space Research*, *46*(2), 236–249, doi:10.1016/j.asr.2010.03.013.

Wubbena, G. (1985), Software developments for geodetic positioning with GPS using TI 4100 code and carrier measurements, in *Proc. 1st Symp. Precise Positioning Global Positioning Syst. Positioning (GPS)*, pp. 403–412.

Wyatt, F. K. (1989), Displacement of surface monuments: Vertical motion, *Journal of Geophysical Research: Solid Earth*, *94*(B2), 1655–1664, doi:10.1029/JB094iB02p01655.

Xu, X., D. T. Sandwell, E. Tymofyeyeva, A. González-Ortega, and X. Tong (2017), Tectonic and Anthropogenic Deformation at the Cerro Prieto Geothermal Step-Over Revealed by Sentinel-1A InSAR, *IEEE Transactions on Geoscience and Remote Sensing*, *PP*(99), 1–9, doi:10.1109/TGRS.2017.2704593.

Yu, C., Z. Li, N. T. Penna, and P. Crippa (2018), Generic Atmospheric Correction Model for Interferometric Synthetic Aperture Radar Observations, *Journal of Geophysical Research: Solid Earth*, *123*(10), 9202–9222, doi:10.1029/2017JB015305.

Zebker, H. A., P. A. Rosen, and S. Hensley (1997), Atmospheric effects in interferometric synthetic aperture radar surface deformation and topographic maps, *Journal of Geophysical Research: Solid Earth*, *102*(B4), 7547–7563, doi:10.1029/96JB03804.

Chapter 3

Characterization of Groundwater Recharge and Flow in California's San Joaquin Valley From InSAR-Observed Surface Deformation

Abstract

Surface deformation in California's Central Valley (CV) has long been linked to changes in groundwater storage. Recent advances in remote sensing have enabled

the mapping of CV deformation and associated changes in groundwater resources at increasingly higher spatiotemporal resolution. Here, we use interferometric synthetic aperture radar (InSAR) from the Sentinel-1 missions, augmented by continuous Global Positioning System (cGPS) positioning, to characterize the surface deformation of the San Joaquin Valley (SJV, southern two-thirds of the CV) for consecutive dry (2016) and wet (2017) water years. We separate trends and seasonal oscillations in deformation time series and interpret them in the context of surface and groundwater hydrology. We find that subsidence rates in 2016 (mean -42.0 mm/yr; peak -345 mm/yr) are twice that in 2017 (mean -20.4 mm/yr; peak -177 mm/yr), consistent with increased groundwater pumping in 2016 to offset the loss of surface-water deliveries. Locations of greatest subsidence migrated outwards from the valley axis in the wetter 2017 water year, possibly reflecting a surplus of surface-water supplies in the lowest portions of the SJV. Patterns in the amplitude of seasonal deformation and the timing of peak seasonal uplift reveal entry points and potential pathways for groundwater recharge into the SJV and subsequent groundwater flow within the aquifer. This study provides novel insight into the SJV aquifer system that can be used to constrain groundwater-flow and subsidence models, which has relevance to groundwater management in the context of California's 2014 Sustainable Groundwater Management Act (SGMA).

3.1 Introduction

California's Central Valley (CV) is a major agricultural production center with an economic output of tens of billions of dollars (USD) annually (*Howitt et al.*, 2015). Because agricultural water demand exceeds supply from precipitation and surface water even in climatologically wet years (*Faunt et al.*, 2016), groundwater is a key resource for CV water users. Periods of prolonged and intense drought threaten economic and agricultural production by limiting access to surface-water supplies, which motivates increased reliance on groundwater (*Hanson et al.*, 2012). This was particularly evident in the semi-arid southern two-thirds of the CV (the San Joaquin Valley or SJV) during the 2012-2016 drought (*Lund et al.*, 2018). Sustained dependency on groundwater resources, such as occurs in the SJV, may jeopardize future groundwater availability if extraction persistently exceeds aquifer recharge (*Scanlon et al.*, 2012).

The hydrological system of SJV is diverse in terms of availability, storage, and conveyance. During an average water year (WY; October 1 to September 30), the SJV receives most of its precipitation between November and April (∼85%), with half occurring between December and February (*Williamson et al.*, 1989; *Faunt*, 2009). Geographically, this precipitation typically falls on the western slopes of the Sierra Nevada as rain and snow, and much of that which does not directly run off is stored in seasonal snowpack, soil moisture, and groundwater (*Enzminger et al.*, 2019). Much of the drainage from these sources of water storage funnels into streams and rivers, with about 84% of the total unimpaired streamflow (surface-water runoff not regulated by

dams, reservoirs, or conveyance systems) entering the SJV from January through June (*Williamson et al.*, 1989). Water is transported from north to south and from east to west via conveyance systems such as the California Aqueduct and the Friant-Kern Canal (Figure 3.1). Networks of canals and artificial waterways distribute surface water from these primary diversions and natural streamflow throughout the valley for agricultural, industrial, and urban use.

Inter-annual variation in surface-water availability, as well as within-year differences in the timing of natural (river) and imported (state and federal project) surface water, plays an important role in SJV water use and groundwater recharge. In an average water year, surface water accounts for ∼60% of water demand with groundwater supplementing the remaining ∼40% (*Faunt et al.*, 2016). During dry or drought years, more groundwater is typically used (some years accounting for as much as 70% of the demand) due to reduced surface-water availability e.g. (*Faunt et al.*, 2016). In the dry WY2016, for example, total unimpaired and natural local inflows to the San Joaquin Valley (San Joaquin and Tulare Lake basins) totaled 7,167 thousand acre-feet (TAF) while state and federal projects imported 3,476 TAF. This is in contrast with wet years, such as WY2017, where total natural inflows were 22,530 TAF and imports from state and federal projects were 6,431 TAF (*Public Policy Institute of California*, 2019). During these wet years, surface-water use increases while groundwater use declines, with excess surface water available for groundwater banking (*Scanlon et al.*, 2016) and natural recharge (*Faunt*, 2009; *Meixner et al.*, 2016). Generally, SJV natural inflows peak in March, while project water imports peak months later in July at the height of surface-

water irrigation (*U.S. Bureau of Reclamation*, 2020). Thus, both the dry and wet year magnitudes of local and imported supplies, and differences in their timing, are expected to be reflected in recharge dynamics. To better understand the resiliency of groundwater reservoirs for future use, there is a great need for assessing how and where both natural and artificial aquifer recharge occurs, whether via managed recharge, return flow from irrigation, direct precipitation, or river runoff.

Directly observing the state of aquifer systems remains challenging because of the sparsity of quality *in-situ* point measurements (both in time and space). However, groundwater extraction and recharge induce Earth surface displacements that can be observed using geodetic techniques. In sedimentary basins such as the SJV, surface displacements are often attributed to the expansion or compaction of the aquifer system in response to pore pressure variations (*Poland and Davis*, 1969). This poroelastic deformation is governed by the law of effective stress (*Terzaghi*, 1925), which is directly related to groundwater levels (hydraulic head). Furthermore, poroelastic deformation can be inelastic or elastic. Wherever the effective stress within the aquifer-system matrix exceeds the preconsolidation stress, often taken to be the lowest previous level of hydraulic head, a new preferred grain realignment with reduced capacity for water storage may result (*Leake*, 1990). For fine-grained deposits such as clay and silt, this consolidation can lead to inelastic deformation, which is manifested as permanent land subsidence (*Leake*, 1990). Changes in hydraulic head that do not result in irreversible realignment of grains result in elastic deformation, which includes reversible land subsidence or uplift.

The sediment-filled trough that is the SJV aquifer system can be described as an

interbedded mix of sand and gravel with finer-grained deposits of clay and silt (*Page*, 1986). Deposited as coalescing alluvial fans, there are generally thicker lenses of coarser grained sediments at the valley margins and a higher clay content nearer the valley axis (*Page*, 1986). Clay and silt deposits are particularly susceptible to inelastic deformation, resulting in observed subsidence of as much as tens of centimeters annually in the SJV e.g., (*Faunt et al.*, 2016). While the link between recent land surface subsidence and groundwater extraction in the SJV has been well documented and attributed to the inelastic aquifer-system response to pumping (*Farr and Zhen*, 2014; *Faunt et al.*, 2016; *Smith et al.*, 2017; *Murray and Lohman*, 2018; *Ojha et al.*, 2018, 2019; *Jeanne et al.*, 2019; *Chaussard and Farr*, 2019), the relatively subtle surface uplift response related to the recovery of local groundwater levels at sub-annual time scales has not been extensively studied.

In 2014, California passed the Sustainable Groundwater Management Act (SGMA) to protect its groundwater resources. To understand the evolution of groundwater resources under natural and human forcing, it is critical to characterize and monitor the aquifer-system response to variable climatological regimes and with respect to anthropogenic management over short (< 1 year) and long (≥ 1 year) time periods. Here, we leverage continuous Global Positioning System (cGPS) daily positions and interferometric synthetic aperture radar (InSAR) techniques (*Neely et al.*, 2020) to evaluate the time evolution of SJV surface deformation associated with changes in groundwater levels across dry and wet water years. We present a new methodology for investigating the elastic (reversible) deformation associated with the seasonal response of the aquifer

system by analyzing both the magnitude and timing of peak seasonal surface uplift at high spatial resolution (100 m). Interpreting our results in the context of relevant hydrological features and data, we provide insight into the movement of water through the SJV aquifer system, with relevance to groundwater management.

3.2 Data and Methods

3.2.1 InSAR Displacements

Our study region spans the southern Central Valley from 34.4°N to 37.9°N. For this analysis, synthetic aperture radar (SAR) scenes from the European Space Agency's Sentinel-1A/B mission (descending track 144; Figure 3.1) are merged along track to construct 51 extra-long images spanning 1 April 2015 to 23 October 2017 (Table 3.S1). Using the GMTSAR software package (*Sandwell et al.*, 2011; *Xu et al.*, 2017), we generate a suite of 263 interferograms (difference in carrier signal phase between SAR images), geometrically aligned to a primary reference image on 17 August 2016. For the purpose of interferogram construction, a maximum perpendicular baseline of 250 m and a maximum 100-day separation is imposed between SAR acquisitions (Figure 3.S1; Table 3.S2). The 1 arc second digital elevation model (DEM) from the Shuttle Radar Topography Mission (SRTM) (*Farr et al.*, 2007) is used to remove the topographic phase contribution from each interferogram. To remove observed burst discontinuities from misregistration, we used the enhanced spectral diversity (ESD) algorithm (*Prats-Iraola et al.*, 2012) available in GMTSAR. Finally, interferograms are unwrapped using the Snaphu algorithm (*Chen*

and Zebker, 2000) with pixel correlation of 0.1 and subsequently converted to line-of-sight (LOS) displacements (∼100 m resolution).

3.2.2 InSAR Correction Using cGPS

Since InSAR estimates are affected by atmospheric, orbital, and processing errors, we augment interferometric displacements with independent surface displacements from 89 cGPS stations located within the study region (Figure 3.1; Table 3.S3). We obtain daily time series of post-processed position data for these stations from the National Science Foundation's Geodesy Advancing Geosciences and EarthScope (GAGE) facility (*Herring et al.*, 2016), then a) correct for offsets from equipment and other non-geophysical changes, b) smooth using a 6-day Gaussian filter to minimize high frequency signals that are likely due to multipath and tropospheric effects (*Borsa et al.*, 2007), and c) project the three components of cGPS displacements into the SAR LOS direction. For a given interferometric pair, the cGPS displacements spanning the dates of the associated SAR images are computed. We take the difference between the cGPS and InSAR displacements at each station location to create a set of residuals, to which we fit a low-order polynominal surface (second order in longitude and fourth order in latitude, empirically selected based on strategies presented in (*Neely et al.*, 2020); Figure 3.S2). This surface is separately calculated for and subtracted from each interferogram to correct long-wavelength error. This methodology (GPS-enhanced InSAR or GInSAR, (*Neely et al.*, 2020)) has the additional benefit of aligning interferometric pairs to the absolute reference provided by the cGPS.

3.2.3 InSAR Time Series Construction

To construct the deformation time series of the SJV study area from our set of corrected interferograms, we implement a modified version of the Small Baseline Subset (SBAS) algorithm (*Berardino et al.*, 2002). Standard SBAS requires pixels to be coherent in every interferogram, which is well suited for urban or rocky terrain where loss of coherence between SAR scenes is minimal. To improve coverage over highly decorrelated vegetated regions such as the agricultural fields in the SJV, we employ a newer algorithm (temporally Connected SBAS, or CSBAS) that estimates displacement for all pixels for which there is at least one valid displacement estimate spanning every interval of the time series (*Neely et al.*, 2020). We apply a temporal smoother to the least-squares CSBAS estimation via a first-order Tikhonov regularization, with the weight of the smoothing constraint $\lambda = 150$, to minimize large changes in displacement velocity often attributed to the turbulent component of atmospheric noise (*Schmidt and Bürgmann*, 2003; *Wang et al.*, 2019). Validation of the CSBAS time series with an independent set of 28 cGPS velocities and time series show good agreement (Table 3.S4).

To isolate the vertical component of displacement, we remove LOS-projected horizontal motion from the Southern California Earthquake Center (SCEC) Community Geodetic Model (CGM) (*Sandwell et al.*, 2016). Inspection of the seasonal amplitudes for cGPS vertical and horizontal components projected into LOS in this region show that the horizontal amplitudes (median value 0.36 mm and 0.12 mm for East and North respectively) are about an order of magnitude smaller than the vertical amplitudes (me-

dian value 3.12 mm). Thus, we consider this approach to be valid and we project the horizontal-corrected LOS residual into the vertical component of displacement by dividing by the cosine of the radar incidence angle.

3.2.4 InSAR Time Series Modeling

To evaluate the annual seasonal response of surface deformation (hereafter referred to simply as "seasonal"), the displacement time series are modeled for each water year at each CSBAS pixel as a linear trend and a single sinusoid described by

$$Y(t) = vt + A\cos\left(2\pi(t - T)\right) + Y_0 \tag{3.1}$$

where $Y(t)$ is our observed surface displacement (mm), t is time in fractional years, v is the linear rate of displacement (mm/yr), A is the seasonal amplitude (mm), T is the time of maximum uplift (in fractional year, where $T = 0$ corresponds to October 1), and Y_0 is a constant shift in the model (mm). We solve equation 1 using least-squares minimization and then map A and T across our study region to investigate spatial patterns in the seasonal signal.

3.2.5 Spatiotemporal Evolution of Seasonal Uplift

The solution to equation 3.1, offers unique insights into the timing of seasonal signals and how they vary across the SJV. For the purpose of this analysis, we assume the peak uplift time T corresponds to the time of maximum instantaneous aquifer pore pressure. By mapping T across the SJV, we are able to observe the spatial evolution of

peak uplift time, and thus the temporal propagation of aquifer pressure. Additionally, the spatial gradient of T indicates the directionality of the subsurface pressure front, which can distinguish the geometry and location of focused groundwater recharge zones.

To estimate this gradient, we convert T(lat,lon) from fractional year into "day of year" relative to the start of the water year (hereafter referred to as "phase" or "p"). We then apply a 2.5 km radius median filter on the phase, p(lat,lon), to smooth over smaller spatial scale features and capture the general behavior of phase progression. For each water year, we take the two-dimensional numerical gradient of this filtered phase P(lat,lon):

$$\nabla P = \frac{\partial P}{\partial \mathrm{E}}\hat{\imath} + \frac{\partial P}{\partial \mathrm{N}}\hat{\jmath} \tag{3.2}$$

where $\frac{\partial P}{\partial \mathrm{E}}$ is the difference in the longitudinal (East) direction, and $\frac{\partial P}{\partial \mathrm{N}}$ is the difference in the latitudinal (North) direction. We unit-normalize ∇P, giving a vector that indicates the lateral direction of (peak) uplift over time. Following the same steps, we calculate the local topographic gradient, ∇P_{topo}, from the SRTM DEM (*Farr et al.*, 2007) to determine the approximate direction of uninterrupted surface-water drainage. For shallower groundwater systems in particular, the water table may represent a subdued replica of topography where streams and rivers can provide locations for efficient groundwater recharge or discharge. Thus, the consideration of the topographic gradients, along with river traces, is important in the interpretation of the seasonal uplift timing progression. While recent land subsidence has modified the land surface elevation since SRTM data collection, these effects are relatively small compared to the topographic slope and

gradient differences are generally confined to the valley axis (Figure 3.S3).

3.2.6 Hydrological Data

While geodetic time series from cGPS and InSAR have expanded our understanding of the SJV aquifer system, they are best intrepreted together with hydrological data. We use stream and river traces (average annual streamflow > 0.5 m^3/s) from the U.S. Geological Survey's (USGS) Elevation Derivatives for National Applications database and the outlines of the California Aqueduct and Friant-Kern Canal (provided by the U.S. Bureau of Reclamation [USBR]) to relate natural and artificial surface-water flow patterns to spatial features observed in the displacement data. In particular, we compare the timing of peak seasonal uplift with the surface flow paths inferred from the SRTM DEM (*Farr et al.*, 2007) and watershed boundaries (hydrologic units code level 8; HUC8) from USGS. Separately, we characterize water availability by hydrologic region using summary statistics from the California Department of Water Resources (*California Department of Water Resources*, 2021) and USBR and DWR summaries of surface-water deliveries by water year (*Lund et al.*, 2018). Though periodic groundwater level measurements from DWR are temporally sparse, we qualitatively compare relative changes in hydraulic head to seasonal surface displacements. Lastly, we infer the role of surface runoff (occurring as streamflow) in our estimated seasonal uplift timing using area-normalized runoff data from USGS WaterWatch portal (*U. S. Geological Survey*, 2019). The runoff information helps constrain our interpretation of the observed deformation in the SJV.

3.3 Results

3.3.1 Vertical Displacement Rates

The estimated vertical displacement rates (v in equation 3.1) between April 2015 and October 2017 are dominated by two areas of high subsidence ($\geq$ 100 mm/yr) inside the alluvial boundary of the SJV (V_t1 and V_t2 in Figure 3.S4). These subsidence regions are well documented and geographically consistent with recent studies (*Farr*, 2018; *Murray and Lohman*, 2018; *Ojha et al.*, 2019). We observe a maximum subsidence rate of $\sim$270 mm/yr within V_t2, similar to the 250 mm/yr maximum subsidence rate reported by (*Ojha et al.*, 2019) for January 2015 to April 2017. Much higher subsidence rates were reported by (*Farr*, 2018) ($\sim$400 mm/yr; May 2015 through May 2017) and (*Murray and Lohman*, 2018) ($\sim$550 mm/yr; November 2014 through September 2017). The observational time window and methodologies for estimating the vertical motion from LOS play large roles in the differences between these reported rates. Further, we show in a recent study (*Neely et al.*, 2020) that interferogram referencing methodologies can influence peak deformation rates, which may account for some portion of these observed differences.

Importantly, subsidence rates in the SJV change throughout the year in response to water demand (*Levy et al.*, 2020). All four of these rate estimates include data across dry and wet years. Because of this interannual variability, and to assess displacement responses to hydrological endmembers (Figure 3.2), we partition our data into water years and separately analyze the dry (WY2016; 1 October 2015 to 30 September 2016)

and wet (WY2017; 1 October 2016 to 30 September 2017) water years. While the absolute magnitude of surface displacements can be related to groundwater changes, for this study we focus on comparing relative displacement changes between dry and wet years.

WY2016 (regulatory "dry" year)

In WY2016, California received 104% of average precipitation, had an estimated 90% of average snowpack, and experienced 97% of average river runoff (*California Department of Water Resources*, 2021), it also had minimal surface-water deliveries (0-5% of requested) from the state and federal water projects and was preceded by 4 years of extreme drought (*Lund et al.*, 2018). Thus, we characterize WY2016 as a regulatory "dry" year. High-subsidence regions in WY2016 (V_d1-2 in Figure 3.2) occur in the same locations as those in our multiyear estimate (Figure 3.S4), but WY2016 subsidence rates are greater, with the maximum exceeding 345 mm/yr. Inside the alluvial boundary of the SJV, the surface subsided at an average rate of 42.0 mm/yr (Table 3.1). Some uplift is observed north of V_d1 though this is likely due to residual unwrapping errors not corrected by our GPS correction (*Xu et al.*, 2017). Outside of the SJV alluvial boundary, the average rate of displacement was near zero. There is some modest uplift (as much as 20 mm/yr) in the adjacent mountain ranges (Figure 3.S4), which has also been observed using campaign and permanent GPS. It is attributed to the solid earth elastic rebound from loss of groundwater and surface water incurred during the 2012-2016 drought (*Borsa et al.*, 2014; *Fu et al.*, 2015; *Argus et al.*, 2017; *Adusumilli et al.*, 2019).

WY2017 ("wet" year)

In the wet WY2017, average precipitation within California was ∼164% of average, mountain snowpack was ∼163% of average, statewide river runoff was ∼217% of average (*California Department of Water Resources*, 2021), and 85-100% surface-water delivery requests were met (*Lund et al.*, 2018). While the regions of greatest subsidence in WY2017 (V_w1-2 in Figure 3.2) coincide with those of WY2016, the areal extent of subsidence and its peak magnitude are sharply reduced in the wet year. The peak subsidence rate in WY2017 is 177 mm/yr and occurs ∼25 km northeastward of the peak subsidence location in WY2016. The average vertical displacement rate inside the alluvial boundary of the SJV was -20.4 mm/yr, which was less than half the subsidence rate in WY2016. The most striking feature in the wet year displacement rate was the substantial uplift (up to 100 mm/yr; mean value of 26.4 mm/yr) across the Westlands Water District (magenta outline in Figure 3.2). In addition to this large area of uplift, we observe several localized uplift features in the southern SJV (V_w3 in Figure 3.2).

In summary, a comparison of vertical displacement rates between the dry WY2016 and the wet WY2017 shows that even with substantial increases in precipitation, runoff, and surface-water allocations in WY2017, subsidence persisted in the two regions of greatest subsidence in WY2016. These locations feature an abundance of underlying clay and silt layers that are highly susceptible to compaction (*Williamson et al.*, 1989; *Faunt*, 2009). Conversely, in regions with coarser-grained deposits, such as the glacial fluvial fans underlying Fresno (*Weissmann et al.*, 2005; *Faunt et al.*, 2016), observed

land subsidence is comparably subdued.

3.3.2 Amplitude of Seasonal Surface Deformation

Seasonal amplitudes (A in equation 3.1) of the vertical displacement time series are an indicator of change in groundwater storage within each water year. Our underlying assumption is that seasonal surface deformation within the alluvial boundary of the SJV is dominated by poroelastic deformation of the aquifer system, which is driven by cyclical changes in groundwater storage (*Murray and Lohman*, 2018). Small seasonal amplitude values typically indicate that groundwater storage changes are non-cyclic on an annual period. Examples include, but not limited to, regions with multiple intervals of groundwater extraction throughout the year or negligible seasonal groundwater recharge. Large seasonal amplitudes are consistent with significant seasonal groundwater recharge and/or highly variable pumping between seasons.

For the purpose of assigning significance to amplitude values, we bin seasonal amplitudes for each water year into three categories: *low* ($A < 10$ mm), *moderate* (10 mm $\leq A <$ 20 mm), and *high* ($A \geq 20$ mm). We note that compared to previous InSAR studies that also examined seasonal amplitude (e.g., (*Colesanti et al.*, 2003) over portions of the Santa Clara Valley and (*Bell et al.*, 2008) over the Las Vegas Valley), our *low* threshold is on the high end of their maximum amplitude of 10 mm.

WY2016 Amplitudes

For the dry WY2016, seasonal amplitudes reach 35 mm, with an average amplitude of 6.7 mm inside the SJV alluvial boundary (Table 3.1) and an average of 4.3 mm outside the boundary. *High*-amplitude regions are exclusively located within the SJV sedimentary basin, accounting for 2.6% of the study area. *Moderate*- and *low*-amplitude regions accounted for 17.2% and 80.2% of the study area, respectively. The spatial pattern of estimated seasonal amplitudes (Figure 3.3a) is similar to that of (*Murray and Lohman*, 2018), although their magnitudes are smaller. *High* seasonal amplitudes are generally coincident with the high subsidence rates in WY2016 (Figure 3.S5a); however, the location of the highest seasonal amplitude value (A_d5) is offset ∼30km to the southeast of the peak subsidence rate.

High- to *moderate*-amplitude areas are typically located along the course of rivers (perennial or ephemeral) originating in the Sierra Nevada to the east or the Coast Ranges to the west (Figure 3.3a). On the eastern side of the SJV, these areas are associated with (from south to north) Caliente Creek and other ephemeral streams from the Tehachapi Mountains, Deer Creek and the Tule River, the Kaweah River, and the termini of several smaller outflows (Fresno River, Chowchilla River, and Mariposa Creek) (Figure 3.1). On the western side of the SJV, the zone of *high* seasonal amplitude is located north of former Tulare Lake and southwest of the Fresno Slough, adjacent to the Los Gatos Creek. Not all rivers are associated with areas of *high*-amplitude seasonal displacements: most notably the Kern, Kings, and San Joaquin Rivers. These perennial rivers are host

to the three largest reservoirs in the southern Sierra Nevada (Isabella, Pine Flat, and Millerton) and heavily managed to support SJV irrigation in both wet and dry years. As a result, we expect groundwater recharge along these rivers to occur more continuously throughout the year, which would act to dampen or eliminate the seasonal signal.

WY2017 Amplitudes

Similar to WY2016, WY2017 also exhibits seasonal amplitudes of up to 35 mm, with the *high*-amplitude areas located exclusively within the alluvial boundary and adjacent to rivers and creeks primarily sourced in the Sierra Nevada (Figure 3.3b). *High*-, *moderate*-, and *low*-amplitude pixels account for 2.6%, 16.8%, and 80.6% of the study area within the SJV, respectively (Table 3.1). We observed average amplitudes of 7.1 mm and 6.6 mm inside and outside of the SJV, respectively. We identified six regions of *high* seasonal amplitude; the largest magnitude (A_w3) is located at the terminus of the Tule River, bordering the boundary of the former Tulare Lake. Spanning 10s of km, A_w3 is located just west of WY2017 peak subsidence and east of the uplift of the Westlands Water District, where we observe relatively little secular deformation (Figure 3.S5b). In contrast to WY2016, many of the *high* to *moderate* seasonal amplitude regions (e.g., A_w1, A_w3-6) are not coincident with strong subsidence rates (Figure 3.S5b).

Comparing the dry and wet years, we observed an increase in mean seasonal amplitude from 5.0 mm (WY2016, dry) to 6.7 mm (WY2017, wet) across the entire study area. Within the SJV itself, seasonal amplitude statistics are similar for both water years (Table 3.1), although there are differences in the spatial patterns of sea-

sonal amplitudes and associated uncertainties (Figure 3.S6). Specifically, in WY2017 we observe reductions in amplitude along the Kaweah River, Tule River, Deer Creek, and intervening regions relative to WY2016. Conversely, we observe an increase in seasonal amplitude near the former Tulare Lake in WY2017 at the confluence of these watercourses. Interestingly, the entire Westlands Water District exhibited *moderate* to *high* seasonal amplitude during the dry year but only the southeast portion of this region experienced appreciable seasonality during the wet year. However, for all the changes in the spatial pattern, more than half of the local maxima in amplitude are common to both years (A_d1-2 to A_w1-2 and A_d4-6 to A_w4-6) despite differences in surface-water availability.

3.3.3 Timing (Phase) of Seasonal Surface Deformation

In addition to amplitude, the sinusoidal term in our model provides the temporal phase shift (T in equation 3.1) associated with seasonal surface displacements. In the SJV, these surface displacements are controlled by the pore-pressure response to changes in hydraulic head (*Poland and Davis*, 1969). We interpret peak subsidence to correspond to annual minima in local groundwater storage and peak uplift to correspond to annual maxima in local groundwater storage (*Leake*, 1990). In this study, we focus on groundwater storage maxima and use phase timing to estimate when the maximum seasonal uplift occurs for each interferometric pixel. We map the peak seasonal uplift in terms of time of year across the SJV (Figure 3.4) to investigate spatiotemporal patterns in seasonal groundwater storage. While we highlight higher confidence pixels ($\sigma \leq 31$

days) in Figures 3.4-3.5, we consider all pixels in our analysis because of the observed spatial coherence in timing.

WY2016 Peak Seasonal Uplift Timing

During WY2016, we observe spatially continuous patterns of uplift timing in the SJV that indicate migration of annual groundwater storage peaks across the valley. In Figure 3.4a, we identify uplift originating in January (pink) to early March (red) along the San Joaquin River (P_d2), the Kaweah River (P_d4), the southern end of the Friant-Kern Canal (P_d8), the northern section of the agricultural fields south of Bakersfield (P_d6), and adjacent to the California Aqueduct along the western edge of the SJV north of the former Tulare Lake (P_d3). From these locations, peak seasonal uplift radiates outward (e.g., Figure 3.5a), with peak timing extending through July (yellow). Regions with uplift outside of this range (October to December and August to September) occur where there is a) less intense agriculture, b) coarse-grained glaciated fluvial fan deposits (e.g., near Fresno), and/or c) within the former Tulare Lake bed. As a whole, we observe a somewhat trimodal distribution of uplift timing across the SJV, with peaks around April, late July, and, to a lesser extent, late October with the mode of peak uplift occurring in late March (Figure 3.6).

WY2017 Peak Seasonal Uplift Timing

In WY2017, spatially continuous patterns of uplift timing are also observed, yet differ from those described for WY2016. We observe fewer locations of winter (January

to early March) peaks in uplift during the wet year than in the dry year (Figure 3.4). However, these regions are typically common to those in WY2016 and include P_w2 along the San Joaquin River (compare to P_d2 although with higher uncertainty), P_w4 along the Kaweah River (compare to P_d4), and P_w6 in the agricultural fields south of Bakersfield (compare to P_d6). In some cases, these peaks visually correspond to regions with high seasonal amplitudes (Figure 3.S8b). An exception being the most notable high amplitude feature, A_w3, which coincides with a summer uplift (August) and is concurrent with the final stages of the river runoff sequence (Figure 3.6). Radiating outward and typically downslope from these winter uplift maxima, peak seasonal uplift in WY2017 occurs progressively later into the year towards the interior of the valley, lasting through September (Figures 3.4b and 3.5b). Compared to WY2016, the summer and autumn uplift peaks for the SJV as a whole are delayed by about a month in WY2017 (Figure 3.6). In a year such as WY2017, with elevated precipitation and prolonged associated runoff, we can observe peak seasonal uplift timing patterns that delineate specific surface-water features at great detail (e.g., the Kern River west of Bakersfield; Figure 3.S9).

For both WY2016 and WY2017, we observe winter (January to early March) peak uplift at discrete locations on the eastern side of the valley. These uplift features typically correspond to areas with *high* seasonal amplitudes and are directly adjacent to perennial rivers sourced at high elevations in the Sierra Nevada which nevertheless experience high seasonal variability in flow. However, seasonal displacements in the interior of the SJV during the wet year do not achieve peak seasonal uplift until September (Figure 3.6). This is a stark difference with the dry year, where a majority of the valley experiences

peak uplift in early spring (April) or mid-summer (July).

3.3.4 Phase Progression vs. Surface-Water Flow

As detailed above (Section 3.3.3), we assume that the time of peak uplift at any given location indicates the time of maximum local groundwater storage. With this interpretation, we postulate that the spatial gradient peak seasonal uplift can indicate either the timing of maximum local vertical infiltration of surface water into the aquifer, the lateral flow of groundwater in response to recharge and/or redistribution resulting from changes in hydraulic gradients, or a combination of the two processes. We examine the horizontal progression of peak uplift for each year and compare it with the direction of uninterrupted surface-water flow derived from topography in order to assess these potential mechanisms for generating observed uplift timing patterns.

Using the unit-normalized ∇P_{topo} (Section 3.2.5), the azimuthal distribution and spatial patterns of surface-water flow derived from topography indicate a bimodal distribution of flow in the SJV (Figure 3.7a), consistent with water entering the valley from the northeast near the Sierra Nevada and from the southwest near the Coast Ranges. Surface-water flow patterns show convergence at topographic lows (rivers and streams) and divergence at topographic highs (coincident with watershed boundaries). These surface flow directions provide context for the lateral migration of peak seasonal uplift over our study period. That is, a difference between the direction of uplift progression and the topographic gradient suggests that the patterns of uplift timing are not controlled by surface-water drainage according to elevation. Conversely, where the direction of uplift

progression aligns with the topographic gradient, either vertical infiltration of surface water (moving downstream over time as the aquifer fills) or the downslope migration of groundwater can be at work.

We find that the azimuthal directions of uplift migration in both the dry and wet water years (Figure 3.7b,c) are more uniformly distributed than the pattern of surface runoff, but are still preferentially oriented along the northeast-southwest axis observed in the pattern of the topographic gradient (Figure 3.7a). While the seasonal uplift timing is broadly different between WY2016 and WY2017, the direction of the progression near noted regions of winter uplift is fairly consistent for both years (Figure 3.S10). For example, the region focused on P_d4 in WY2016 has peak uplift timing ranging from January to June (Figure 3.5a), whereas in WY2017 (P_w4), the phase timing spans January to August (Figure 3.5b). However, despite this difference in uplift timing, the horizontal direction of uplift progression in both water years is similar (Figures 3.5a,b and 3.7e,f).

3.4 Discussion

3.4.1 Implications for Groundwater Recharge and Flow within the SJV

In the SJV, vertical surface displacements are often attributable to changes in hydraulic head (*Smith et al.*, 2017). A decomposition of these displacement time series

into annual rates and seasonal oscillations offers unique insight into the spatiotemporal variability of groundwater resources in this region. While displacement trends can inform us of groundwater sustainability and the relative balance of groundwater recharge and extraction, the seasonal amplitudes and timing of surface displacements are suggestive of how groundwater moves through the aquifer system. Comparison of deformation observed in the SJV between dry and wet water years further illustrates the complexities and dynamic behavior of groundwater flow on short time scales. However, surface displacements can be interpreted in several ways. For example, a displacement time series reflecting only seasonal drawdowns from pumping (or conversely reflecting only seasonal recharge) separated by periods of no change may yield a similar amplitude to that from a displacement time series consisting of both seasonal pumping and recharge (*Bell et al.*, 2008). Further, pumping and recharge can alter hydraulic head gradients on seasonal time scales, which can change the direction of groundwater flow (*Fetter*, 2018). Here, we use "recharge" to denote local groundwater storage increases in the aquifer system that result from either or both external sources (e.g., infiltration of water from the land surface to the aquifer system) and internal sources (e.g., redistribution of groundwater within the aquifer system to areas impacted by groundwater extraction).

Seasonal surface displacements are best understood in the context of local and regional hydrology. Conceptually, low seasonal amplitude values during a dry year suggests the region was subjected to either negligible groundwater extraction or that the extraction is non-cyclic on an annual period. Conversely, high amplitude values in a dry year most likely result from strong seasonal groundwater extraction. Low ampli-

tude values in a wet year, similar to a dry year, suggests that there was either negligible groundwater extraction/recharge or that any extraction/recharge is non-cyclic on an annual period. High amplitude values in a wet year indicate strong seasonal groundwater extraction and/or seasonal recharge. This includes the case where there is both strong seasonal and nonseasonal groundwater extraction and/or recharge. Thus, the inclusion of *in-situ* data and ancillary information is needed to constrain possible interpretations of the amplitude variations.

WY2016 was a regulatory dry year, having a total uninterrupted runoff from the Sierra Nevada into the Tulare Lake Region (TLR) of the SJV of ∼2.4 km^3 (65% of average), with peak runoff in May (∼0.6 km^3) and below-average river flow for all months (*California Department of Water Resources*, 2021). Further, water deliveries from regional, state, and federal water projects were minimal (0-5% of requested for agricultural contractors south of the Sacramento-San Joaquin Delta) (*Lund et al.*, 2018). In general, a reduction in available surface water often leads to an increased reliance on groundwater in order to meet the water demand of agricultural production (*Hanson et al.*, 2012; *Howitt et al.*, 2015). The increased pumping in WY2016, and in the preceding drought years, reduced pore-pressure in the aquifer system and subsequently induced high subsidence rates across the SJV (e.g., Murray & Lohman, 2018; Ojha et al., 2019; Figure 3.2a). WY2016 vertical land surface displacements also exhibited strong seasonal amplitudes (∼35 mm; Figure 3.3a), despite the minimal surface water available for natural or artificial recharge. One interpretation is that seasonal groundwater pumping was a dominant driver of observed seasonal displacements, consistent with results from previ-

ous studies (*Chaussard and Farr*, 2019). Groundwater-level observations show increases that are coincident with the timing of uplift (Figure 3.5c). These relative increases may be the result of a comparatively rapid pressure response related to groundwater pumping operations, a slower lateral redistribution of water within the aquifer system due to changes in hydraulic head gradients, or a combination of the two.

In contrast to WY2016, WY2017 was an exceptionally wet year. The SJV experienced above average precipitation (∼171% of average in the TLR) and river runoff into the TLR exceeded 8.9 km^3 (∼223% of average; peak runoff in June with ∼1.8 km^3) with above-average river flow from January to September. Contractual surface-water deliveries from the State Water Project and the Central Valley Project were 85-100% fulfilled statewide (*Lund et al.*, 2018). Even when surface water is broadly available, groundwater is often still extracted to meet agricultural demand late in the growing season or in regions with minimal access to surface-water supplies (*Faunt et al.*, 2016). Relative to WY2016, subsidence in WY2017 was greatly diminished, with only a few regions of high (>100 mm/yr) subsidence persisting across both years (Figure 3.2). Part of this wet year subsidence may be explained by delayed groundwater drainage from relatively thick fine-grained (e.g., clays and silts) sedimentary units (aquitards or interbeds) in the aquifer system (*Smith et al.*, 2017; *Ojha et al.*, 2019). Although large precipitation and runoff events occurred within several months of the start of WY2017, compaction of clay layers at depth (due to the previous period of low hydraulic heads) likely continued until the surface-water influx (recharge) started raising water levels in deeper aquifers. While the deeper confined aquifer is typically conceptualized as distinct from the shal-

low "semi-confined" aquifer, groundwater wells that are perforated in both aquifers can increase the exchange of groundwater between the aquifers through intraborehole flow, promoting recharge to the deeper confined aquifer (*Faunt*, 2009).

Some displacement patterns can be related to specific water management districts, underscoring this dataset's utility for informing groundwater policy. Strikingly, the Westlands Water District exhibits elevated uplift rates in WY2017 (as much as 100 mm/yr with a mean value of 26.4 mm/yr and standard deviation of 29.5 mm/yr; Figure 3.2b). Historically, this region has experienced periods of uplift, with as much as 61 mm of apparent rebound observed in 1975 (*Ireland et al.*, 1984). Available extensometer data, which measures compaction or expansion of the subsurface material over a specific depth interval, revealed ∼40 mm of expansion (from the near land surface to ∼307 m depth) in this region during WY2017 indicating that some of the observed uplift can be attributed to recharge and/or regional redistribution of groundwater in the deeper aquifer system. The remaining uplift maybe explained by additional expansion below the depth of the extensometer, a swelling of clays at the surface, or the result of a perched water table from water pooling near the surface due to poor natural drainage (*San Joaquin Valley Drainage Program*, 1990). Finally, the heterogeneity of the aquifer system material may result in a combination of poor drainage and local recharge that explains the pronounced but spatially localized uplift observed at several locations across the valley (V_w3; Figure 3.2b).

WY2017 also exhibited significant seasonal amplitudes (as much as ∼35 mm; Figure 3.3b). The largest amplitude area (A_w3) is associated with summer uplift and

occurs near the confluence of the Kaweah and Tule Rivers (Figure 3.S5b). This feature is absent in the dry WY2016, but there are higher amplitude-value regions farther upstream not observed in WY2017 (compare A_w3 with A_d3). In a wet year with increased water deliveries and elevated uninterrupted streamflow, runoff originating in the Sierra Nevada commingled with canal water imports may travel the lengths of these rivers and directly recharge the central region of the SJV near the former Tulare Lake in much higher volumes than is possible in dry years. The change in uplift timing between the dry and wet years near the terminus of the Kern River (Figure 3.S9) may support this hypothesis, although we note that this is a region with relatively large timing uncertainties. In WY2016, there is no discernible trace of the river in the uplift timing map (Figure 3.S9b). However, in WY2017, there is a clear indication of the river trace and recharge reservoirs defined by winter uplift (Figure 3.S9c). Runoff was relatively low during WY2016, followed by a sharp increase around January 2017 (Figure 3.6; waterwatch.usgs.gov). This general runoff history, taken with our seasonal uplift timing estimates, may indicate when and where water is moving vertically into the aquifer at locations of high sediment porosity and permeability (i.e., likely higher hydraulic conductivity of coarse-grained sediments). Lateral groundwater flow from recharge areas of high hydraulic head near rivers to areas of lower hydraulic head could explain the increases in groundwater level and surface uplift observed in this region. We interpret the timing of seasonal uplift (Figure 3.4) to reveal the spatiotemporal evolution of this flow for a given water year.

As stated previously, there are a number of regions common to both the dry and wet water years that exhibit winter (January to early March) uplift (e.g., P_d2 vs.

P_w2; P_d4 vs P_w4; P_d6 vs P_w6). Taking the feature originating off of the Kaweah River (P_d4 in Figure 3.4a; P_w4 in Figure 3.4b) as an example, we observe that the onset of uplift and the ensuing lateral progression of uplift are consistent between wet and dry years. While the topographic slope trends from the northeast to the southwest in this region, uplift in both years does not simply migrate along this gradient (Figure 3.5a,b), as would be expected if groundwater recharge were initiating along the SJV margin and progressing from high to low elevations through the aquifer under unstressed conditions (*Williamson et al.*, 1989). Instead, we find the progression of surface uplift ranges across all azimuths and often crosses surface watershed boundaries indicated by topographic gradients, which implies that hydraulic head gradients must deviate substantially from uninterrupted surface flow gradients and likely are modulated by groundwater withdrawals (*Williamson et al.*, 1989). While a hypothetical displacement time series resulting from only seasonal groundwater extraction can generate modeled (equation 1) uplift (as the model assumes equal magnitudes for peak subsidence and uplift amplitudes), the relative increase in spring hydraulic head for both dry and wet years (e.g., Figure 3.5c-d) also supports the concept that the modeled uplift is responding to local increases in groundwater storage. Additionally, we do not observe symmetrical phase progression on either side of the Kaweah River. This indicates that the hydraulic head gradients and/or hydraulic conductivity within the aquifer system can vary over spatial scales as short as several kilometers, consistent with a high degree of heterogeneity in the aquifer system.

Attribution of these winter uplift features in WY2017 to recharge from rivers and

streams sourced in the Sierra Nevada is also supported by recent studies of stable isotopes of water. As water vapor travels from the warmer coast towards cooler high elevations of the Sierra Nevada, the heavier isotopes precipitate out first, leaving relatively depleted concentrations of the heavier stable isotopes (for example δ^{18}O in the water molecule) in precipitation that falls farther inland, often referred to as the "continental effect" (*Ingraham and Taylor*, 1991). Water with a relatively lighter isotopic signature (depleted in the heavier isotopes) is then channeled and transported into the SJV by Sierra-sourced rivers. (*Visser et al.*, 2018) found plumes of depleted δ^{18}O concentrations in groundwater samples originating near the Kings, Kaweah, Tule, and Kern rivers (their Figure 4b), emphasizing the role that these rivers play in the recharge of the aquifer system. In fact, all winter uplift features on the eastern side of the valley (e.g., P_w2, P_w4, and P_w6) are associated with lower δ^{18}O concentrations. While we do not observe a similar, distinct winter uplift feature along the Kings River, the region of lowest δ^{18}O content in the (*Visser et al.*, 2018) study, this could be due to the perennial nature of the Kings (i.e., recharge occurring with more regularity rather than just seasonally) and that the coarser-grain material underlying the region is less susceptible to high amplitude deformation related to changes in pore pressure. The agreement between these two independent datasets underscores the potential utility of these new observations of uplift timing and evolution as a tool for understanding groundwater recharge and flow.

3.4.2 Limitations of this study and implications for other aquifer systems

This study investigates the use of surface displacement time series and their seasonal components for identifying and characterizing potential regions of groundwater recharge and flow in the SJV. Our approach can be applied to interferometric time series over other aquifer systems, with the caveat that any such studies consider the simplifying assumptions we have made about the SJV aquifer.

First of all, our analysis does not relate surface displacement to absolute changes in groundwater volumes. Rather, we use surface displacement estimates as a proxy for relative groundwater storage changes, where we assume that displacements are proportional to variations in pore pressure and are governed by the characteristics (e.g., compressibility, thickness, confinement) of the aquifer system. To estimate actual groundwater recharge volumes and/or flow rates would require explicitly characterizing aquifer structure and properties, which we do not do.

Secondly, we assume that the San Joaquin Valley aquifer system is spatially (vertically and horizontally) and temporally homogeneous, even though aquifer heterogeneity has been extensively documented (*Faunt et al.*, 2010). As a result, a given change in groundwater volume may not translate to the same magnitude of surface displacement at different locations in the valley and vice versa. This is why we do not focus on the relative amplitudes of seasonal displacement changes betwen locations, but instead focus on the timing and location of peak uplift, which we interpret in the context of the

spatiotemporal evolution of groundwater flow.

Additionally, while we observe seasonal uplift occurring along river channels where streamflow from the Sierra Nevada provides a potential source of groundwater recharge, there are river-adjacent locations without measurable seasonal surface elevation change. An example is the city of Fresno, which is underlain by a coarse-grained glacial fluvial fan deposit (*Weissmann et al.*, 2005) that would be less compressible than finer grained sediments found elsewhere in the valley. Other notable examples are the large perennial Kings River and San Joaquin River systems, which are extensively managed to provide year-round water flow. These rivers may provide nearly continuous recharge to adjacent aquifers, which would limit seasonal surface deformation.

Further, interpretations may be improved with the inclusion of mass change observations. The use of freely available satellite gravimetry from the Gravity Recovery and Climate Experiment (GRACE) and/or elastic loading estimates derived from GPS have proven effective at determining regional estimates of terrestrial water storage changes (*Famiglietti et al.*, 2011; *Borsa et al.*, 2014; *Argus et al.*, 2017; *Adusumilli et al.*, 2019; *Lau et al.*, 2020). The addition of higher spatial resolution surface displacements from InSAR to these estimates may be helpful for constraining the areal extent of mass change concentrations and in turn help supplement water level observations in data limited regions (*Castellazzi et al.*, 2016). Results from this study further highlight the potential of synergetic use between these datasets.

Lastly, while this study showed success in identifying potential regions of recharge over an aquifer composed of unconsolidated sediments, we might not expect our approach

to be as relevant to karst aquifer systems where deformation related to fluid-pressure changes is strongly dependent on the orientation and size of pre-existing rock fractures (*Serpelloni et al.*, 2018; *Silverii et al.*, 2019).

3.4.3 Groundwater Management

With the passage of the Sustainable Groundwater Management Act (SGMA), the State of California established a framework to protect against the exploitation and degradation of its groundwater resources. Critical to this initiative was the designation of "groundwater sustainability agencies" (GSAs; see Figure 3.7d-f). A GSA is established by a single agency or a combination of local agencies (Water Code §10723.6) and is tasked to develop, implement, and enforce a basin's groundwater sustainability plan in accordance with SGMA (Water Code §10733.4). As such, their boundaries often coincide with existing water management entities, which were typically designed around the availability and flow of surface-water as well as urban development. At agency, regional, and state levels, new or independent data that have the potential to constrain groundwater flow models can lead to an improved understanding of the interconnectedness of the aquifer systems. This would aid monitoring and protection of groundwater resources efforts by informing how existing GSAs can improve their coordination in achieving sustainability goals.

Here, we offer a synoptic view of seasonal surface displacements from InSAR and cGPS over the southern San Joaquin Valley at policy relevant scales. Seasonal displacement amplitude, uplift timing, and lateral progression of timing demonstrate

the complexities of deformation associated with joint surface-water and groundwater hydrological processes in the SJV. Our results highlight where groundwater-driven deformation deviates from natural surface-driven processes. We infer these differences to be preferential pathways for annually averaged groundwater flow. While streams and canals define surface-water networks for GSAs, these inferred pathways suggest potential subsurface interconnectivity (Figure 3.7e,f). Novel information such as this may help identify strategies for GSA coordination that maximize the utility of groundwater resources shared between GSAs. The striking differences in the uplift timing between a dry and wet year display the changing dynamics of the SJV aquifer system under different water availability scenarios at relatively short timescales. Further analysis comparing other water years with a range of hydrological conditions may establish a framework that groundwater managers and users can use to assess and perhaps anticipate the movement and availability of groundwater early in the water year and in time to inform critical planning decisions. These decisions may include, but are not limited to, crop selection, diversions for active conjunctive water use, and monitoring prioritization.

3.5 Conclusions

Leveraging the high spatial resolution of InSAR with the greater accuracy and temporal resolution of cGPS provides detailed insight into regional surface displacements. We estimated the annual rate and seasonal behavior of land surface elevation over the southern SJV for both a regulatory dry (WY2016) and wet (WY2017) water

year using GPS-enhanced InSAR. We find that subsidence in the valley was greatly diminished in WY2017 compared to WY2016, consistent with a reduction in groundwater withdrawals in the presence of increased surface-water availability. Our characterization of the seasonal deformation reveals coherent patterns in amplitude and phase (peak uplift timing) across the SJV. While the peak seasonal amplitude was ∼35 mm for both years, regions of *high* amplitude in WY2017 are typically located near the confluence of rivers and downstream of their WY2016 counterparts. From the seasonal phase, we find that relative uplift generally occurs in the late winter to spring (March to May) for the dry year (WY2016) and during the summer (July to September) for the wet year (WY2017), coincident with waning river runoff volumes. We identified several regions of winter uplift common to both years which are adjacent to rivers with headwaters in the high Sierra Nevada. These regions are consistent with recent isotope studies indicating zones of possible recharge. The progression of this seasonal uplift across the valley often deviates from the topographic gradient, which suggests that the displacement signal is controlled by subsurface processes. Relative maxima in groundwater levels from well measurements (where available) are generally coincident with the timing of peak seasonal uplift, further indicating that we are able to resolve the pore-fluid pressure response from changes in pumping activities and/or a lateral redistribution of water (groundwater flow) in the SJV aquifer system. These analyses and interpretations highlight the complexities of surface deformation related to changes in surface-water availability, groundwater resources, and the conjunctive water use.

Acknowledgements

This work was funded by NASA under Grant NNX16AR07G (Science Team for the NISAR Mission) and Grant 80NSSC18K1422 (NASA Earth and Space Science Fellowship). All raw geodetic and hydrological data are freely available from public sources (as referenced). Processed GPS-enhanced InSAR products are available from the Zenodo repository (DOI: 10.5281/zenodo.3968903). We are grateful to P. Castellazzi, C. Jones, an anonymous reviewer, and D. Galloway who provided thoughtful and constructive feedback which helped improve this manuscript. Further, we thank S. Adusumilli, E. Knappe, D. Kilb, and S. Mumma for their helpful comments during the drafting of this manuscript. Analyses and visualizations were done using GMTSAR (*Sandwell et al.*, 2011; *Xu et al.*, 2017), Generic Mapping Tools (*Wessel et al.*, 2013), and MATLAB. Any use of trade, firm, or product names is for descriptive purposes only and does not imply endorsement by the U.S. Government.

Chapter 3, in full, is a reformatted version of material as it appears in Water Resources Research: Neely, W. R., A. A. Borsa, J. A. Burney, M. C. Levy, F. Silverii, and M. Sneed (2021), Characterization of groundwater recharge and flow in California's San Joaquin Valley from InSAR-observed surface deformation, *Water Resources Research*, 57(4), 1–20, doi:10.1029/2020WR028451. I was the primary investigator and author of this paper.

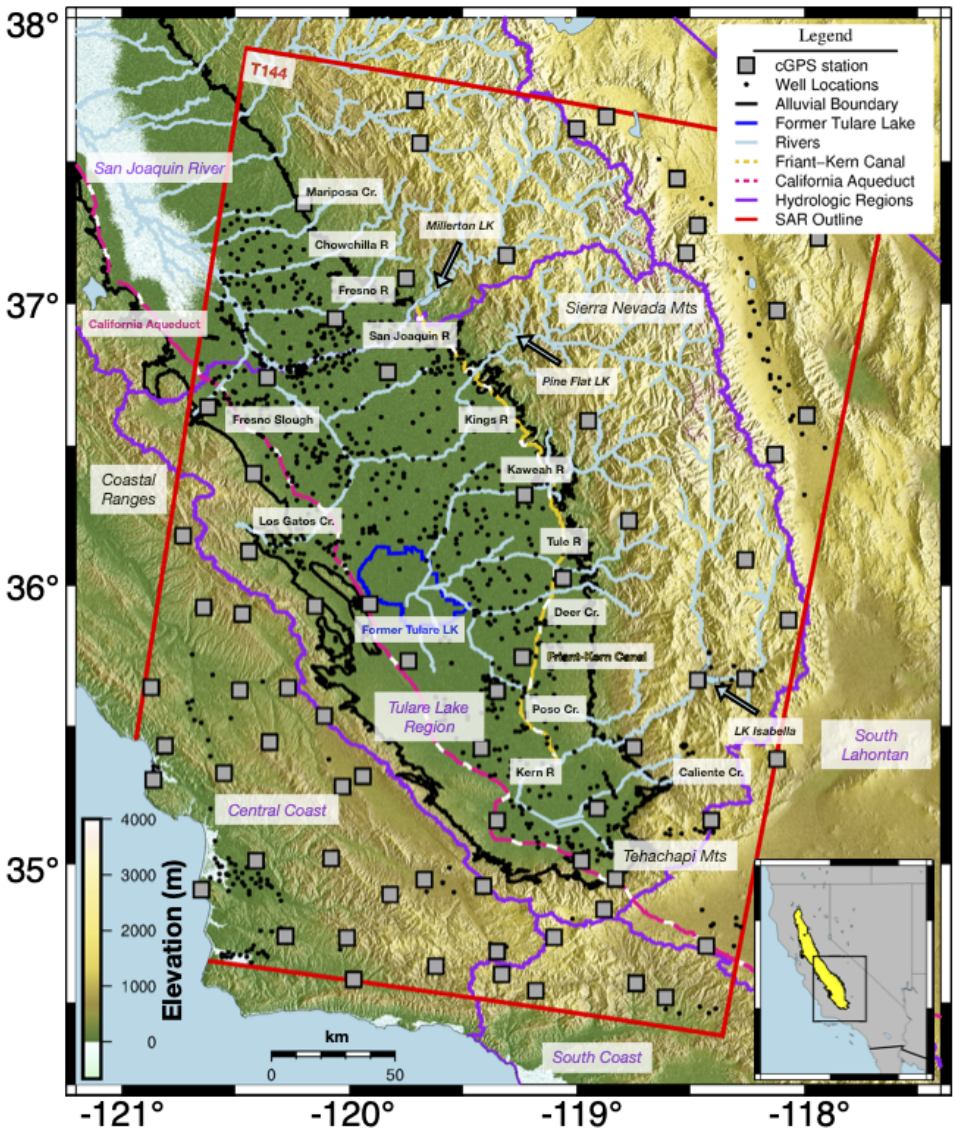

Figure 3.1: Topographic map of study region in the San Joaquin Valley (elevation data from the Satellite Radar Topography Mission). Inset (bottom right) shows the study region over California with the Central Valley (yellow). Synthetic aperture radar (SAR) data used is provided by the Sentinel-1A/B missions, descending track 144 (red outline). A subset of continuous Global Positioning System (cGPS) station locations in the Geodesy Advancing Geosciences and EarthScope (GAGE) network (gray squares) are used to correct and reference each interferogram. We note key hydrological features such as monitoring well locations with data spanning April 2015 to October 2017 (black dots), the alluvial boundary of the valley floor (black outline), the former Tulare Lake (blue outline), rivers entering the valley (light blue lines), the Friant-Kern Canal (dashed yellow line), the California Aqueduct (dashed pink line), and hydrologic regions as designated by the Department of Water Resources (DWR) (purple outlines)

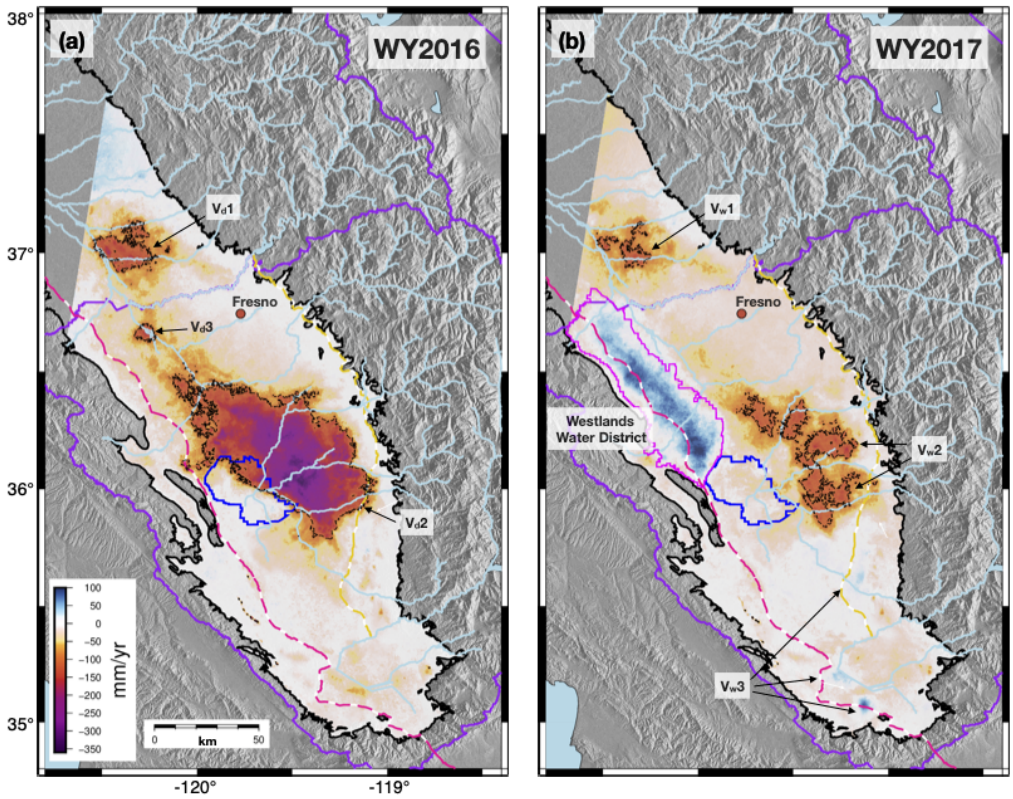

Figure 3.2: Vertical displacement rate maps (mm/yr) over the San Joaquin Valley study region for (a) WY2016 (1 October 2015 to 30 September 2016) and (b) WY2017 (1 October 2016 to 30 September 2017). Regions with vertical displacement rates $\leq$ -100 mm/yr (indicating subsidence greater than or equal to 100 mm/yr; dashed black contour) are labeled V_d1-3, velocity for dry WY2016, and V_w1-2, velocity for wet WY2017. The Westlands Water District (magenta outline) exhibits relatively strong uplift in WY2017. Other smaller regions of uplift in WY2017 are noted as V_w3. The city center of Fresno, CA, is marked by a red-orange circle. We note rivers entering the valley (light blue lines), hydrologic regions (purple outlines), the Tulare Lake (blue outline), the California Aqueduct (dashed pink line), and the Friant-Kern Canal (dashed yellow line).

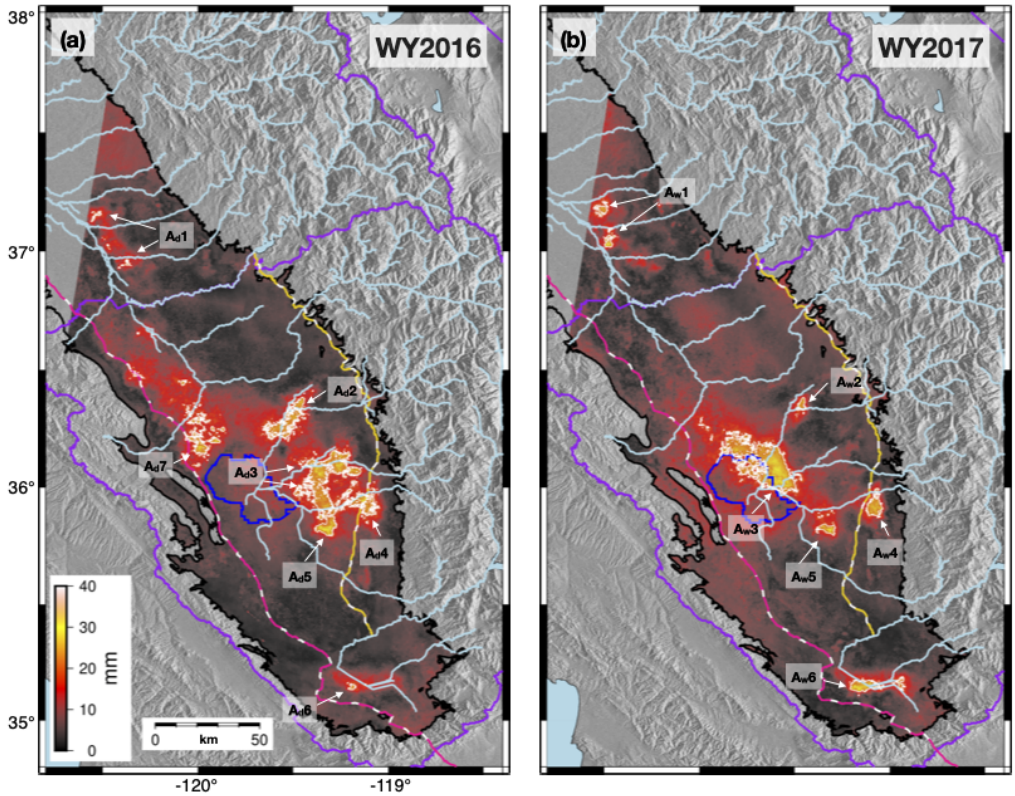

Figure 3.3: Seasonal amplitude maps (mm) over the San Joaquin Valley study region for (a) WY2016 (1 October 2015 to 30 September 2016) and (b) WY2017 (1 October 2016 to 30 September 2017). Regions of *high*-amplitude ($\geq$ 20 mm; white contours) are labeled A_d1-7 (amplitude for dry WY2016), and A_w1-6 (amplitude for wet WY2017). We note rivers entering the valley (light blue lines), hydrologic regions (purple outlines), the Tulare Lake (blue outline), the California Aqueduct (dashed pink line), and the Friant-Kern Canal (dashed yellow line).

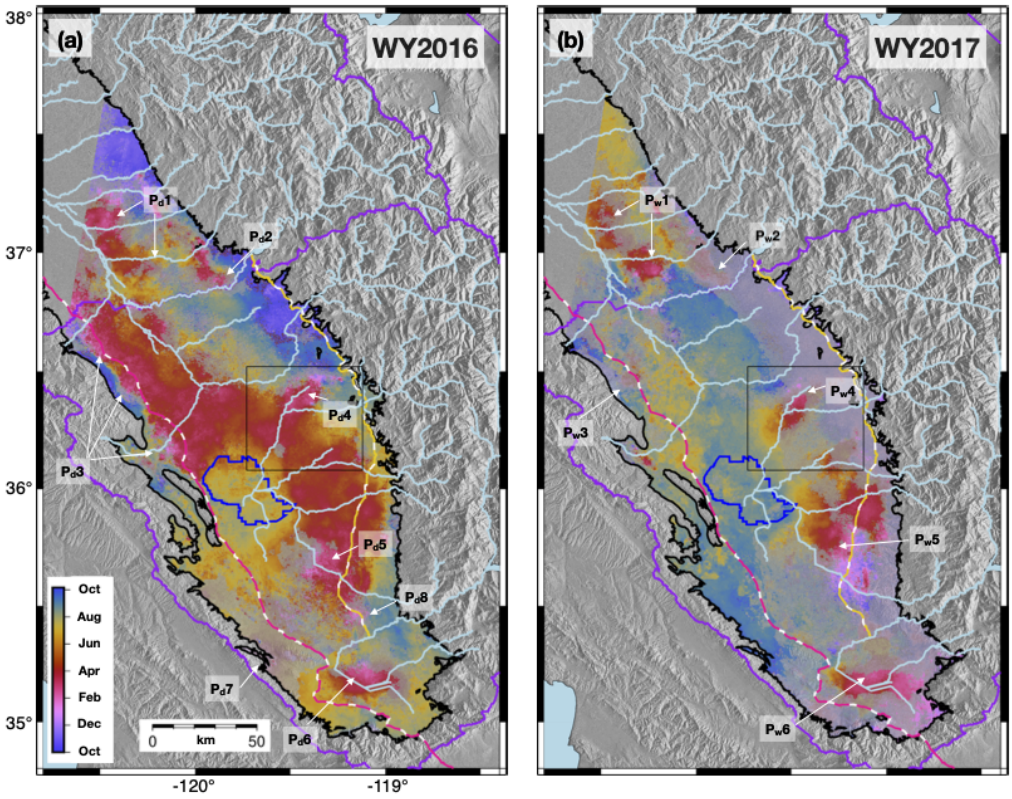

Figure 3.4: Seasonal phase maps (time of year) over the San Joaquin Valley study region for (a) WY2016 (1 October 2015 to 30 September 2016) and (b) WY2017 (1 October 2016 to 30 September 2017). Colors correspond to the timing of peak seasonal uplift in the valley. Regions of interest are labeled P_d1-8, phase for dry WY2016, and P_w1-6, phase for wet WY2016. We note the area around P_d4 and P_w4 shown in Figure 3.5 (black box). We note rivers entering the valley (light blue lines), hydrologic regions (purple outlines), the Tulare Lake (blue outline), the California Aqueduct (dashed pink line), and the Friant-Kern Canal (dashed yellow line).

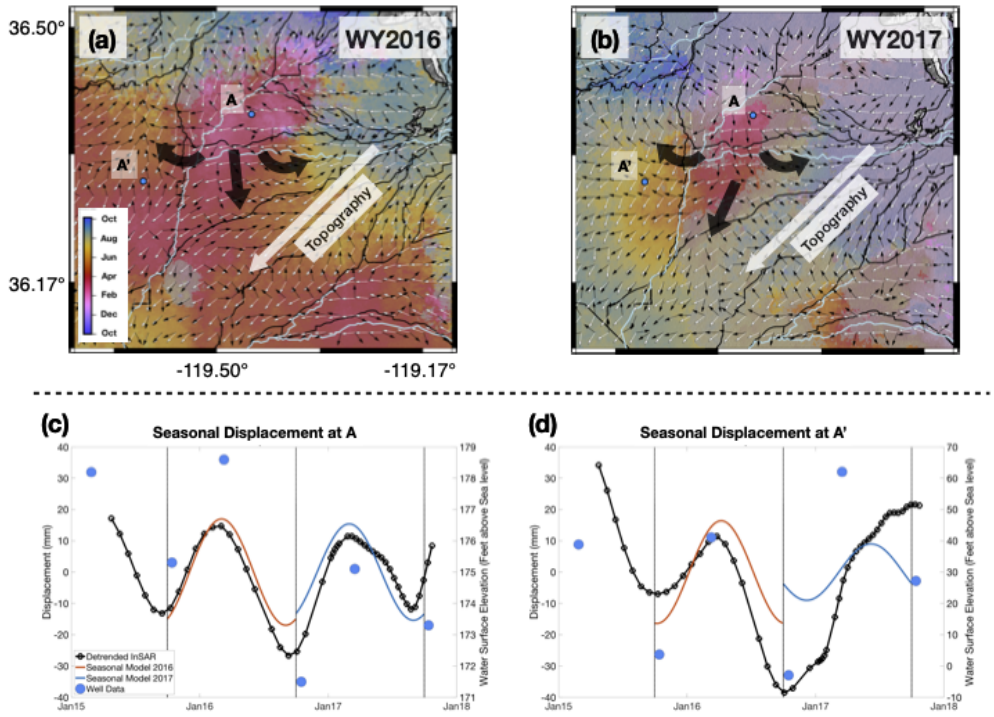

Figure 3.5: Seasonal phase (time of year) for (a) WY2016 and (b) WY2017 around P_d4 and P_w4. The topographic gradient (white arrows) show the direction of implied natural surface-water flow. The gradient of uplift timing (black arrows) indicate direction of phase progression. The general direction of these gradients (larger arrows) are shown in context with watershed boundaries (black outlines). A and A' (blue circles) mark the locations of the seasonal displacement time series shown in (c) and (d) respectively. (c) shows the detrended and modeled seasonal displacement time series (mm) at A along with collocated water surface elevations (feet above sea level; blue circles) from well 327204N1168056W001 (DWR). Similarly, (d) shows the detrended and modeled seasonal displacement time series at A' along with collocated water surface elevations (blue circles) from well 329223N1170659W001 (DWR). Water years (October 1 to September 30) are indicated by vertical dotted lines.

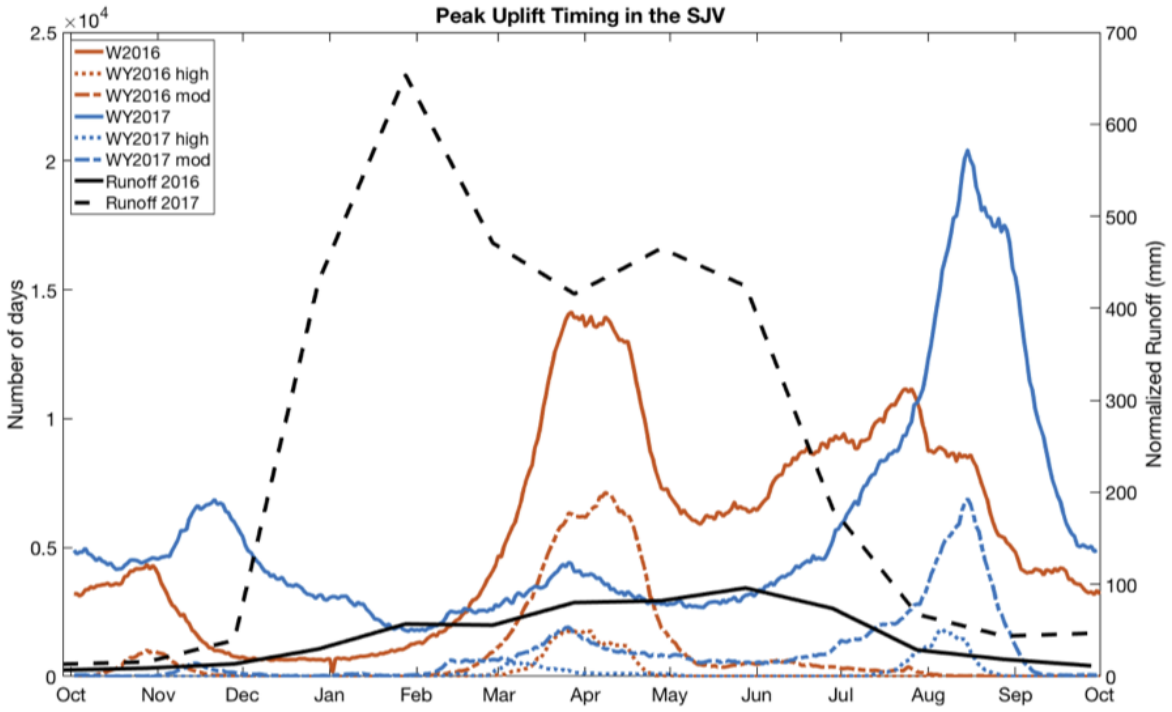

Figure 3.6: Histograms of the peak seasonal uplift timing in the San Joaquin Valley for WY2016 (orange) and WY2017 (blue). Contribution from *moderate* and *high* amplitude value pixels are represented by dotted-dashed and dotted lines, respectively. The monthly area-normalized runoff (waterwatch.usgs.gov) for hydrological unit codes (Figure 3.S11) 18030003, 18030004, 18030005, 18030006, 18030007, 18030009, 18030012, 18040001, and 18040007 are shown for WY2016 (solid black line) and WY2017 (dashed black line).

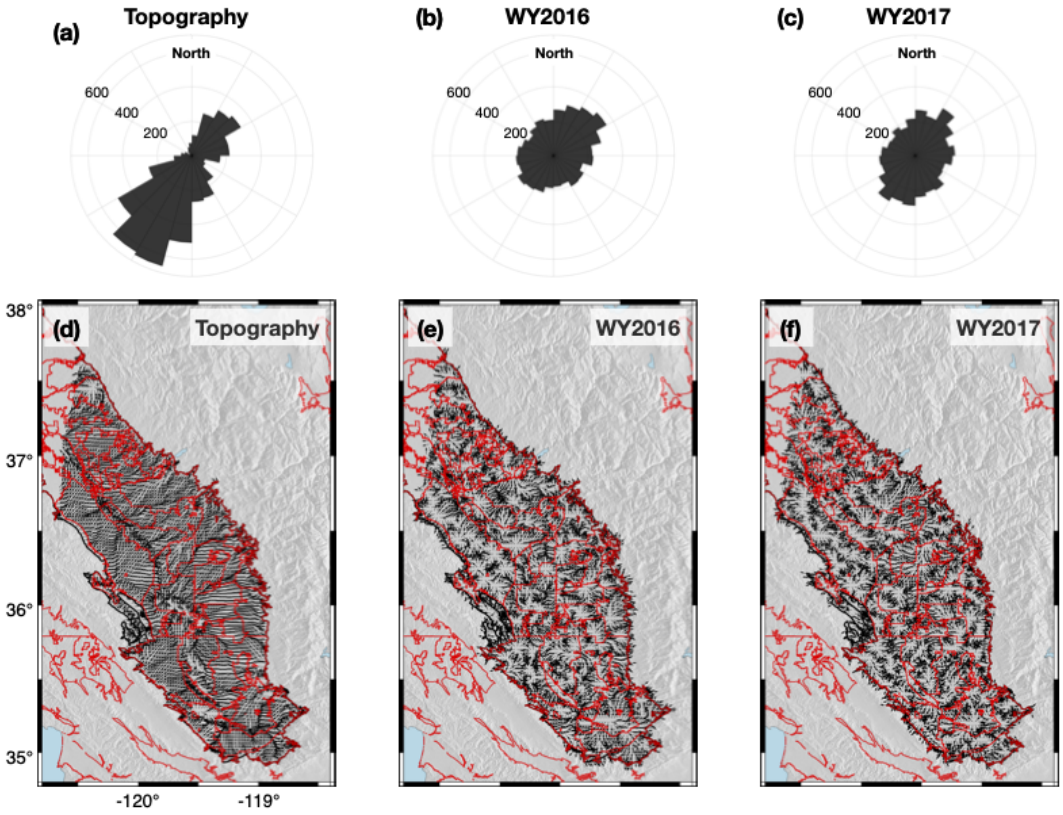

Figure 3.7: Azimuthal distribution of (a) the gradient of topographic slope, (b) the WY2016 phase progression, and (c) the WY2017 phase progression. (d), (e), and (f) show the gradient and phase progression (arrows) for topography, WY2016, and WY2017, respectively, in the context of proposed groundwater sustainability agencies (red outlines).

Table 3.1: Summary Statistics for vertical displacements in the San Joaquin Valley

Time Period	Mean Rate (mm/yr)	Mean Amplitude (mm)	High Amplitude (% of pixels $\geq$ 20 mm)	Moderate Amplitude (% of pixels $\geq$ 10 mm and $<$ 20 mm)	Low Amplitude (% of pixels $<$ 10 mm)
April 2015 to October 2017	-35.3	7.4	5.7	16.3	78.0
WY2016 (October 2015 to September 2016)	-42.0	6.7	2.6	17.2	80.2
WY2017 (October 2016 to September 2017)	-20.4	7.1	2.6	16.8	80.6

3.6 Supplementary Materials

Introduction

This Supplementary Material contains Supplementary Tables 3.S1 through 3.S4 and Supplementary Figures 3.S1 through 3.S11 (with associated captions).

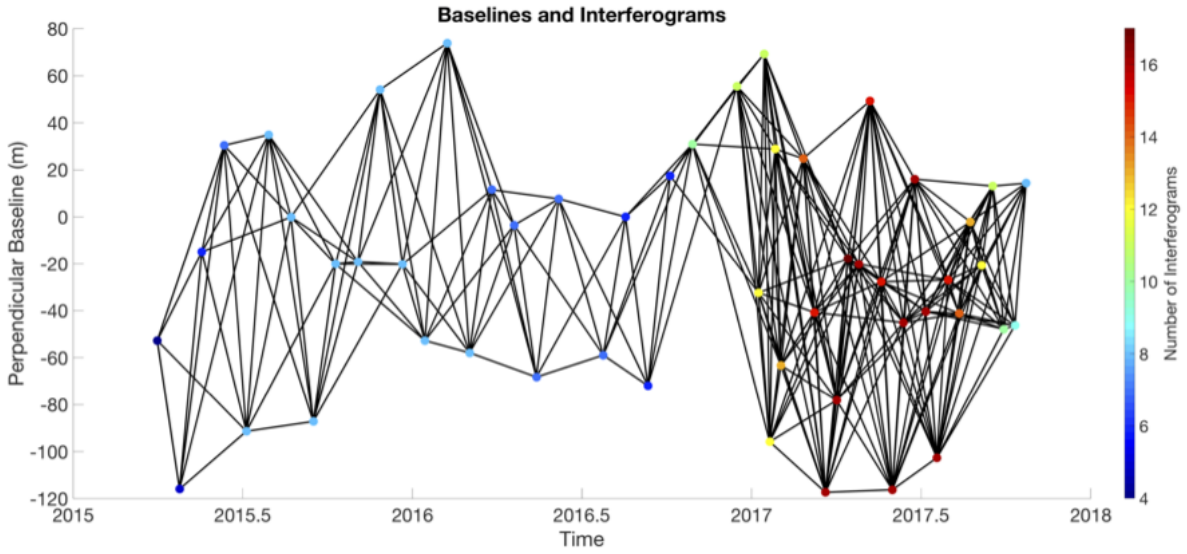

Figure 3.S1: Plot of the perpendicular baseline between synthetic aperture radar (SAR) acquisitions and the number of interferometric pairs each date contributes to. Acquisitions (circle symbols) have a perpendicular baseline relative to the primary reference image (17 August 2016). There are 263 interferometric connections (black lines) with the number of interferograms each scene contributes to (color value of circle symbols) ranging between 4 and 17.

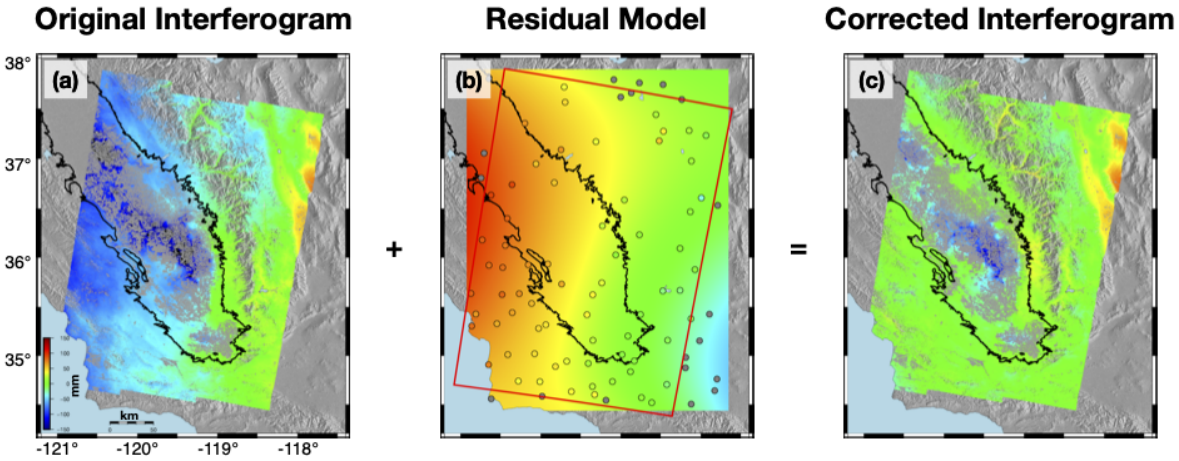

Figure 3.S2: Example of long-wavelength correction for a single interferogram (Sentinel-1, spanning 6 June 2016 to 10 September 2016). Panel (a) is the raw unwrapped interferogram in line-of-sight (LOS). (b) is the residual model constructed by fitting a second/fourth order polynomial to residuals between continuous Global Positioning System (cGPS) displacements and the raw interferometric displacements (scattered circles). (c) is the corrected interferogram which is a summation of (a) and (b).

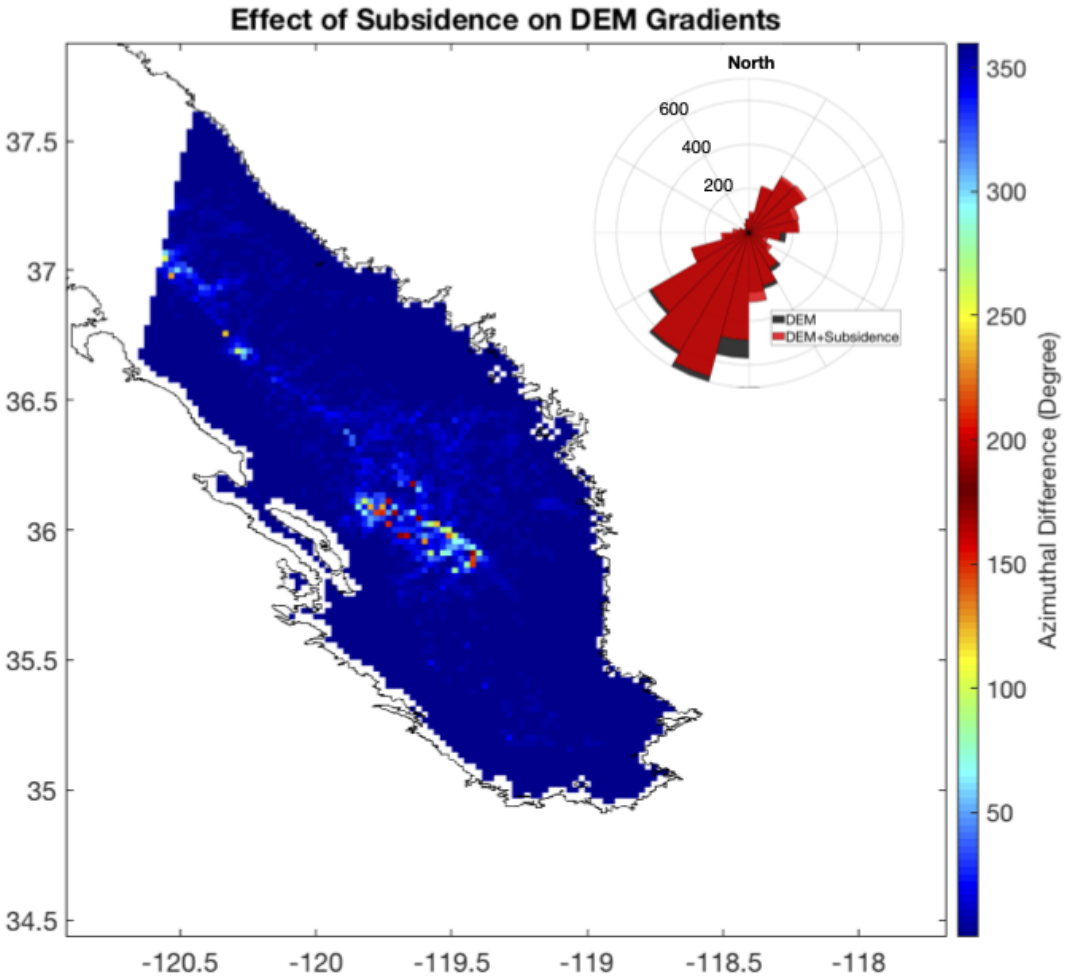

Figure 3.S3: Assessment of land subsidence effects on topographic gradient analysis. Here we generate an extreme subsidence case where 17 years of subsidence (extrapolating displacement rates from WY2016) are superimposed on the original Shuttle Radar Topography Mission (SRTM) Digital Elevation Model (DEM). The histogram in the right-hand corner shows the azimuthal distribution of the gradient for the original DEM (black) and the DEM+subsidence (red) cases. Spatially, the differences are generally confined to the valley axis where there is a change in slope due to sediment sources from the Coast Ranges to the west and the Sierra Nevada to the east.

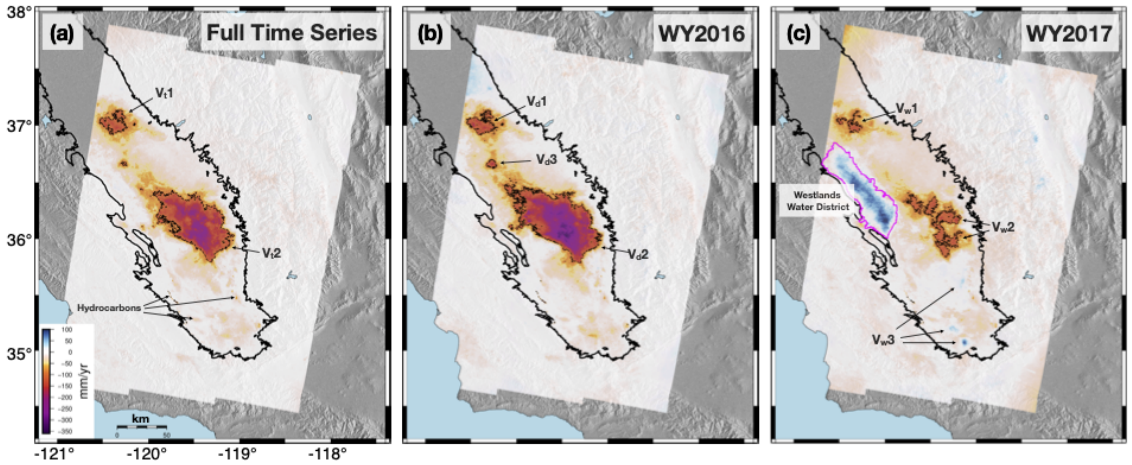

Figure 3.S4: Vertical displacement rate maps (mm/yr) over the southern San Joaquin Valley (black outline) and surrounding environs for (a) the full time series (1 April 2015 to 23 October 2017), (b) WY2016 (1 October 2015 to 30 September 2016) and (c) WY2017 (1 October 2016 to 30 September 2017). Regions with displacement rates $\leq$ -100 mm/yr (indicating subsidence greater than or equal to 100 mm/yr; dashed black contour) are labeled V_t1-2, velocity for the full time series, V_d1-3, velocity for dry WY2016, and V_w1-2, velocity for wet WY2017. The Westlands Water District (magenta outline) exhibits relatively strong uplift in WY2017. Other regions of uplift in WY2017 are noted as V_w3.

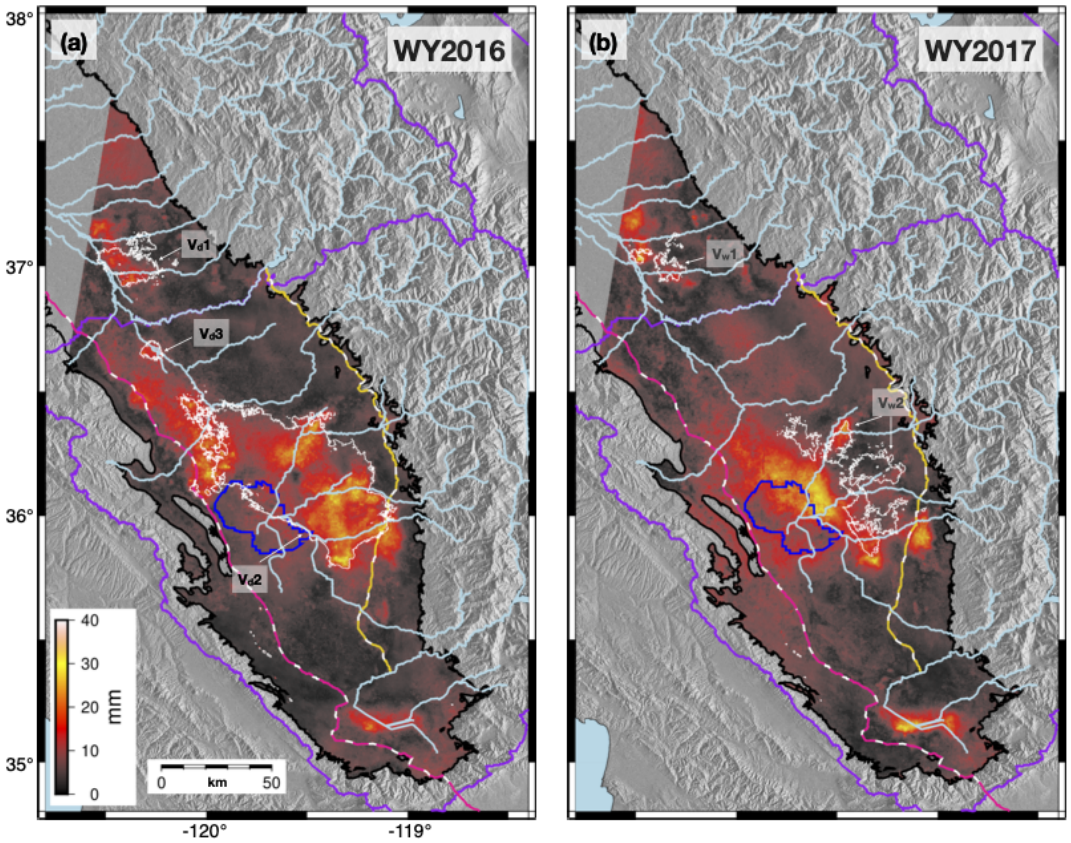

Figure 3.S5: Seasonal amplitude (mm) maps over the southern San Joaquin Valley for (a) WY2016 (1 October 2015 to 30 September 2016) and (b) WY2017 (1 October 2016 to 30 September 2017). Regions with displacement rates $\leq$ -100 mm/yr (indicating subsidence greater than or equal to 100 mm/yr; white contour) are labeled V_d1-3, velocity for dry WY2016, and V_w1-2, velocity for wet WY2017.

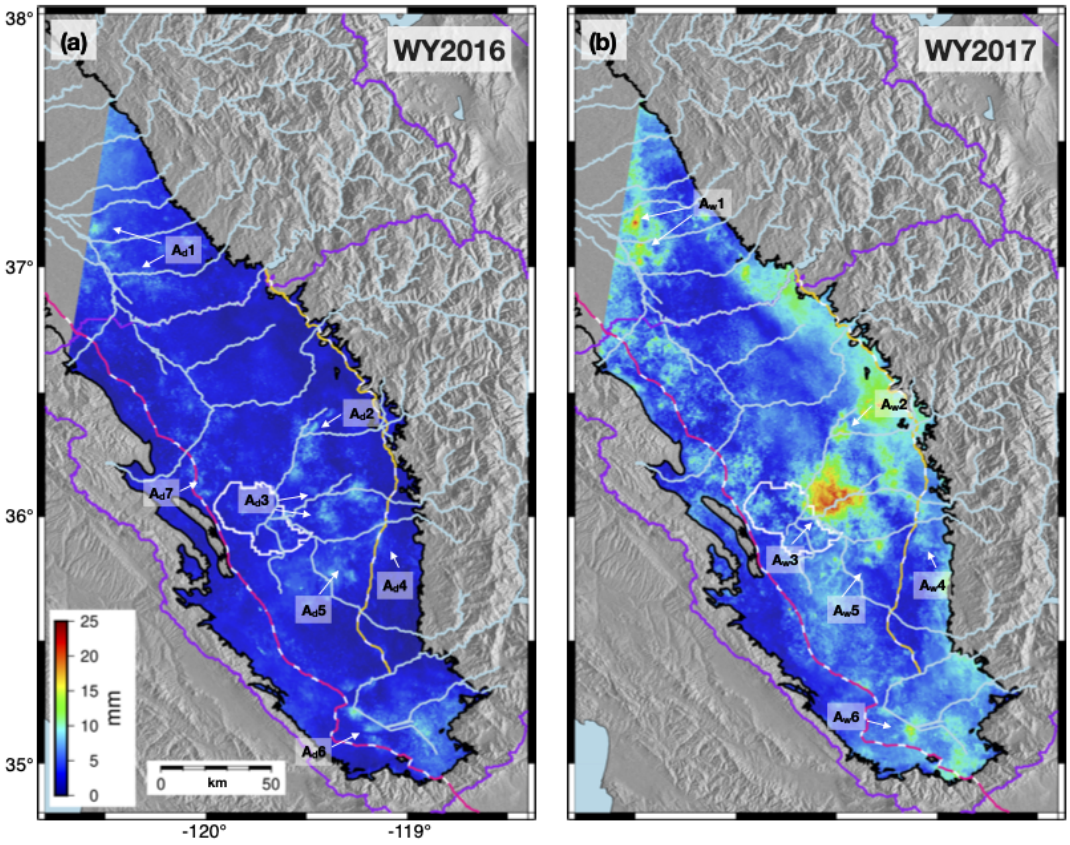

Figure 3.S6: Seasonal amplitude uncertainty (mm) maps over the southern San Joaquin Valley for (a) WY2016 (1 October 2015 to 30 September 2016) and (b) WY2017 (1 October 2016 to 30 September 2017). Values indicate the standard deviation of the amplitude fit. Locations of high seasonal amplitude (from Figure 3.3) are labeled for reference. Other features are consistent with Figure 3.1 with the exception that the former Tulare Lake (now white outline).

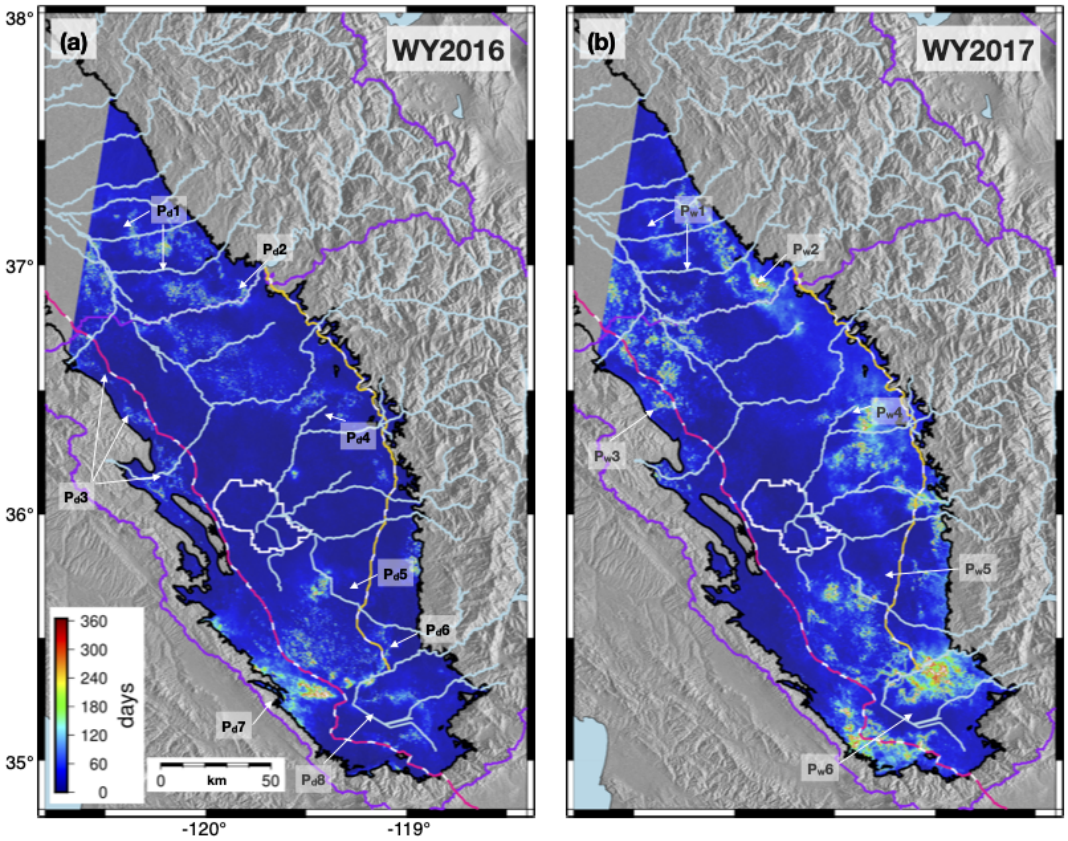

Figure 3.S7: Seasonal phase timing uncertainty (days) maps over the southern San Joaquin Valley for (a) WY2016 (1 October 2015 to 30 September 2016) and (b) WY2017 (1 October 2016 to 30 September 2017). Values indicate the standard deviation of the phase timing fit. Locations of noted seasonal phase (from Figure 3.4) are labeled for reference. Other features are consistent with Figure 3.1 with the exception that the former Tulare Lake (now white outline).

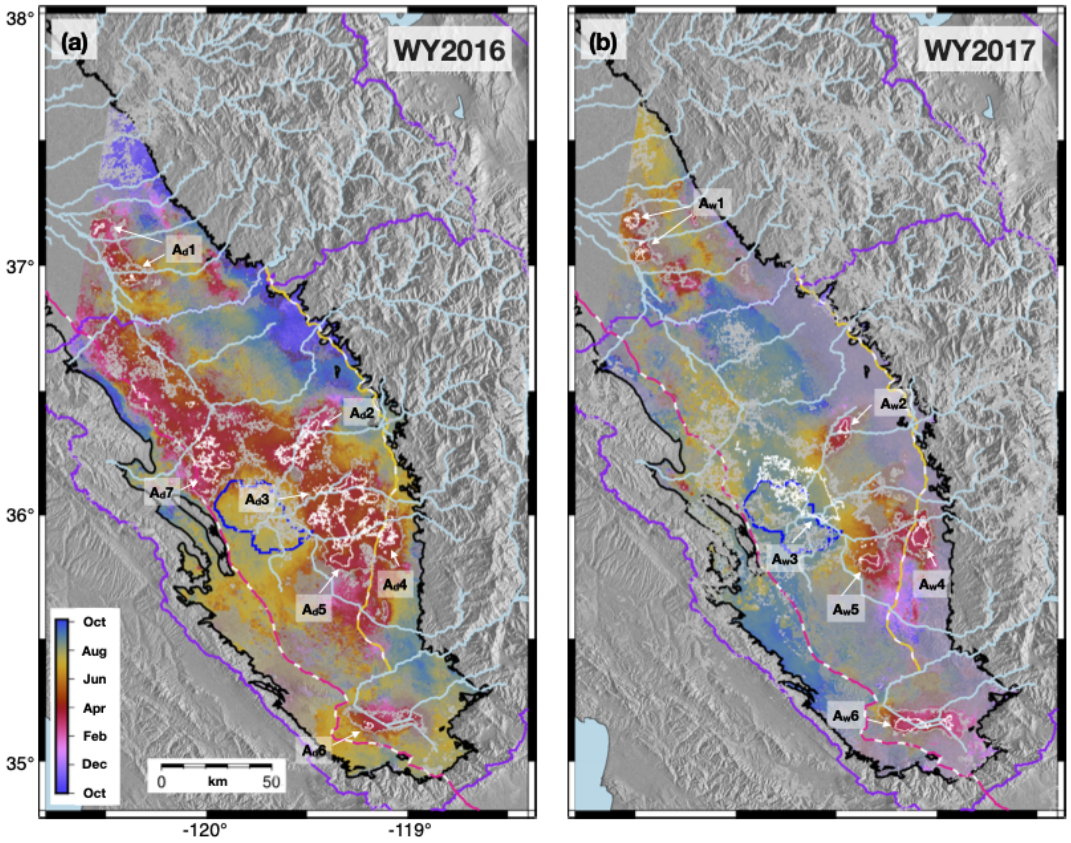

Figure 3.S8: Seasonal phase maps (time of year) over the southern San Joaquin Valley for (a) WY2016 (1 October 2015 to 30 September 2016) and (b) WY2017 (1 October 2016 to 30 September 2017). Regions of *high* amplitude ($\geq$ 20 mm; white contours) are labeled A_d1-8, amplitude for dry WY2016, and A_w1-7, amplitude for wet WY2017. Regions of *moderate* amplitude ($\geq$ 10 mm and $<$ 20 mm; gray contours) surround the regions of *high* amplitude.

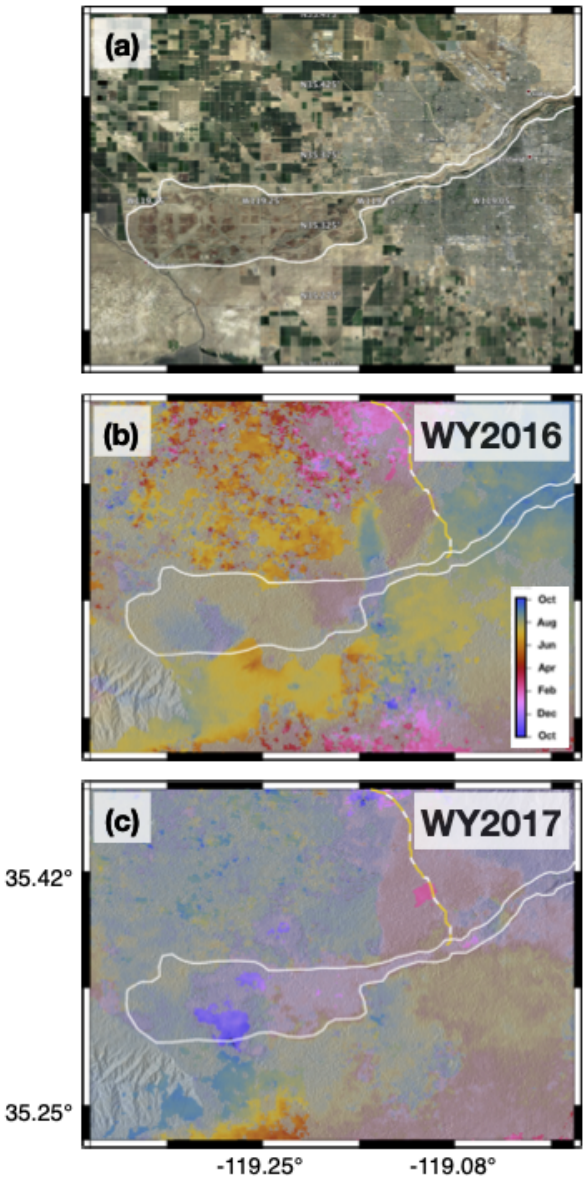

Figure 3.S9: The Kern River between water years. (a) true cover imagery of the Kern River terminus (GoogleEarth; any use of trade, firm, or product names is for descriptive purposes only and does not imply endorsement by the U.S. Government) with the approximate extent of the river (white outline). (b) and (c) show the dry WY2016 and wet WY2017 seasonal phase (peak uplift timing), respectively.

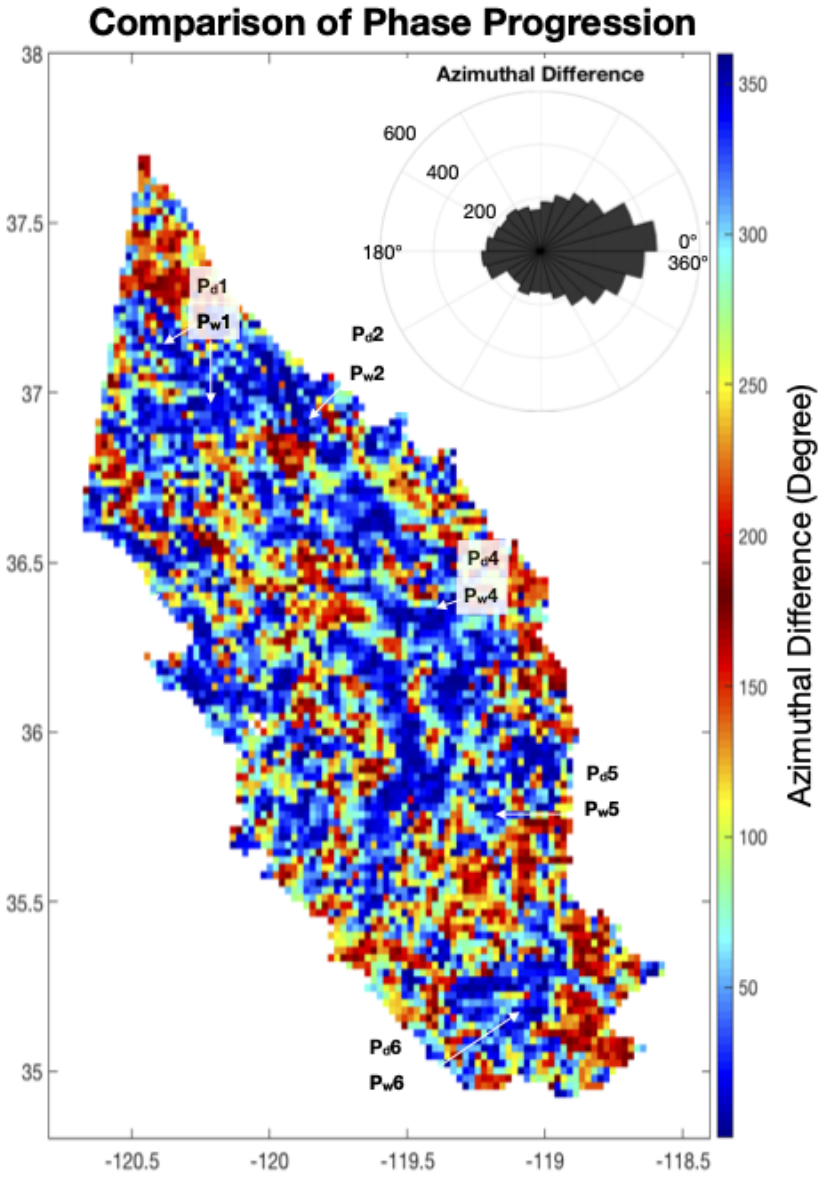

Figure 3.S10: Spatial differences in the phase gradients between WY2016 and WY2017. The histogram shows the collective distribution of azimuthal differences. Locations of noted seasonal phase (from Figure 3.4) are labeled for reference.

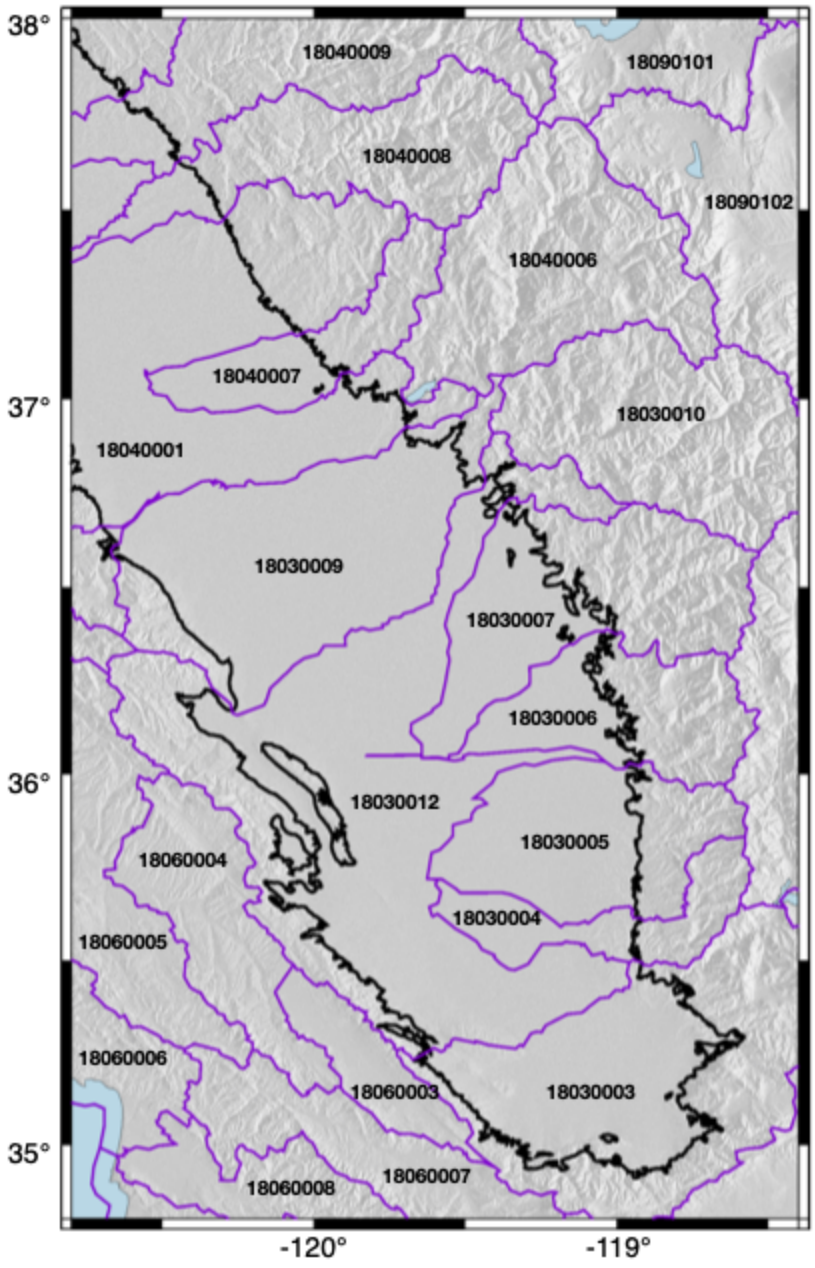

Figure 3.S11: Boundaries for the level 8 hydrological unit codes across the San Joaquin Valley. Runoff values from 18030003, 18030004, 18030005, 18030006, 18030007, 18030009, 18030012, 18040001, and 18040007 were used to compare with peak seasonal uplift timing (Figure 3.6 in the main text).

Table 3.S1: List of dates and perpendicular baselines ($B_\perp$) for Sentinel-1 synthetic aperture radar (SAR) data used in this study. Sentinel-1 data is publicly accessible via the European Space Agency's Copernicus Open Access Hub (https://scihub.copernicus.eu/) and the Alaska Satellite Facility (https://www.asf.alaska.edu/).

Mission	Day	Month	Year	B (m)
Sentinel-1A	1	4	2015	-52.7
Sentinel-1A	25	4	2015	-115.9
Sentinel-1A	19	5	2015	-14.9
Sentinel-1A	12	6	2015	30.4
Sentinel-1A	6	7	2015	-91.3
Sentinel-1A	30	7	2015	34.8
Sentinel-1A	23	8	2015	-0.1
Sentinel-1A	16	9	2015	-87.2
Sentinel-1A	10	10	2015	-20.1
Sentinel-1A	3	11	2015	-19.1
Sentinel-1A	27	11	2015	54.1
Sentinel-1A	21	12	2015	-20.2
Sentinel-1A	14	1	2016	-52.7
Sentinel-1A	7	2	2016	73.9
Sentinel-1A	2	3	2016	-57.9
Sentinel-1A	26	3	2016	11.5
Sentinel-1A	19	4	2016	-3.5
Sentinel-1A	13	5	2016	-68.2
Sentinel-1A	6	6	2016	7.7
Sentinel-1A	24	7	2016	-58.9
Sentinel-1A*	17	8	2016	0.0
Sentinel-1A	10	9	2016	-71.9
Sentinel-1A	4	10	2016	17.5
Sentinel-1A	28	10	2016	30.9
Sentinel-1A	15	12	2016	55.5
...	...	...	...	...

Mission	Day	Month	Year	B (m)
Sentinel-1A	8	1	2017	-32.4
Sentinel-1B	14	1	2017	69.3
Sentinel-1A	20	1	2017	-95.8
Sentinel-1B	26	1	2017	28.8
Sentinel-1A	1	2	2017	-63.3
Sentinel-1A	25	2	2017	24.8
Sentinel-1A	9	3	2017	-40.7
Sentinel-1A	21	3	2017	-117.3
Sentinel-1A	2	4	2017	-78.2
Sentinel-1A	14	4	2017	-17.8
Sentinel-1A	26	4	2017	-20.1
Sentinel-1A	8	5	2017	49.3
Sentinel-1A	20	5	2017	-27.7
Sentinel-1A	1	6	2017	-116.2
Sentinel-1A	13	6	2017	-45.1
Sentinel-1A	25	6	2017	16.0
Sentinel-1A	7	7	2017	-40.4
Sentinel-1A	19	7	2017	-102.6
Sentinel-1A	31	7	2017	-26.9
Sentinel-1A	12	8	2017	-41.2
Sentinel-1A	24	8	2017	-2.1
Sentinel-1A	5	9	2017	-20.7
Sentinel-1A	17	9	2017	13.1
Sentinel-1A	29	9	2017	-47.8
Sentinel-1A	11	10	2017	-46.3
Sentinel-1A	23	10	2017	14.3

* Primary reference image used to align other acquisitions.

Table 3.S2: Summary of interferometric connections and baselines for the full time series, WY2016, and WY2017.

Time Period	Acquisitions	Mean connections per acquisition	Median connections per acquisition	Number of pairs	Mean perpendicular baseline (m)	Standard deviation perpendicular baseline (m)
April 2015 to October 2017	51	10.6	10	263	-23.2	49.4
WY2016 (October 2015 to September 2016)	15	7.3	7	53	-13.9	43.6
WY2017 (October 2016 to September 2017)	28	13.4	14	188	-24.2	50.7

Table 3.S3: List of Global Positioning System (GPS) stations and their locations (decimal degrees; east longitude and latitude) used to correct each interferogram. These locations can be seen in Figure 3.1 (gray squares). Data is from the Plate Boundary Observatory network, a part of the National Science Foundation's Geodesy Advancing Geosciences and EarthScope (GAGE) facility. Non-geophysical offsets are corrected then smoothed using a 6-day Gaussian filter, and the three component (North, East, and Vertical) displacements are projected into the synthetic aperture radar (SAR) line-of-sight direction. The raw GPS time series data is available from UNAVCO (ftp://data-out.unavco.org/pub/products).

Station	Latitude	Longitude
ARM1	35.2013	-118.9104
BBDM	34.5822	-119.9815
BCWR	34.9205	-119.4058
BEPK	35.8784	-118.0741
BVPP	35.1573	-119.3475
CHMS	34.6405	-117.8277
CTDM	34.5165	-118.6132
CUHS	34.9426	-119.6739
EDPP	34.9462	-118.8304
ELTN	34.7031	-118.4257
FGST	34.7330	-120.0094
GR8R	36.3990	-120.4157
HIVI	34.7599	-117.7995
ISLK	35.6623	-118.4743
LAND	35.8998	-120.4733
LVMS	34.7336	-119.1037
MUSB	37.1699	-119.3094
ORES	34.7391	-120.2786
OZST	34.6834	-119.3534
P056	36.0274	-119.0629
P093	36.6060	-117.9941
P245	37.7131	-119.7061
P290	36.1789	-120.7283
P291	35.9228	-120.6448
P294	36.1232	-120.4399
P301	36.8063	-120.7431
P302	36.6347	-120.6186
P303	37.0544	-120.7053
P304	36.7390	-120.3566
...	...	...

Station	Latitude	Longitude
P305	37.3522	-120.1968
P306	37.7952	-120.6445
P307	36.9473	-120.0579
P311	37.1776	-118.5198
P465	36.4668	-118.1324
P466	36.5312	-117.7895
P468	36.9757	-118.1184
P469	37.2314	-117.9358
P512	37.5626	-119.6944
P513	34.9073	-120.6502
P514	35.0107	-120.4097
P518	35.0200	-120.0753
P520	34.6305	-119.6164
P521	34.8886	-119.8154
P523	35.3044	-120.8603
P525	35.4258	-120.8081
P526	35.6360	-120.8697
P528	35.3278	-120.5454
P529	35.4405	-120.3538
P530	35.6248	-120.4804
P532	35.6338	-120.2670
P536	35.2798	-120.0250
P537	35.3168	-119.9353
P538	35.5342	-120.1125
P544	35.7313	-119.7380
P546	35.9279	-120.1549
P547	35.9347	-119.9094
P549	34.5996	-119.3263
P553	34.8351	-118.8790
...	...	...

Station	Latitude	Longitude
P562	34.9821	-118.1887
P563	35.4187	-119.4212
P564	35.6229	-119.3494
P565	35.7439	-119.2367
P566	36.3245	-119.2293
P567	35.4209	-118.7536
P569	35.3780	-118.1238
P570	35.6673	-118.2600
P571	36.2314	-118.7667
P572	36.5855	-118.9546
P573	36.0931	-118.2605
P616	35.4246	-117.8933
P630	37.6130	-119.0004
P632	37.7857	-119.0861
P639	37.6546	-118.8687
P647	37.7544	-118.7677
P652	37.5892	-118.2385
P653	37.7375	-118.4717
P724	37.4395	-118.5611
P725	37.0889	-119.7456
P726	37.2805	-118.1467
P727	37.2736	-118.4668
P812	35.1525	-118.0165
RBRU	36.7591	-119.8287
RSTP	34.8751	-118.1929
RSVY	34.5415	-119.1844
THCP	35.1582	-118.4146
VNDP	34.5563	-120.6165
VNPS	34.5015	-118.1212
WGPP	35.0108	-118.9837

Table 3.S4: Validation summary for the full time series, WY2016, and WY2017. Independent continuous Global Positioning System (cGPS) velocities and time series were projected into the synthetic aperture radar (SAR) line-of-sight to assess the GPS-enhanced InSAR surface displacements.

Time Period	Velocity residual median (mm/yr)	Velocity residual σ_r (mm/yr)	Time series residual σ_r (mm)
April 2015 to October 2017	-0.3	2.9	4.3
WY2016 (October 2015 to September 2016)	-0.8	6.4	3.2
WY2017 (October 2016 to September 2017)	-3.7	11.1	4.0

References

Adusumilli, S., A. A. Borsa, M. A. Fish, H. K. McMillan, and F. Silverii (2019), A Decade of Water Storage Changes Across the Contiguous United States From GPS and Satellite Gravity, *Geophysical Research Letters*, *46*(22), 13,006–13,015, doi:10.1029/2019GL085370.

Argus, D. F., Landerer Felix W., Wiese David N., Martens Hilary R., Fu Yuning, Famiglietti James S., Thomas Brian F., Farr Thomas G., Moore Angelyn W., and Watkins Michael M. (2017), Sustained Water Loss in California's Mountain Ranges During Severe Drought From 2012 to 2015 Inferred From GPS, *Journal of Geophysical Research: Solid Earth*, *122*(12), 10,559–10,585, doi:10.1002/2017JB014424.

Bell, J. W., F. Amelung, A. Ferretti, M. Bianchi, and F. Novali (2008), Permanent scatterer InSAR reveals seasonal and long-term aquifer-system response to groundwater pumping and artificial recharge, *Water Resources Research*, *44*(2), doi:10.1029/2007WR006152.

Berardino, P., G. Fornaro, R. Lanari, and E. Sansosti (2002), A new algorithm for surface deformation monitoring based on small baseline differential SAR interferograms, *IEEE Transactions on Geoscience and Remote Sensing*, *40*(11), 2375–2383, doi:10.1109/TGRS.2002.803792.

Borsa, A. A., J.-B. Minster, B. G. Bills, and H. A. Fricker (2007), Modeling long-period noise in kinematic GPS applications, *Journal of Geodesy*, *81*(2), 157–170, doi:10.1007/s00190-006-0097-x.

Borsa, A. A., D. C. Agnew, and D. R. Cayan (2014), Ongoing drought-induced uplift in the western United States, *Science*, *345*(6204), 1587–1590, doi:10.1126/science.1260279.

California Department of Water Resources (2021), Bulletin 132.

Castellazzi, P., R. Martel, D. L. Galloway, L. Longuevergne, and A. Rivera (2016), Assessing Groundwater Depletion and Dynamics Using GRACE and InSAR: Potential and Limitations, *Groundwater*, *54*(6), 768–780, doi:10.1111/gwat.12453.

Chaussard, E., and T. G. Farr (2019), A New Method for Isolating Elastic From Inelastic Deformation in Aquifer Systems: Application to the San Joaquin Valley, CA, *Geophysical Research Letters*, *46*(19), 10,800–10,809, doi:10.1029/2019GL084418.

Chen, C. W., and H. A. Zebker (2000), Network approaches to two-dimensional phase unwrapping: intractability and two new algorithms, *Journal of the Optical Society of America A*, *17*(3), 401–414, doi:10.1364/JOSAA.17.000401.

Colesanti, C., A. Ferretti, F. Novali, C. Prati, and F. Rocca (2003), SAR monitoring of progressive and seasonal ground deformation using the permanent scatterers technique, *IEEE Transactions on Geoscience and Remote Sensing*, *41*(7), 1685–1701, doi:10.1109/TGRS.2003.813278.

Enzminger, T. L., E. E. Small, and A. A. Borsa (2019), Subsurface Water Dominates Sierra Nevada Seasonal Hydrologic Storage, *Geophysical Research Letters*, *46*(21), 11,993–12,001, doi:10.1029/2019GL084589.

Famiglietti, J. S., M. Lo, S. L. Ho, J. Bethune, K. J. Anderson, T. H. Syed, S. C. Swenson, C. R. de Linage, and M. Rodell (2011), Satellites measure recent rates of groundwater depletion in California's Central Valley, *Geophysical Research Letters*, *38*(3), L03,403, doi:10.1029/2010GL046442.

Farr, T. G. (2018), Insar Measurements of Subsidence and Rebound in California, in *IGARSS 2018 - 2018 IEEE International Geoscience and Remote Sensing Symposium*, pp. 8401–8403, doi:10.1109/IGARSS.2018.8517774.

Farr, T. G., and L. Zhen (2014), Monitoring Subsidence Associated with Groundwater Dynamics in the Central Valley of California Using Interferometric Radar, *Remote Sensing of the Terrestrial Water Cycle*, doi:10.1002/9781118872086.ch24.

Farr, T. G., P. A. Rosen, E. Caro, R. Crippen, R. Duren, S. Hensley, M. Kobrick, M. Paller, E. Rodriguez, L. Roth, D. Seal, S. Shaffer, J. Shimada, J. Umland, M. Werner, M. Oskin, D. Burbank, and D. Alsdorf (2007), The Shuttle Radar Topography Mission, *Reviews of Geophysics*, *45*(2), RG2004, doi:10.1029/2005RG000183.

Faunt, C. C. (Ed.) (2009), *Groundwater availability of the Central Valley Aquifer, California*, no. 1766 in U.S. Geological Survey professional paper, U.S. Geological Survey, Reston, Va.

Faunt, C. C., K. Belitz, and R. T. Hanson (2010), Development of a three-dimensional model of sedimentary texture in valley-fill deposits of Central Valley, California, USA, *Hydrogeology Journal*, *18*(3), 625–649, doi:10.1007/s10040-009-0539-7.

Faunt, C. C., M. Sneed, J. Traum, and J. T. Brandt (2016), Water availability and land subsidence in the Central Valley, California, USA, *Hydrogeology Journal*, *24*(3), 675–684, doi:10.1007/s10040-015-1339-x.

Fetter, C. W. (2018), *Applied Hydrogeology: Fourth Edition*, Waveland Press.

Fu, Y., D. F. Argus, and F. W. Landerer (2015), GPS as an independent measurement to estimate terrestrial water storage variations in Washington and Oregon, *Journal of Geophysical Research: Solid Earth*, *120*(1), 2014JB011,415, doi:10.1002/2014JB011415.

Hanson, R. T., L. E. Flint, A. L. Flint, M. D. Dettinger, C. C. Faunt, D. Cayan, and W. Schmid (2012), A method for physically based model analysis of conjunctive use in response to potential climate changes, *Water Resources Research*, *48*(6), W00L08, doi:10.1029/2011WR010774.

Herring, T. A., T. I. Melbourne, M. H. Murray, M. A. Floyd, W. M. Szeliga, R. W. King, D. A. Phillips, C. M. Puskas, M. Santillan, and L. Wang (2016), Plate Boundary Observatory and related networks: GPS data analysis methods and geodetic products, *Reviews of Geophysics*, *54*(4), 2016RG000,529, doi:10.1002/2016RG000529.

Howitt, R., D. MacEwan, J. Medellín-Azuara, J. Lund, and D. Sumner (2015), Economic Analysis of the 2015 Drought For California Agriculture, p. 31.

Ingraham, N. L., and B. E. Taylor (1991), Light stable isotope systematics of large-scale hydrologic regimes in California and Nevada, *Water Resources Research*, *27*(1), 77–90, doi:10.1029/90WR01708.

Ireland, R., J. Poland, and F. Riley (1984), Land subsidence in the San Joaquin Valley, California, as of 1980, *USGS Numbered Series 437-l*.

Jeanne, P., T. G. Farr, J. Rutqvist, and D. W. Vasco (2019), Role of agricultural activity on land subsidence in the San Joaquin Valley, California, *Journal of Hydrology*, *569*, 462–469, doi:10.1016/j.jhydrol.2018.11.077.

Lau, N., A. A. Borsa, and T. W. Becker (2020), Present-Day Crustal Vertical Velocity Field for the Contiguous United States, *Journal of Geophysical Research: Solid Earth*, *125*(10), e2020JB020,066, doi:https://doi.org/10.1029/2020JB020066.

Leake, S. A. (1990), Interbed storage changes and compaction in models of regional groundwater flow, *Water Resources Research*, *26*(9), 1939–1950, doi:10.1029/WR026i009p01939.

Levy, M. C., W. R. Neely, A. A. Borsa, and J. A. Burney (2020), Fine-scale spatiotemporal variation in subsidence across California's San Joaquin Valley explained by groundwater demand, *Environmental Research Letters*, *15*(10), 104,083, doi:10.1088/1748-9326/abb55c.

Lund, J. R., J. Medellin-Azuara, J. Durand, and K. Stone (2018), Lessons from California's 2012-2016 drought, *Journal of Water Resources Planning and Management*, *144*(10), 04018,067, doi:10.1061/(ASCE)WR.1943-5452.0000984.

Meixner, T., A. H. Manning, D. A. Stonestrom, D. M. Allen, H. Ajami, K. W. Blasch, A. E. Brookfield, C. L. Castro, J. F. Clark, D. J. Gochis, A. L. Flint, K. L. Neff, R. Niraula, M. Rodell, B. R. Scanlon, K. Singha, and M. A. Walvoord (2016), Implications of projected climate change for groundwater recharge in the western United States, *Journal of Hydrology*, *534*, 124–138, doi:10.1016/j.jhydrol.2015.12.027.

Murray, K. D., and R. B. Lohman (2018), Short-lived pause in Central California subsidence after heavy winter precipitation of 2017, *Science Advances*, *4*(8), eaar8144, doi:10.1126/sciadv.aar8144.

Neely, W. R., A. A. Borsa, and F. Silverii (2020), GInSAR: A cGPS Correction for Enhanced InSAR Time Series, *IEEE Transactions on Geoscience and Remote Sensing*, *58*(1), 136–146, doi:10.1109/TGRS.2019.2934118.

Ojha, C., M. Shirzaei, S. Werth, D. F. Argus, and T. G. Farr (2018), Sustained Groundwater Loss in California's Central Valley Exacerbated by Intense Drought Periods, *Water Resources Research*, *54*(7), 4449–4460, doi:10.1029/2017WR022250.

Ojha, C., S. Werth, and M. Shirzaei (2019), Groundwater Loss and Aquifer System Compaction in San Joaquin Valley During 2012–2015 Drought, *Journal of Geophysical Research: Solid Earth*, *124*(3), 3127–3143, doi:10.1029/2018JB016083.

Page, R. W. (1986), *Geology of the Fresh Ground-water Basin of the Central Valley, California: With Texture Maps and Sections*, U.S. Government Printing Office.

Poland, J. F., and G. H. Davis (1969), Land Subsidence Due To Withdrawal Of Fluids, in *Reviews in Engineering Geology*, vol. 2, pp. 187–270, Geological Society of America, doi:10.1130/REG2-p187.

Prats-Iraola, P., R. Scheiber, L. Marotti, S. Wollstadt, and A. Reigber (2012), TOPS Interferometry With TerraSAR-X, *IEEE Transactions on Geoscience and Remote Sensing*, *50*(8), 3179–3188, doi:10.1109/TGRS.2011.2178247.

Public Policy Institute of California (2019), PPIC San Joaquin Valley Water Balance 1988-2017.

San Joaquin Valley Drainage Program (1990), A Management Plan For Agricultural Subsurface Drainage and Related Problems on the Westside San Joaquin Valley, *Tech. rep.*, U.S. Department of the Interior and California Resources Agency, Sacramento, CA.

Sandwell, D., R. Mellors, X. Tong, M. Wei, and P. Wessel (2011), Open radar interferometry software for mapping surface Deformation, *Eos, Transactions American Geophysical Union*, *92*(28), 234–234, doi:10.1029/2011EO280002.

Sandwell, D. T., Y. Zeng, Z.-K. Shen, B. Crowell, J. Murray, R. McCaffrey, and X. Xu (2016), The SCEC community geodetic model V1: Horizontal velocity grid, *SCEC Annu. Meeting*.

Scanlon, B. R., C. C. Faunt, L. Longuevergne, R. C. Reedy, W. M. Alley, V. L. McGuire, and P. B. McMahon (2012), Groundwater depletion and sustainability of irrigation in the US High Plains and Central Valley, *Proceedings of the National Academy of Sciences*, *109*(24), 9320–9325, doi:10.1073/pnas.1200311109.

Scanlon, B. R., R. C. Reedy, C. C. Faunt, D. Pool, and K. Uhlman (2016), Enhancing drought resilience with conjunctive use and managed aquifer recharge in California and Arizona, *Environmental Research Letters*, *11*(3), 035,013, doi:10.1088/1748-9326/11/3/035013.

Schmidt, D. A., and R. Bürgmann (2003), Time-dependent land uplift and subsidence in the Santa Clara valley, California, from a large interferometric synthetic aperture radar data set, *Journal of Geophysical Research: Solid Earth*, *108*(B9), 2416, doi:10.1029/2002JB002267.

Serpelloni, E., F. Pintori, A. Gualandi, E. Scoccimarro, A. Cavaliere, L. Anderlini, M. E. Belardinelli, and M. Todesco (2018), Hydrologically Induced Karst Deformation: Insights From GPS Measurements in the Adria-Eurasia Plate Boundary Zone, *Journal of Geophysical Research: Solid Earth*, *123*(5), 4413–4430, doi:https://doi.org/10.1002/2017JB015252.

Silverii, F., N. D'Agostino, A. A. Borsa, S. Calcaterra, P. Gambino, R. Giuliani, and M. Mattone (2019), Transient crustal deformation from karst aquifers hydrology in the Apennines (Italy), *Earth and Planetary Science Letters*, *506*, 23–37, doi:10.1016/j.epsl.2018.10.019.

Smith, R. G., R. Knight, J. Chen, J. A. Reeves, H. A. Zebker, T. Farr, and Z. Liu (2017), Estimating the permanent loss of groundwater storage in the southern San Joaquin Valley, California, *Water Resources Research*, *53*(3), 2133–2148, doi:10.1002/2016WR019861.

Terzaghi, K. (1925), Structure and Volume of voids in soils, translated from Erdbaumechanik auf bodenphysikalischer grundlage, in *From Theory to Practice in Soil Mechanics*, John Wiley, New York.

U. S. Geological Survey (2019), USGS Water Data for the Nation, doi:10.5066/F7P55KJN.

U.S. Bureau of Reclamation (2020), 2020 Water Delivery Monthly Tables.

Visser, A., J. E. Moran, M. J. Singleton, and B. K. Esser (2018), Importance of river water recharge to the San Joaquin Valley groundwater system, *Hydrological Processes*, *32*(9), 1202–1213, doi:10.1002/hyp.11468.

Wang, J., Y. Deng, R. Wang, P. Ma, and H. Lin (2019), A Small-Baseline InSAR Inversion Algorithm Combining a Smoothing Constraint and L_1-Norm Minimization, *IEEE Geoscience and Remote Sensing Letters*, pp. 1–5, doi:10.1109/LGRS.2019.2893422.

Weissmann, G. S., G. L. Bennett, and A. L. Lansdale (2005), Factors controlling sequence development on Quaternary fluvial fans, San Joaquin Basin, California, USA, in *Alluvial Fans: Geomorphology, Sedimentology, Dynamics*, vol. 251, pp. 169–186, Geological Society of London.

Wessel, P., W. H. F. Smith, R. Scharroo, J. Luis, and F. Wobbe (2013), Generic Mapping Tools: Improved Version Released, *Eos, Transactions American Geophysical Union*, *94*(45), 409–410, doi:10.1002/2013EO450001.

Williamson, A. K., D. E. Prudic, and L. A. Swain (1989), *Ground-Water Flow in the Central Valley, California: Regional aquifer-system analysis - Central Valley, California*, vol. 1401-D, U.S. Geological Survey Professional Paper.

Xu, X., D. T. Sandwell, E. Tymofyeyeva, A. González-Ortega, and X. Tong (2017), Tectonic and Anthropogenic Deformation at the Cerro Prieto Geothermal Step-Over Revealed by Sentinel-1A InSAR, *IEEE Transactions on Geoscience and Remote Sensing*, *PP*(99), 1–9, doi:10.1109/TGRS.2017.2704593.

Chapter 4

Analysis of *in-situ* periodic groundwater level measurements over California's Central Valley

Abstract

4.1 Introduction

Access to freshwater resources has played a crucial role in human interaction with the environment and the development of population centers. The first major human settlements were focused near plentiful sources of water such as rivers, lakes, and natural springs (*Yevjevich*, 1992). So important were and are these resources that changes in local to regional water availability have led to the rise and fall of civilizations. Modern

cities and towns are still reflective of this dependence on freshwater with over 50% of the global population living within 3 km of a surface water source and fewer than 10% living farther away than 10 km (*Kummu et al.*, 2011). Where and when access to surface water is limited, water can be routed from distant sources. The development of water conveyance technologies such as aqueducts and pipelines have allowed for the transformation of inhospitable environments for human settlement. Where the importation of water from afar is too challenging, too costly, or not feasible, wells can be constructed to tap groundwater resources.

Groundwater reservoirs are commonly referred to as a "savings account". The idea being that extraction occurs only during times when surface water is limited or unavailable and is replenished during wet periods. The use of groundwater via wells dates back to the Neolitic era (*Galili and Nir*, 1993). These wells were hand dug up to depths of 10 m. In many rural and/or developing regions, hand dug wells are still common practice. Using modern technologies, wells for industrial scale groundwater extraction can routinely be drilled to hundreds of meters depth. Access to these deeper sources of water have allowed for longer and more productive growing cycles in arid to semi-arid environments. However, overexploitation of groundwater reservoirs may lead to permanent storage loss, jeopardizing the availability of future water (*Scanlon et al.*, 2012). For the protection and sustainability of these groundwater resources, it is paramount to characterize groundwater levels (GWL) at local to aquifer-wide scales with sufficient spatio-temporal resolution.

4.1.1 Central Valley Aquifer System

For California's Central Valley, the utilization of groundwater has transformed the region into one of the most productive agricultural hubs in the world (*Howitt et al.*, 2015) as well as provide potable water to millions of residents. The Central Valley Aquifer System is a sediment-filled structural depression bounded by the Sierra Nevada ranges to the east, the Tehachapi Mountains to south, the Coast Ranges to the west, and the Cascade Range to the north. As rivers sourced in the surrounding mountain ranges enter the valley, they deposited an interbedded mix of coarser gravel and sands with finer-grained deposits of clays and silt (*Page*, 1986; *Weissmann et al.*, 2005). This alluvial fill provides the granular matrix for the aquifer system with the silt and clay lenses acting as impediments to groundwater flow (or aquitards). In the sounthern Central Valley, the subsurface is often conceptualized as a two-tiered system with a deeper confined aquifer and a shallower unconifined-to-semiconfined aquifer separated by the largest regional clay package, the Corcoran clay (*Page*, 1986; *Faunt*, 2009).

The valley climate is arid to semi-arid hot with precipitation falling as rain and snow over the mountain ranges (predominately in the north and east) which drains into major river systems that enter the valley or into reservoirs. This surface water is then routed throughout the valley to support agricultural, industrial, and urban demand. During average water years (with a water year beginning October 1 and ending September 30), a majority of precipitation ($\sim 85\%$) occurs between November and April (*Faunt*, 2009; *Williamson et al.*, 1989) making the summers dry. To support the water

demand not met by surface water, groundwater is extracted and used. In an average year, groundwater contributes roughly 40% of total water use (*Faunt et al.*, 2016).

4.1.2 California's Drought Response

Over the past several decades, the state of California has experienced multiple periods of drought (Figure 4.1). This has led to increased stress on regional aquifers as groundwater is used to meet the water demand of crops unfulfilled by surface-water resources alone (*Hanson et al.*, 2012) with up to 70% of total water use sourced from groundwater (*Faunt et al.*, 2016). As such, California's Central Valley has seen its groundwater levels decline resulting in land subsidence related to dewatering of fine-grained clay and silt aquitards (*Chaussard and Farr*, 2019; *Famiglietti et al.*, 2011; *Faunt et al.*, 2016; *Jasechko and Perrone*, 2020; *Murray and Lohman*, 2018; *Neely et al.*, 2021; *Ojha et al.*, 2018, 2019; *Scanlon et al.*, 2012).

The California government passed legislation in 2014 to address and protect against the decline and degradation of the state's groundwater stores. The Sustainable Groundwater Management Act (SGMA) created a framework that allows local agencies to best determine groundwater management strategies in accordance with state guidelines. This led to the establishment of over 260 Groundwater Sustainability Agencies (GSAs) in high- and medium-priority basins, each tasked with developing and implementing Groundwater Sustainability Plans (GSPs) detailing how these groundwater basins will reach long term sustainability. GSPs are designed so each basin avoids six undesirable results: (i) lowering of groundwater levels, (ii) reduction in groundwater

storage, (iii) seawater intrusion, (iv) degraded quality, (v) land subsidence, and (vi) surface water depletion. While the observation and understanding of groundwater resources at an agency-level scale is critical to the success of SGMA, there is benefit in the assessment of the state of groundwater across the entire valley.

4.1.3 Objective

Here we analyze readily available groundwater level (GWL) records and generate a monthly time series of GWL conditions across the CV between 2009 and 2019. We assess the suitability of this dataset for identifying patterns in groundwater levels as they respond to natural and anthropogenic influences during periods of high and low surface water availability. Further, GWL records in the San Joaquin Valley (southern portion of the CV; SJV) are placed in the context of seasonal and longer-term surface deformation as observed by a joint GPS (global positioning system) and InSAR (interferometric synthetic aperture radar) dataset (*Neely et al.*, 2020, 2021).

4.2 Data and Methods

4.2.1 Monitoring Wells

Monitoring wells are the most direct method for measuring the current state of groundwater levels and are often used in the determination of groundwater storage (*Jasechko and Perrone*, 2020; *Kim et al.*, 2020). However, a single measurement is limited to the hydrogeological unit the well samples and is specific to the time of the

observation. The use of multiple monitoring well observations to characterize the aquifer system across space and time better informs our understanding of the heterogeneity of the system and its response to various climatological regimes (e.g. periods of drought or surplus of surface-water supplies).

While there is an abundance of *in-situ* GWL observations in California, access to these data may be limited and/or inconsistent due to differing collection and reporting processes. In an effort to establish a publicly accessible and permanent network of groundwater monitoring wells for achieving goals outlined in state legislature, the California Department of Water Resources (DWR) hosts state-wide databases of groundwater elevation observations. Focusing on observations within the Central Valley alluvial boundary and between the 2010-2019 water years (October 1, 2009 to September 30, 2019), we have access to 201,520 quality well measurements from 9,666 unique monitoring well stations in DWR's "Periodic Groundwater Level Measurements" dataset (with wells tpically sampled once or twice a year).

4.2.2 Quality Control and Perforation Categorization

Many well level observations are subjected to local or nearby effects that make their inclusion into a regional groundwater level estimation undesirable. In particular, the influence of active or recent use/recharge provide an imprecise characterization of equilibrated head levels. To discriminate against such measurements, we omit well observations that are flagged as "pumping", "pumped recently", "nearby pump operating", "recharge or surface water effects near well", "oil or foreign substance in casing", or "dry

well".

Previously noted, monitoring wells record groundwater conditions specific to the individual water-bearing hydrogeological units they sample. In the southern Central Valley, the aquifer system is often conceptualized as a shallower unconfined to semiconfined unit stacked on top of a deeper confined unit with the Corcoran clay unit acting as the confining layer between the two. Thus, where available, we categorize the well observations as shallow or deep based on the well perforation depths. To this aim, we simply take a representative depth to Corcoran clay ($\sim$ 120 m) (*Faunt*, 2009) as a discrimination between "shallow" and "deep" observations.

4.2.3 Groundwater Level Spatial Gridding

While monitoring well station locations span the whole of the Central Valley, station density varies across sub-basins reflecting intensities of groundwater use and management strategies. The heterogeneity of observations is also a product of the frequency of data collection. For example, despite there being more stations in the southern and central portions of the valley, the stations to the north collect orders of magnitude more observations (*Kim et al.*, 2020).

In an attempt to avoid spatially biasing our results, we create a framework to uniformly sample the available well data by establishing a 0.1° x 0.1° grid over the CV. For each grid cell, we select the median value of groundwater elevation of the available wells on monthly intervals. We do this for shallow, deep, and all wells. However, not all grid cells contain a valid measurement. We then fit a surface to these points for

each time slice using GRIDFIT (*D'Errico*, 2005). Rather than directly interpolating scattered GWL values, this surface fitting technique approximates a smooth surface that represents general behavior of the provided data. GRIDFIT makes use a triangular (linear) interpolation scheme and a gradient based regularizer designed to be biased towards smooth directional derivatives across grid cell boundaries.

4.2.4 Surface Displacements

Using data from the European Space Agency's C-band Sentinel-1A/B synthetic aperture radar (SAR) mission (descending track 144), we estimate the spatio-temporal evolution of surface elevation displacements across the San Joaquin Valley spanning April 1 2015 to October 1 2019. We generate a suite of 769 interferograms from 114 SAR images using GMTSAR (*Sandwell et al.*, 2011). We geometrically align images to a primary reference image on August 17, 2016 and construct our interferometric pairs using a maximum perpendicular baseline of 250 m and a maximum separation of 100-days. The contribution of topographic phase is removed from each interferogram using the Shuttle Radar Topography Mission (SRTM) (*Farr et al.*, 2007) 1 arc second digital elevation model (DEM). Due to observed burst discontinuities resulting from misregistration, we elect to apply the enhanced spectral diversity (ESD) algorithm (*Prats-Iraola et al.*, 2012). Interferometric pairs are then unwrapped following the Statistical-Cost, Network-Flow Algorithm for Phase Unwrapping (SNAPHU) (*Chen and Zebker*, 2000) with an unwrapping pixel correlation threshold of 0.1. The interferograms in unwrapped phase are converted into line-of-sight displacements with a spatial resolution of $\sim$ 100 m.

4.2.5 GInSAR Correction and Time Series Construction

To reduce long-wavelength noise present in interferometric estimates of land surface elevations and to provide each interferogram a common absolute reference, we leverage continuous Global Positioning System (GPS) daily displacement time series from the National Science Foundation's Geodesy Advancing Geosciences and EarthScope (GAGE) facility (*Herring et al.*, 2016). These GPS time series data are atmospherically corrected and generally taken to be higher fidelity estimates displacement than InSAR estimates. Using a subset of stations within our interferometric coverage, we correct the time series for offsets due to nongeophysical changes (e.g. equipment changes/upgrades), smooth the data using a Gaussian filter (6-day window) to minimize higher frequency signals (e.g. multipath and tropospheric effects) (*Borsa et al.*, 2007), and project the combined north, east, and vertical components into the SAR line-of-sight (LOS) direction. Following the GPS-enhanced InSAR (GInSAR) methodology (*Neely et al.*, 2020), the residual displacements between GPS and InSAR estimates are calculated at each GPS station. For each interferogram, we fit a low-order polynomial surface (2nd order in longitude and 4th order in latitude) to the residuals. These models are used to correct the suite of interferograms to be used in the time series inversion. A detailed guide to this method and strategies for parameter selection is presented in *Neely et al.* (2020, 2021).

To estimate the temporal evolution of surface displacements from our GInSAR results, we adopt a modified version of the Small Baseline Subset (SBAS) algorithm

(*Berardino et al.*, 2002). While standard SBAS techniques require pixel coherence in every interferogram, the temporally Connected SBAS (CSBAS) algorithm (*Neely et al.*, 2020) that we use retains a higher level of pixel coverage by only requiring at least one displacement estimate spanning each acquisition date. This is particularly beneficial for investigations over heavily vegetated region such as the Central Valley were pixel coherence is lower (*Wei and Sandwell*, 2010). Additionally, we temporally smooth during the least squares estimation using a first-order Tikhonov regularization (smoothing constraint $\lambda = 150$) to minimize large changes in displacement velocity (*Schmidt and Bürgmann*, 2003; *Wang et al.*, 2019). Finally, we remove the LOS-projected horizontal surface motion from our time series using the Southern California Earthquake Center (SCEC) Community Geodetic Model (CGM) (*Sandwell et al.*, 2016) and scale the residual by the cosine of the radar incidence angle in order to isolate the vertical component of displacement.

4.2.6 Time Series Modeling

Neely et al. (2021) demonstrated how a temporal decomposition and simple modeling of surface displacement data over the San Joaquin Valley can provide unique insights into the poroelastic response under wet and dry conditions. We expand that analysis here to the gridded GWL surfaces and additional years of surface displacement observations. On a pixel-by-pixel basis, we estimate the annual seasonal response (amplitude and timing) of our groundwater level surfaces and displacement data using a

model described by a simple sinusoid with a linear trend

$$Y(t) = vt + A\cos 2\pi(t - T) + Y_0 \tag{4.1}$$

where $Y(t)$ describes the observable (m for GWL; mm for displacements), t is the time in fractional years, v is the linear rate of change (m/yr for GWL; mm/yr for displacements), A is the seasonal amplitude (m for GWL; mm for displacements), T is the time of relative peak in the seasonal signal (where $T = 0$ corresponds to October 1), and Y_0 is a constant shift in the model (m for GWL; mm for displacements). We use least-squares minimization to estimate the model parameters and map v, A, and T across our study region (Figures 4.2-4.8). For the purposes of this investigation, we consider water years WY2012-2016 and WY2018 as "dry" years and WY2010-2011, WY2017, and WY2019 as "wet" years using the U.S. Drought Monitor as our basis (Figure 4.1).

4.2.7 Time Series Decomposition

To further assess similarities and differences in signal between GWL (approximated through surface fitting methods) and land surface displacements, we employ an empirical orthogonal function (EOF) analysis (also referred to as principal component analysis) on each dataset. This type of analysis is a multivariate statistical technique that separates signal in the data into orthogonal basis functions ordered by fractional variance (*Abdi and Williams*, 2010). The EOF analyis can be performed using a singular value decomposition with the data, X, decomposed into the following

$$X = P\Delta Q^T \tag{4.2}$$

where P are the *left singular vectors* (eigenvectors of XX^T), Δ is the diagonal matrix of *singular values*, and Q are the *right singular vectors* (eigenvectors of X^TX). Here, the columns of P are the EOFs and the amplitudes are the columns of the product of the singular values and the transpose of the right singular vectors, ΔQ^T. As EOFs are mathematical representations of linearly independent components of the data, they do not correspond one-to-one to physical processes. However, dominant physical processes should be represented in the first several EOFs and thus provide insight into the data.

4.3 Results and Discussion

4.3.1 Validation with original GWL records

To assess the gridded GWL products, we extract individual time series at locations where we have collocated displacement observations and monitoring well records with relatively frequent sampling. In general, we find that the gridded products exhibit large changes in GWL (10s of meters) not observed in the monitoring well records (panel 2 in Figures 4.9-4.11). Despite these large short-period oscillations, the gridded time series do capture the first order behavior evident in the original well data. Turning our attention to models of the annual rate of change and seasonal component (using equation 4.1), we find a single sinusoid and linear trend sufficiently represent a majority

of the signal observed in original well data and the displacement observations while the large swings of GWL in the gridded time series appears to bias the fit. This may result in disagreements between peak seasonal GWL timing of up to half a year compared to the original groundwater well record (e.g., Figure 4.10). However, for some years and locations, the estimated seasonal parameters consistently match the fits to the observed data to within a month (e.g., Figure 4.11). The seasonal timing of peak uplift in the displacement time series, which suggests a peak in pore pressure related to a relative maximum in hydraulic head (*Poland and Davis*, 1969; *Terzaghi*, 1925), generally occurs later than the seasonal peak in GWL. This is consistent with the idea that there is a delay in aquitard drainage as it responds to drops in hydraulic head, modulating the timing of deformation (*Liu et al.*, 2019; *Ojha et al.*, 2019; *Smith et al.*, 2017). This appears particularly true for locations where both the deformation and groundwater records exhibit regular seasonal oscillations (e.g., Figure 4.9).

The broad agreement between the gridded time series and original well records demonstrates the potential utility of this publicly available dataset for characterizing GWL across the valley. However, further refinement is needed to confidently approximate the groundwater surface elevation. A potential avenue for this refinement would include a detailed assessment of which time periods the surface fitting was unconstrained for each time series. This would provide insight into the robustness of the seasonal modelling. As the surface fitting technique is conducted independently for each month and GWL sampling is not uniform across time and space due to some months having a dearth of data leading to inaccurate estimates (e.g., Figure 4.12). In lieu of increased

well sampling, which would only affect future GWL approximations, the application of a temporal smoother may improve the agreement between the gridded GWL estimates and individual well records.

4.3.2 GWL and Displacement Change Rates

The vertical displacement rates (v in equation 4.1) indicate broad regions of subsidence over the San Joaquin Valley (Figure 4.2), consistent with previous geodetic studies (*Chaussard and Farr*, 2019; *Murray and Lohman*, 2018; *Neely et al.*, 2021; *Ojha et al.*, 2018, 2019). Subsidence rates during dry years (WY2016 and WY2018) exceeded 300 mm/yr. Canonically, this agrees with what is expected for poroelastic deformation where in a dry year there is typically more groundwater extraction (i.e., a greater reduction in hydraulic head) and thus a larger decline in pore pressure resulting in compaction of the aquifer system (*Poland and Davis*, 1969; *Leake*, 1990). Despite a recovery from drought conditions during WY2017 and WY2019, these "wet" years still exhibit subsidence signals of ~ 150 mm/yr. While diminished compared to the dry years, this sinking of the land surface under wetter conditions is relatively large compared to other regions globally experience groundwater related subsidence (*Bagheri-Gavkosh et al.*, 2021). This is due in part to the San Joaquin Valley's continued reliance on groundwater even in non-drought years (*Faunt et al.*, 2016) and potentially related to the deferred subsidence associated with the dewatering of clay and silt packages which can occur on time scales of years to decades (*Liu et al.*, 2019; *Ojha et al.*, 2019; *Smith et al.*, 2017). Interesting, in both wet years, a large uplift is observed on the western side of the San Joaquin Valley

where the Westlands Water District is located. This region has historically experienced land surface rebound (*Ireland et al.*, 1984) and *Neely et al.* (2021) identified this feature previously as well in WY2017. This uplift may be combination of groundwater recharge, expansion of clay and silt packages near the surface, and/or poor drainage related to a perched water table (*San Joaquin Valley Drainage Program*, 1990).

Seasonal amplitude (A in equation 4.1) maps of displacement over the valley suggest the magnitude and regions of cyclic change in GWL. Following poroelastic theory, larger amplitude values indicate larger seasonal changes in hydraulic head. In all years, we observe amplitudes exceeding 35 mm (Figure 4.2). The years with the largest displacement amplitude values (WY2016 and WY2017) are also the years with the greatest extremes in surface water availability. WY2016 was preceded by 4 years of intense drought (*Lund et al.*, 2018) and WY2017 had well above average precipitation, Sierra Nevada snow pack, and river runoff ($\sim$164%, 163%, and 217% of average respectively) (*California Department of Water Resources*, 2021). *Neely et al.* (2021) noted that the spatial patterns of amplitude do not correspond directly to the vertical displacement rates and that the higher amplitude regions during WY2016 are typically associated further upstream along river courses than the high amplitude regions in WY2017 which appear closer to the confluence of rivers. These patterns appear to hold true for the relatively dry and wet years of WY2018 and WY2019, albeit muted.

The seasonal phase (T in equation 4.1) of displacement, or timing of peak seasonal uplift, is assumed to be related to the timing of peak hydraulic head at that location (*Poland and Davis*, 1969). For both dry years, the greater part of the valley has seasonal

uplift during winter and early spring (January to April). As the maximum in surface water availability occurs during this time, though limited, and this timing is roughly half a year out of phase with the expected minimum in GWLs following a summer of persistent groundwater withdrawals, these maps are consistent with our expectation of water use in the valley. For both wet years, we observe peak seasonal uplift occurring in winter and early spring (January to April) along the eastern valley margin. Moving from the valley margin towards the valley axis, this timing occurs progressively later into the year. For WY2019, this timing is not as extended as for WY2017. While we consider WY2019 as a "wet" year, conditions were subdued compared to WY2017 and thus may reflect a seasonal uplift timing spatial behavior that is in between the extremes of the dry years and WY2017.

Neely et al. (2021) suggested that individual water years with similar hydrological conditions (e.g. dry vs. dry or wet vs. wet years) may result in a similar spatial and temporal evolution of surface displacements. Results here appear to support that idea with WY2016 and WY2018 exhibiting mirrored behavior of each other and WY2017 and WY2019 are likewise similar (though WY2019 displaying seasonal parameters somewhere in between wet and dry years). Given that California receives a majority of its precipitation early in the year (*Williamson et al.*, 1989; *California Department of Water Resources*, 2021), the spatio-temporal progression of surface displacements and associated groundwater resources may be predictable. This has implications for which regions should receive prioritization for critical planning decisions such as surface water diversions, resource and infrastructure monitoring, and/or even crop selection.

Despite a general agreement between the gridded GWL approximations and in-situ GWL observations, estimates of the linear rate of GWL change and seasonal parameters are noisy and contain artifacts from the surface fitting procedure (Figures 4.3-4.8). Further, we were unable to produce results when using only deep wells (wells perforated at depths below ∼120 m) due to a sparsity in data coverage. While we were able to produce results for the shallow aquifer, we will focus on results that did not discriminate based on depth unless otherwise specified. Notably, the most northern section of the valley exhibits a gradient in the rate and amplitude with increasing magnitude of "signal" towards the valley boundary in 7 of the 10 years. This is a region that frequently loses data coverage (e.g., Figure 4.12) such that it is unconstrained and promotes extreme edge effects. This phenomenon is also evident along the southwest margin of the valley were the land is mostly native and unmonitored. The region with the most consistent network of GWL observations lies between 37° and 39° latitude. Coincidentally, this is a region that experiences very little surface deformation and seasonal effects (*Jasechko and Perrone*, 2020; *Ojha et al.*, 2018). For regions with low amplitude seasonal signals, caution should be used when assessing the seasonal phase fits as they can effectively be random (evidenced here in the form of spatial discontinuities). Curiously, many of our dry years exhibit increases in GWL when we expected to approximate large GWL declines (e.g. WY2016 in Figure 4.5). Potentially, the rate of GWL change and seasonal parameters are likely biased towards wells sampling the shallow aquifer. As groundwater is typically extracted from the deeper aquifer system to irrigate crops due to its higher water quality, some of this water may enter the shallower aquifer system (*Scanlon et al.*,

2005) which in turn may suggest increases in groundwater level for our results.

4.3.3 EOF Analysis

Figure 4.13 shows the EOF analysis on the surface displacement data by year. Here we focus on the first 4 components as they explain ∼90% of the variance. The first component for each year mirrors the long-term deformation rate which explains ∼46-67% of the variance and have monotonically decreasing temporal functions. While we only have 4 years of data (2 dry and 2 wet), more variance, on average, is explained in the first component for the dry years than the wet years (∼58% vs. ∼49%). The second component explains ∼10-26% of the variance with the most prominent spatial patterns occuring in the EOF amplitude maps for WY2017 and WY2019. These features are similar to the regions of observed uplift in the rate of deformation maps near Westlands Water District. Regions of high seasonal amplitude (observed in Figure 4.2) are also highlighted here. The third and fourth components, which explain ∼5-15% and ∼4% of the variance respectively, show the additional regions of higher seasonal amplitude that were not fully captured in the second component. The temporal functions for the third and fourth components exhibit seasonality, potentially reflecting groundwater pumping activities and aquifer recharge processes.

Spatial patterns in this analysis are in general agreement with a previous signal decomposition study (*Chaussard and Farr*, 2019) although they focused on the full time series record rather than investigate on an annual basis. Conceptually, the higher explained variance in the first component during dry years is consistent if we expect there

to be more persistent pumping and less seasonal recharge. This analysis demonstrates the complexity of surface deformation in the San Joaquin Valley.

Figures 4.14-4.19 show the EOF analyses on the gridded GWL by year. Similar to the displacement EOF analysis, we focus on the first 4 components which explain ∼85-90% of the variance. The first component for each year, which explain ∼41-69% of the variance, all exhibit similar spatial patterns. When combined with the temporal functions, these results suggest increases in GWL around the valley margins and GWL declines in the valley interior. Contrary to our rate of GWL change results (Figures 4.3-4.8), the first components of the EOF analyses generally follow our expectations of GWL storage changes in the San Joaquin Valley. Further, the mean variance explained by the first component, when partitioned into wet (WY2010, WY2011, WY2017, and WY2019) and dry (WY2012-2016 and WY20018) periods, broadly agree with results from the displacement EOF analysis in the sense that more importance placed on this component during dry years than in wet years (∼57% compared to ∼52%). However, we observe GWL declines in the region spanning 37° to 39° latitude that we do not expect. As this region is the most consistent in terms of sampling, in addition to our and others (*Jasechko and Perrone*, 2020; *Ojha et al.*, 2018) results indicating little GWL change, this signal in the EOF is confounding which may warrant further investigation.

The second, third, and fourth components explain ∼10-31%, ∼5-17%, and ∼4-6% of the variance respectively. Interpreting these higher order components are challenging as spatial structure often appear biased due to the surface fitting process and the temporal functions oscillate dramatically in a non-physical manner. Additionally, EOF

analyses on gridded GWL products only using shallow wells (Figures 4.17-4.19) also appear to be dominated by artifacts from the surface fitting procedure. As noted previously, the application of a temporal smoother may elucidate meaningful structure that we could relate to physical processes.

4.4 Summary

The utilization of groundwater is a vital component for California water use, especially in the Central Valley. During periods of limited surface water availability, we expect groundwater level (GWL) declines in response to increased reliance. Under wetter conditions, GWL should rebound or remain somewhat stable. Recent and persistent droughts have threatened these resources and motivated legislation to ensure their future vitality. However, directly observing the state of these aquifer systems remains challenging. While monitoring wells have and will continue to play a critical role in the characterization of groundwater resources, there is currently no means to efficiently map changes in the water table at spatial and temporal resolutions sufficient for regional management and policy decisions.

Here, we investigated the utility of DWR's periodic groundwater level database for synoptically mapping GWL across California's Central Valley at monthly intervals between 2009 and 2019. Despite our gridded GWL product broadly agreeing with individual monitoring well time series, it is insufficient for describing spatial patterns, magnitude, and/or timing of GWL changes due to a sparsity of data. A time series

decomposition in the form of an empirical orthogonal function analysis showed some promise for estimating GWL behavior in the first component, but contained confounding signal and artifacts from the surface fitting procedure.

Additionally, we investigated 4 years of surface displacement from a joint GPS-InSAR analysis. We observed large subsidence signals consistent with previous studies and interestingly found that deformation patterns and timing are comparable for years with similar hydrological conditions (dry vs. dry or wet vs. wet). While changes in displacement time series do not strictly map to GWL changes in an one-to-one fashion, this is an early step for predicting how groundwater resources may respond given knowledge of projected water availability and has implications for groundwater management and policy development.

Acknowledgements

Chapter 4 is an active research project currently being prepared for publication, and is coauthored with Farhood Ensan and Adrian Borsa. I was the primary investigator and author of this research material.

This work was funded by NASA under Grant NNX16AR07G (Science Team for the NISAR Mission) and Grant 80NSSC18K1422 (NASA Earth and Space Science Fellowship). All raw geodetic and hydrological data are freely available from public sources (as referenced).

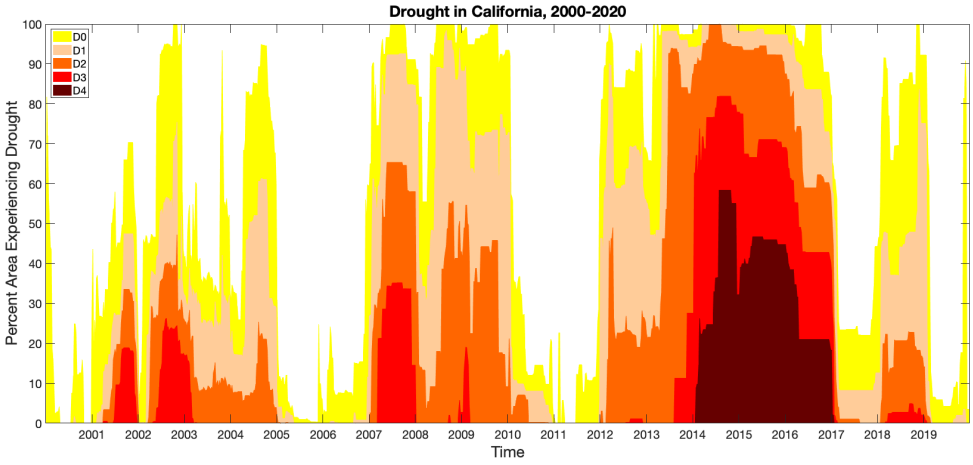

Figure 4.1: Percent area and severity of California in drought between 2000-2020. Drought conditions are broken into 5 categories: D0 abnormally dry (yellow), D1 moderate drought (peach), D2 severe drought (orange), D3 extreme drought (red), D4 exceptional drought (maroon). Image recreated using U.S. Drought Monitor data from the National Integrated Drought Information System (https://www.drought.gov/states/california).

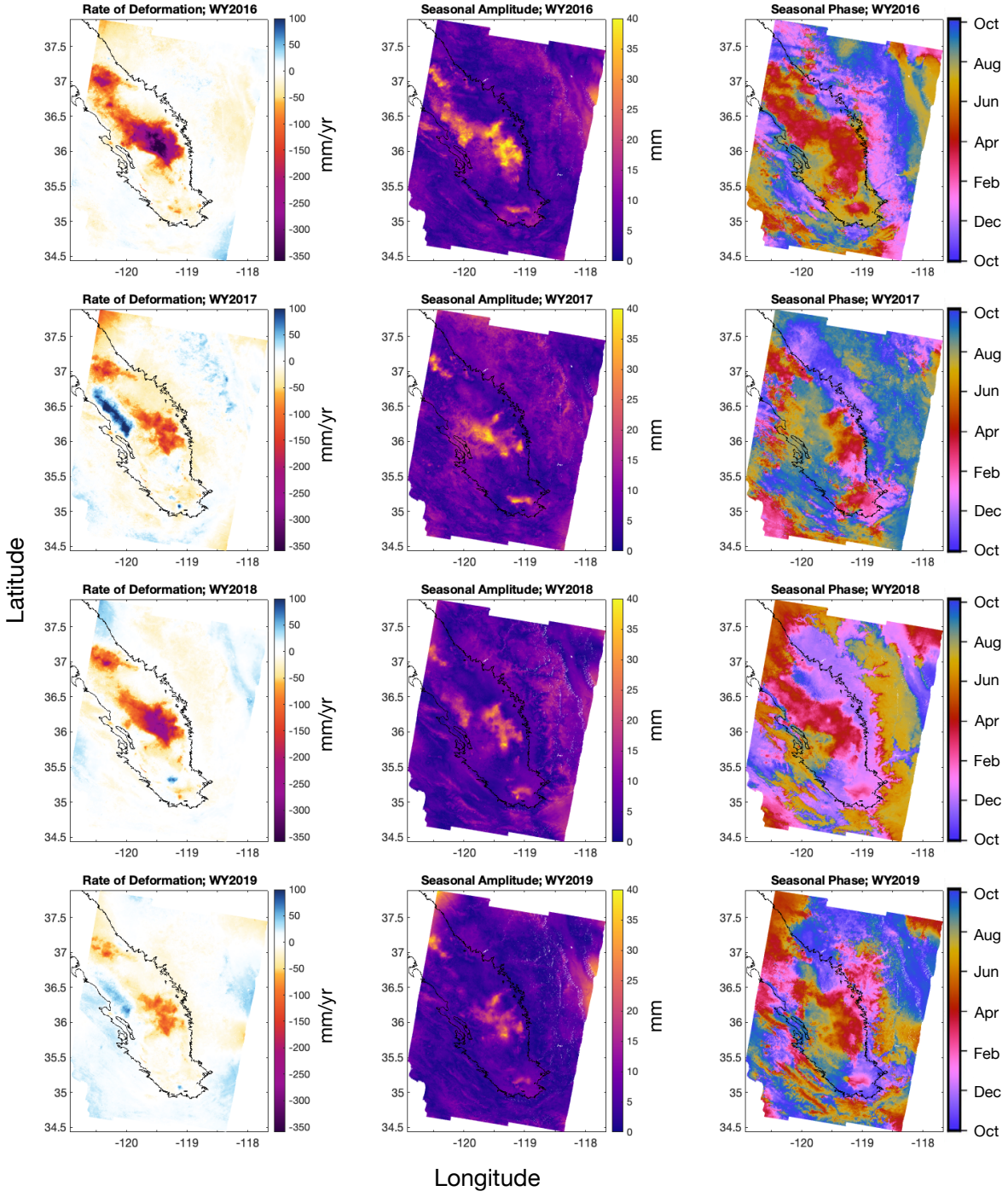

Figure 4.2: Annual vertical displacement rates (mm/yr), seasonal amplitudes (mm), and seasonal uplift timing over the San Joaquin Valley for water years 2016 to 2019. Displacement time series are estimated using Sentinel-1 data and the GInSAR method. Rates of deformation and seasonal parameters are modeled using equation 4.1. The alluvial boundary of the Central Valley distinguished by the black outline.

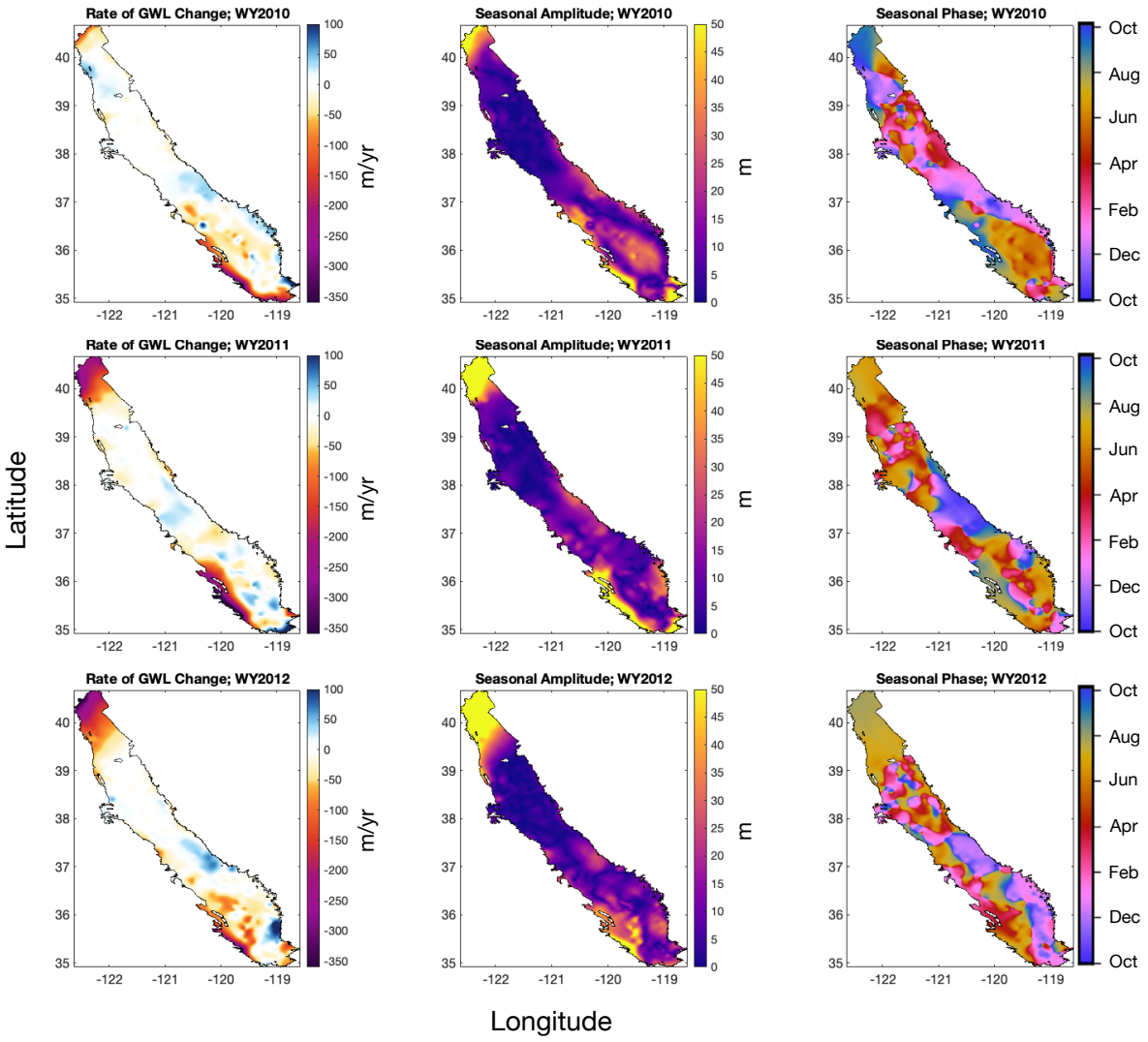

Figure 4.3: Annual rates of groundwater (GWL) change (m/yr), seasonal amplitudes (m), and seasonal timing of peak GWL over the Central Valley for water years 2010 to 2012 using the gridded GWL time series.

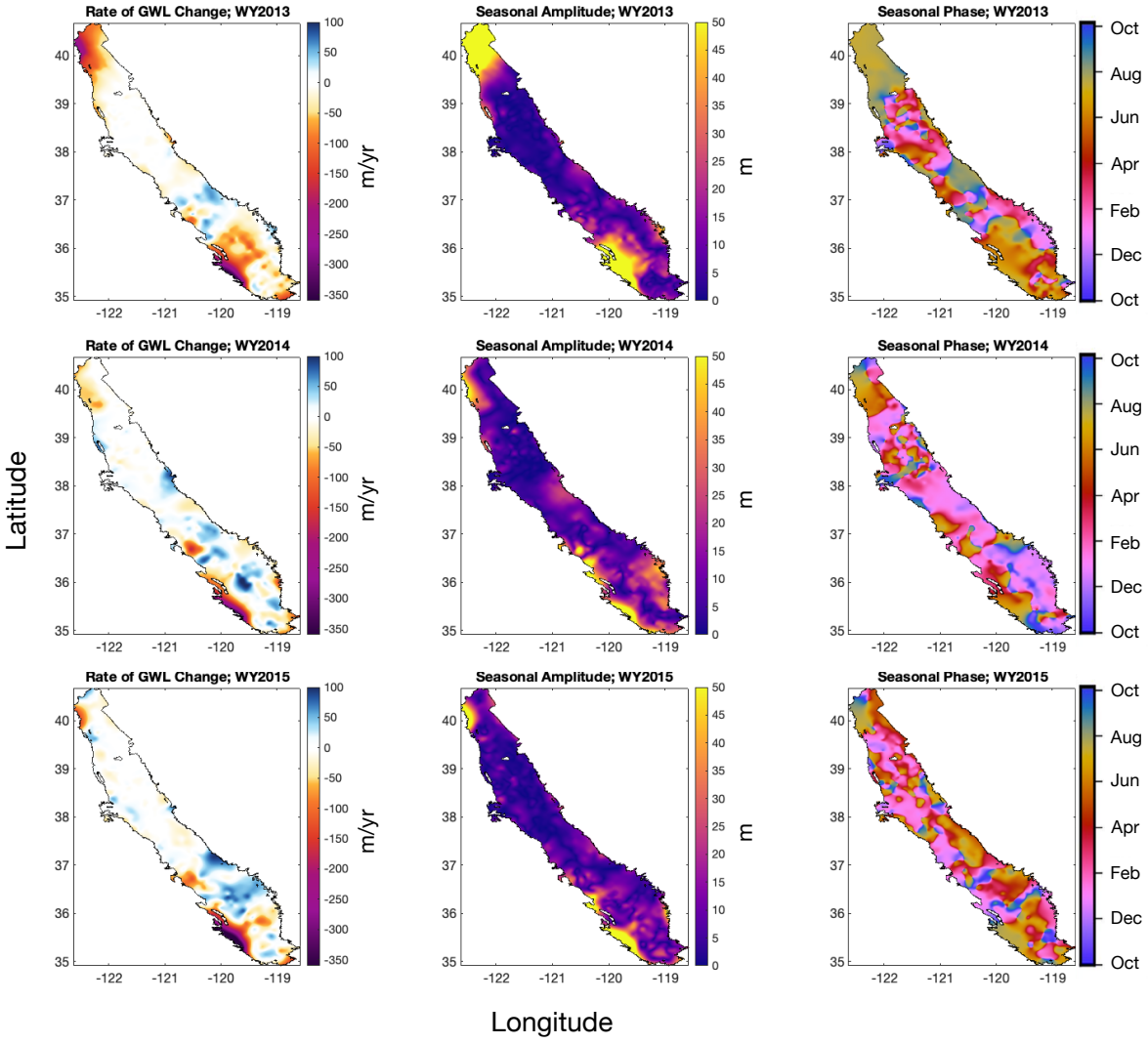

Figure 4.4: Annual rates of groundwater (GWL) change (m/yr), seasonal amplitudes (m), and seasonal timing of peak GWL over the Central Valley for water years 2010 to 2015 using the gridded GWL time series.

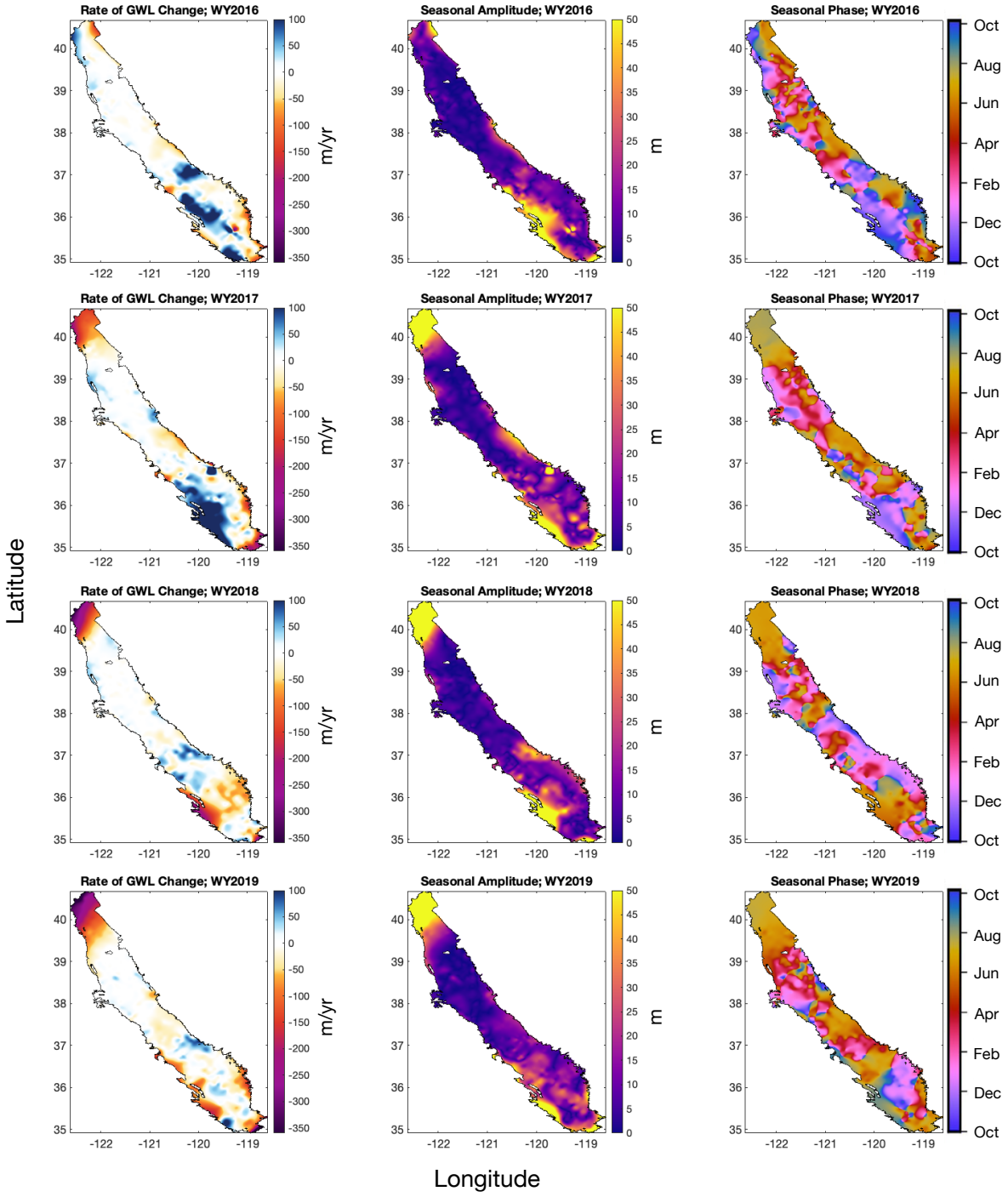

Figure 4.5: Annual rates of groundwater (GWL) change (m/yr), seasonal amplitudes (m), and seasonal timing of peak GWL over the Central Valley for water years 2016 to 2019 using the gridded GWL time series.

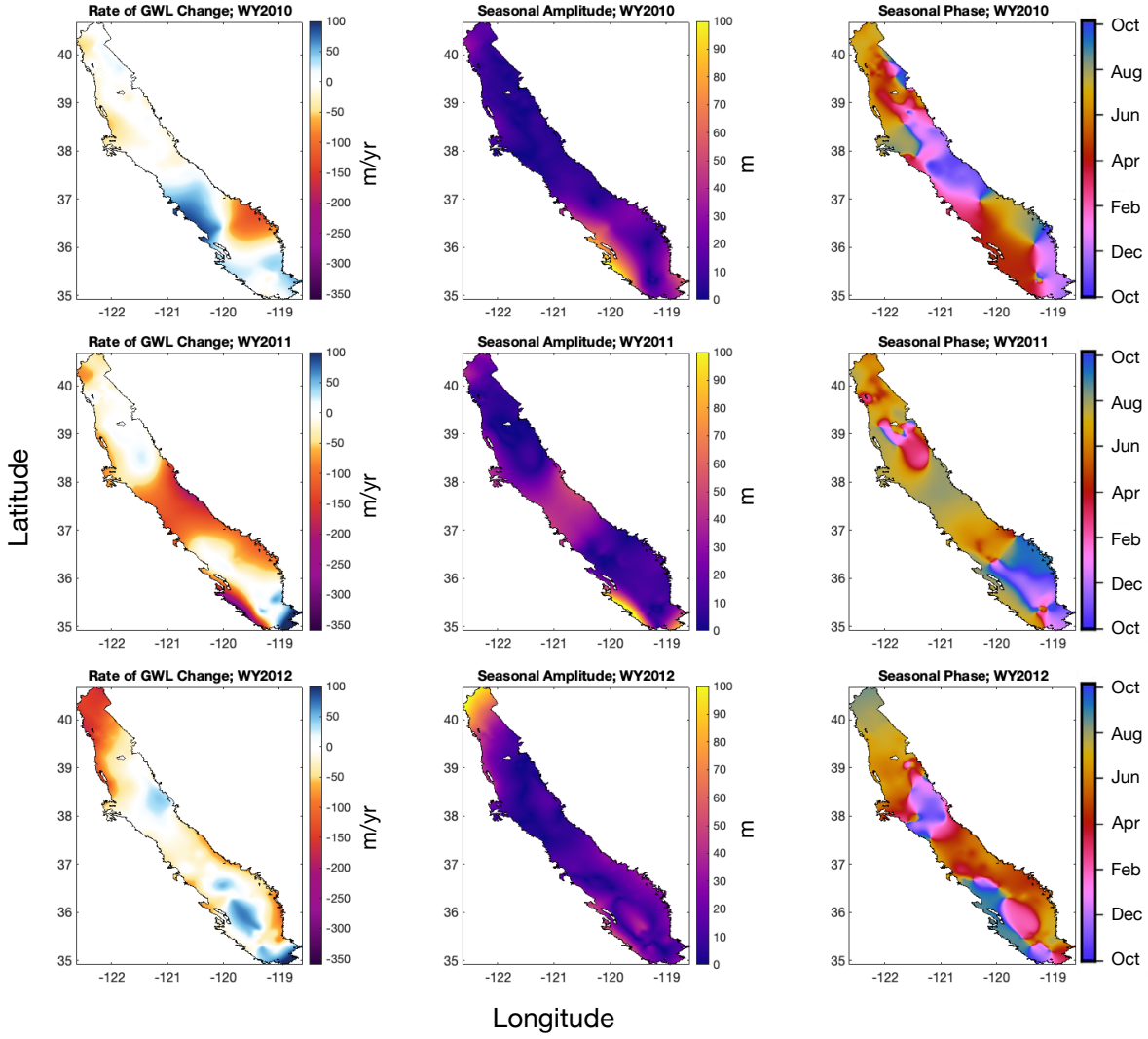

Figure 4.6: Annual rates of groundwater (GWL) change (m/yr), seasonal amplitudes (m), and seasonal timing of peak GWL over the Central Valley for water years 2010 to 2012 using the shallow gridded GWL time series.

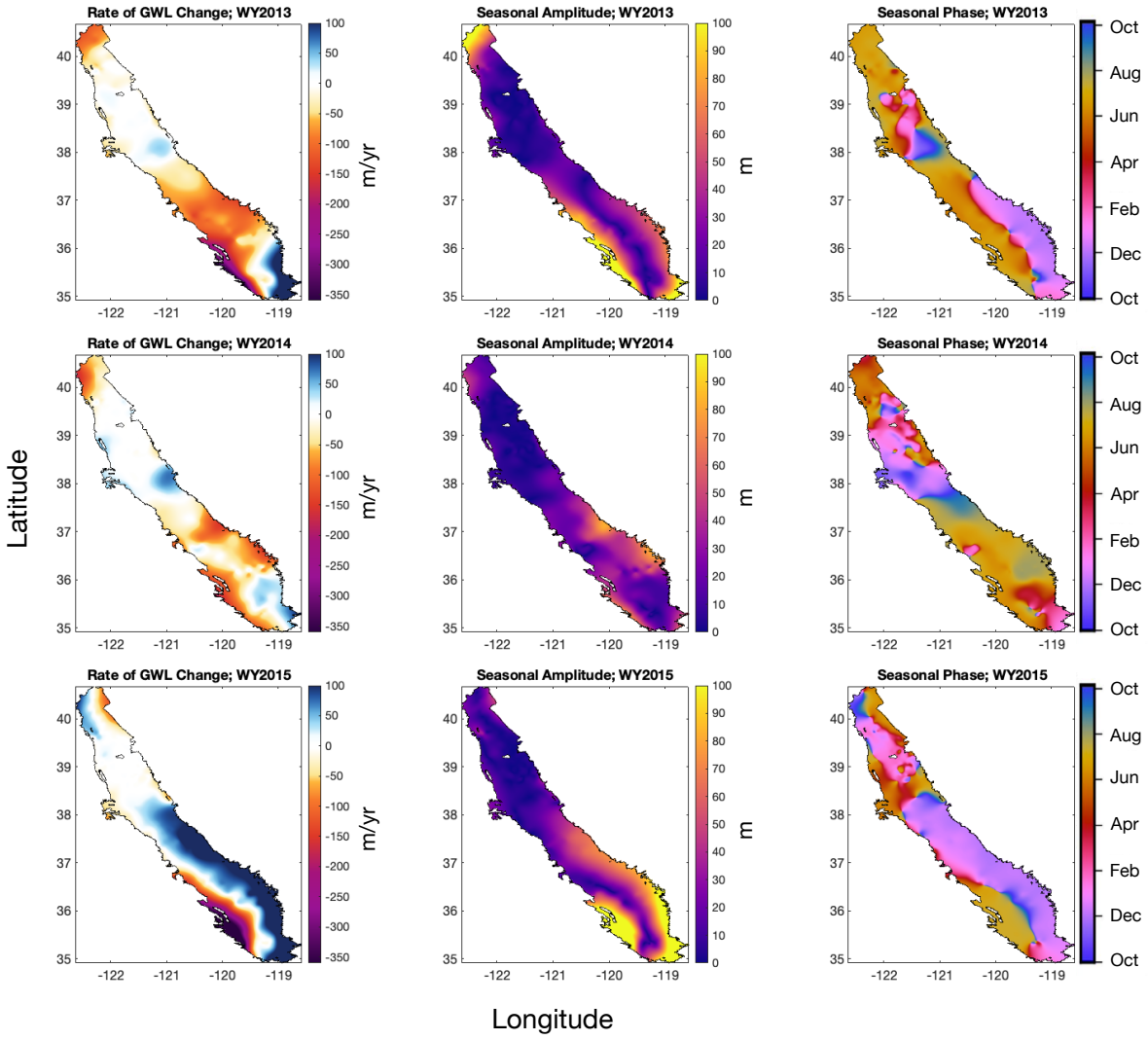

Figure 4.7: Annual rates of groundwater (GWL) change (m/yr), seasonal amplitudes (m), and seasonal timing of peak GWL over the Central Valley for water years 2010 to 2015 using the shallow gridded GWL time series.

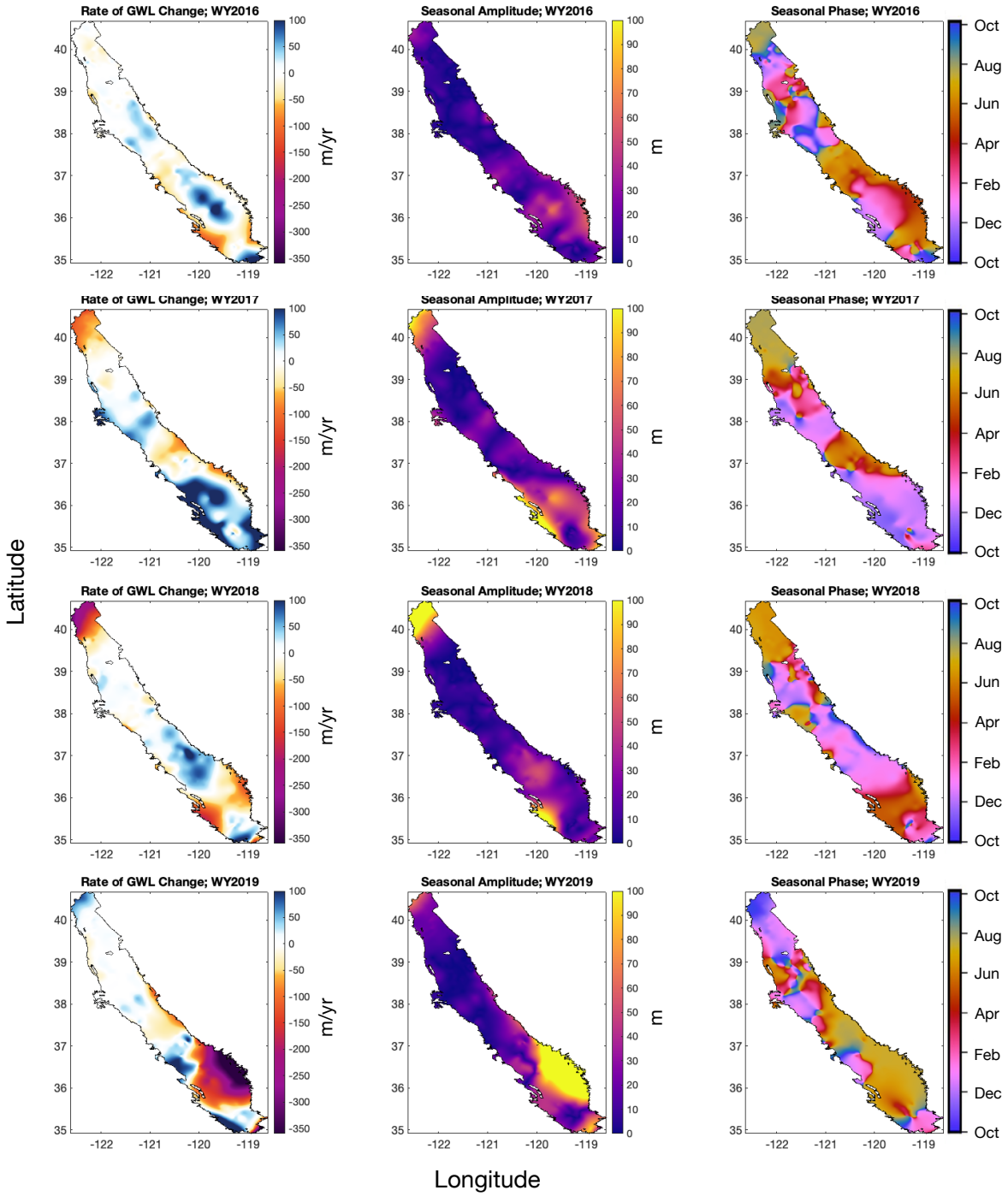

Figure 4.8: Annual rates of groundwater (GWL) change (m/yr), seasonal amplitudes (m), and seasonal timing of peak GWL over the Central Valley for water years 2016 to 2019 using the shallow gridded GWL time series.

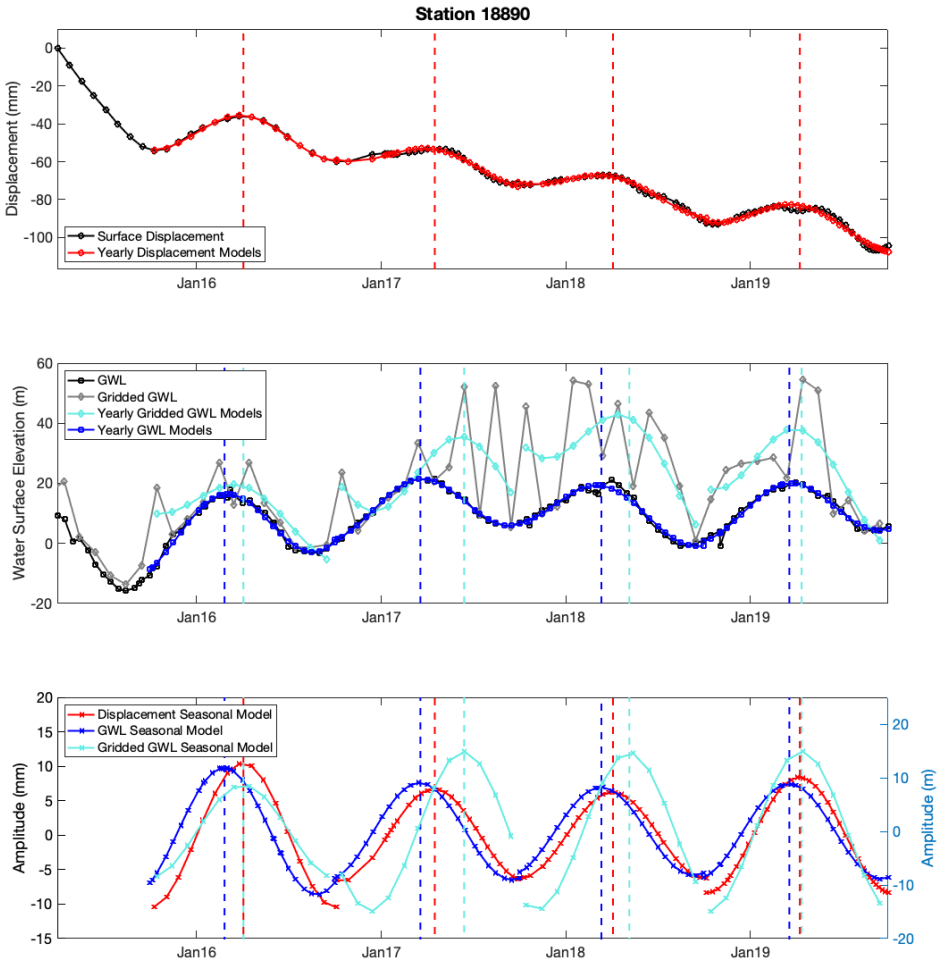

Figure 4.9: Comparison of surface displacements, gridded groundwater levels (GWL), and *in-situ* groundwater levels at monitoring well 18890. The top panel shows the surface displacement from GPS-enhanced InSAR (black with circle symbols), the yearly models of displacement using equation 4.1 (red with circle symbols), and the timing of peak seasonal uplift estimated by the models (vertical dashed red lines). The middle panel shows the gridded GWL (gray with diamond symbols), the yearly models of gridded GWL using equation 4.1 (cyan with diamond symbols), the timing of peak seasonal gridded GWL estimated by the models (vertical dashed cyan lines), the GWL at station 18890 (black with square symbols), the yearly models of GWL using equation 4.1 (blue with square symbols), and the timing of peak seasonal GWL estimated by the models (vertical dashed blue lines). The bottom panel shows the detrended seasonal models and timing of peak seasonal signals for displacement, gridded GWL, and GWL at station 18890 (red, cyan, and blue respectively).

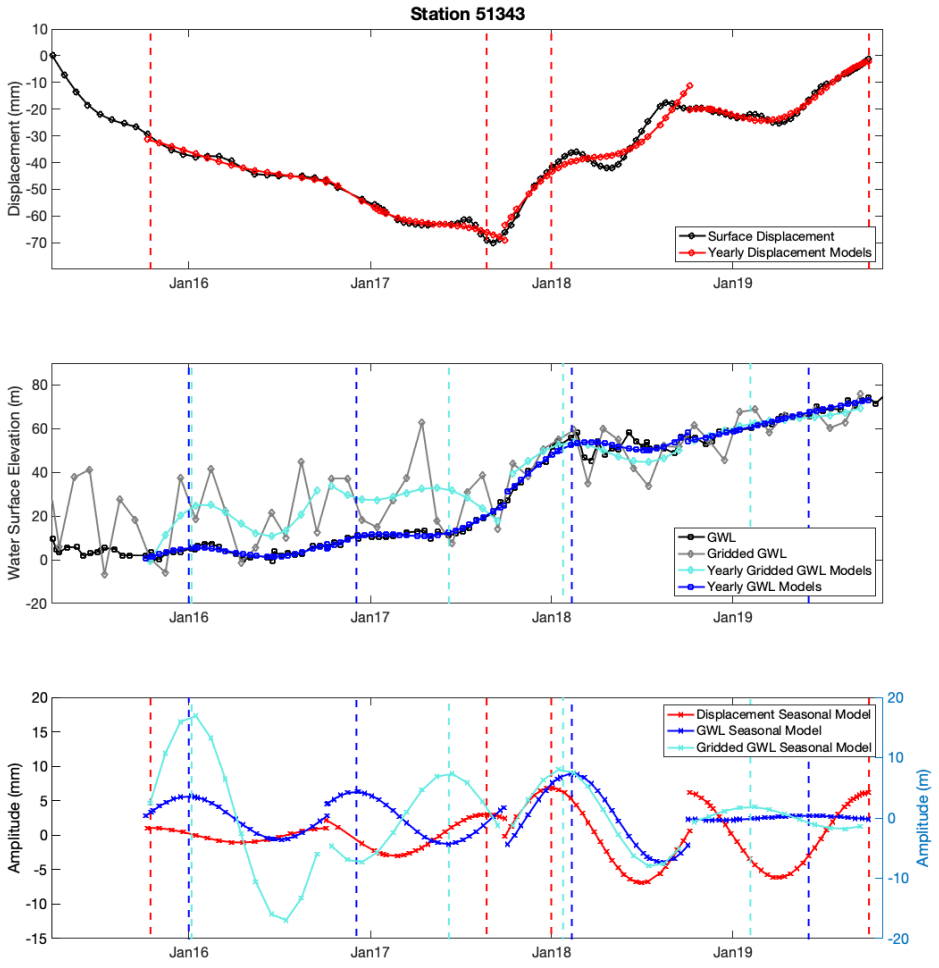

Figure 4.10: Comparison of surface displacements, gridded groundwater levels (GWL), and *in-situ* groundwater levels at monitoring well 51343. The top panel shows the surface displacement from GPS-enhanced InSAR (black with circle symbols), the yearly models of displacement using equation 4.1 (red with circle symbols), and the timing of peak seasonal uplift estimated by the models (vertical dashed red lines). The middle panel shows the gridded GWL (gray with diamond symbols), the yearly models of gridded GWL using equation 4.1 (cyan with diamond symbols), the timing of peak seasonal gridded GWL estimated by the models (vertical dashed cyan lines), the GWL at station 51343 (black with square symbols), the yearly models of GWL using equation 4.1 (blue with square symbols), and the timing of peak seasonal GWL estimated by the models (vertical dashed blue lines). The bottom panel shows the detrended seasonal models and timing of peak seasonal signals for displacement, gridded GWL, and GWL at station 51343 (red, cyan, and blue respectively).

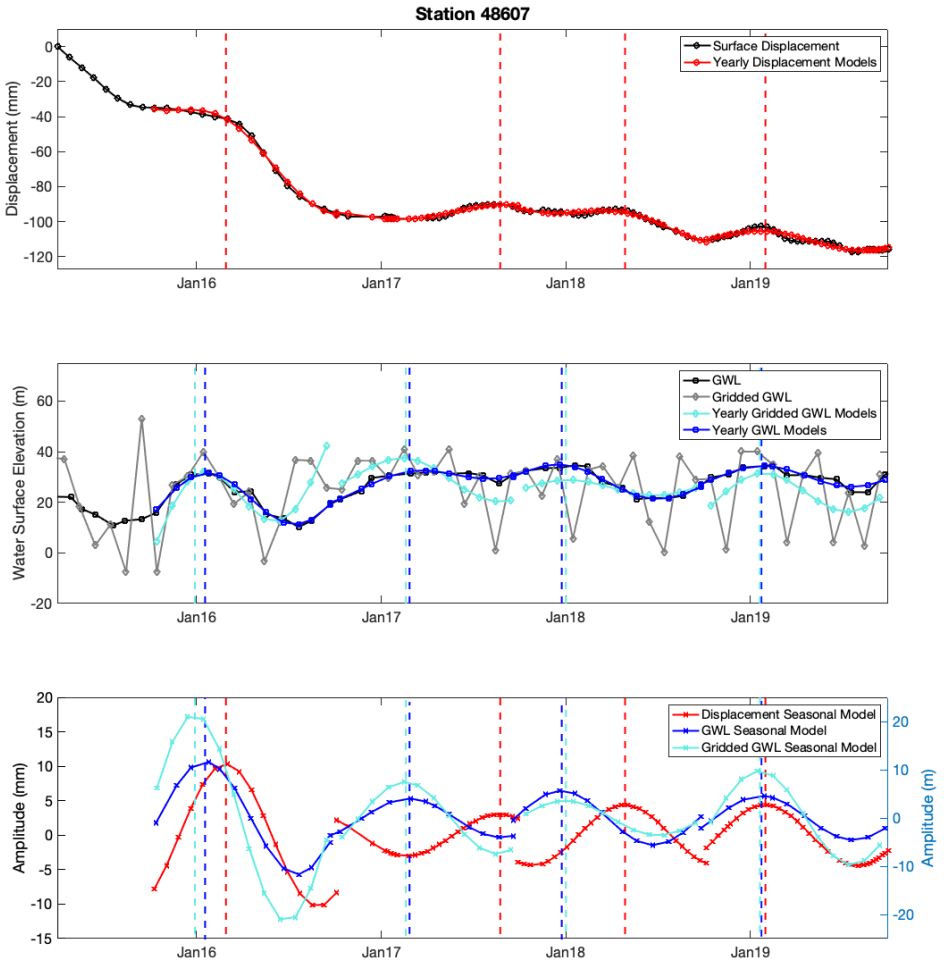

Figure 4.11: Comparison of surface displacements, gridded groundwater levels (GWL), and *in-situ* groundwater levels at monitoring well 48607. The top panel shows the surface displacement from GPS-enhanced InSAR (black with circle symbols), the yearly models of displacement using equation 4.1 (red with circle symbols), and the timing of peak seasonal uplift estimated by the models (vertical dashed red lines). The middle panel shows the gridded GWL (gray with diamond symbols), the yearly models of gridded GWL using equation 4.1 (cyan with diamond symbols), the timing of peak seasonal gridded GWL estimated by the models (vertical dashed cyan lines), the GWL at station 48607 (black with square symbols), the yearly models of GWL using equation 4.1 (blue with square symbols), and the timing of peak seasonal GWL estimated by the models (vertical dashed blue lines). The bottom panel shows the detrended seasonal models and timing of peak seasonal signals for displacement, gridded GWL, and GWL at station 48607 (red, cyan, and blue respectively).

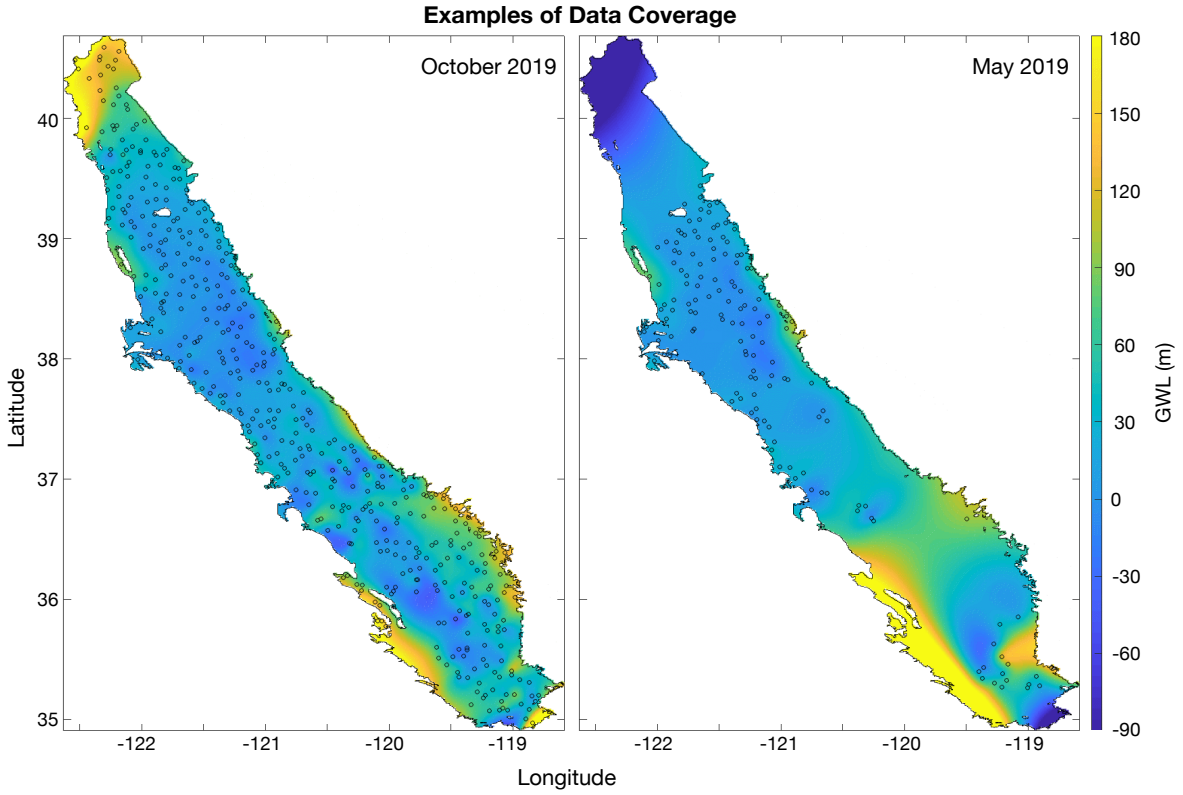

Figure 4.12: Examples of station coverage used during the surface fitting procedure. The left panel is an example of a month with higher data coverage (October 2019). The right panel is an example of a month with lower data coverage (May 2019). The groundwater level (GWL) surfaces estimated from "gridit" using the available stations (black circles) are displayed for each month.

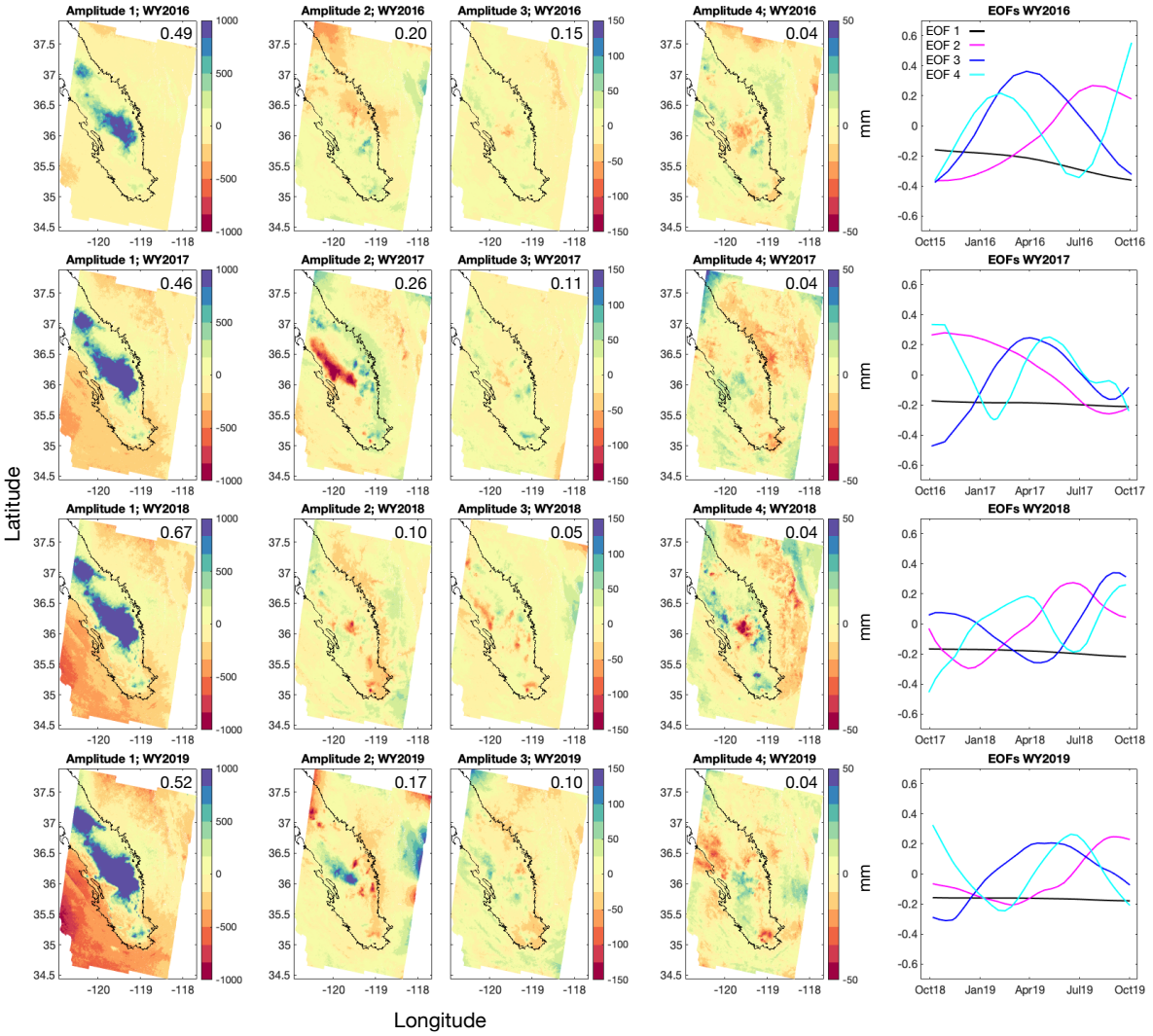

Figure 4.13: Spatial amplitude maps and temporal behavior of surface displacements as estimated using empirical orthogonal function (EOF) analysis for each water year (WY2016-WY2019). Input displacement time series are estimated using Sentinel-1 data and the GInSAR method. Rows of panels correspond to a particular water year. The first four columns of panels correspond to the first four components estimated during the EOF analysis. The values in the top right of each panel is the fractional variance each component explains. The panels in the last column are the temporal functions associated with each component.

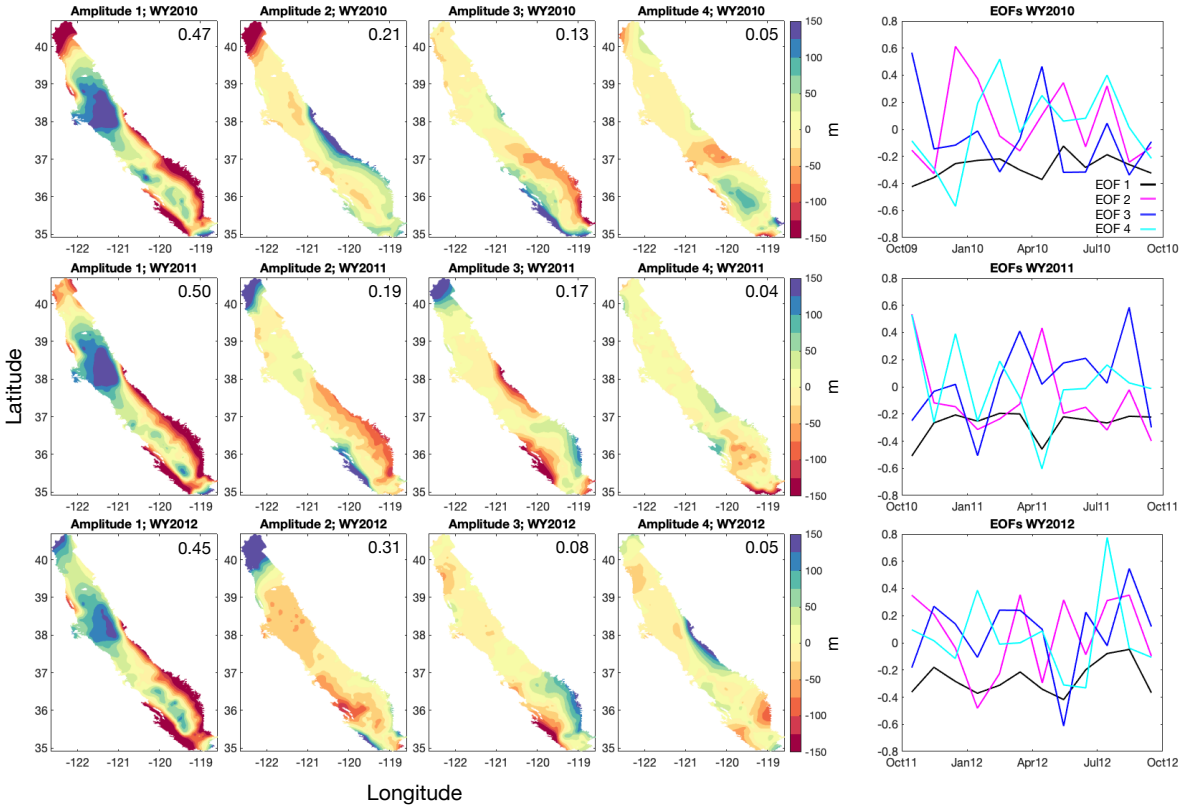

Figure 4.14: Spatial amplitude maps and temporal behavior of gridded GWL as estimated using empirical orthogonal function (EOF) analysis for each water year (WY2010-WY2012). Rows of panels correspond to a particular water year. The first four columns of panels correspond to the first four components estimated during the EOF analysis. The values in the top right of each panel is the fractional variance each component explains. The panels in the last column are the temporal functions associated with each component.

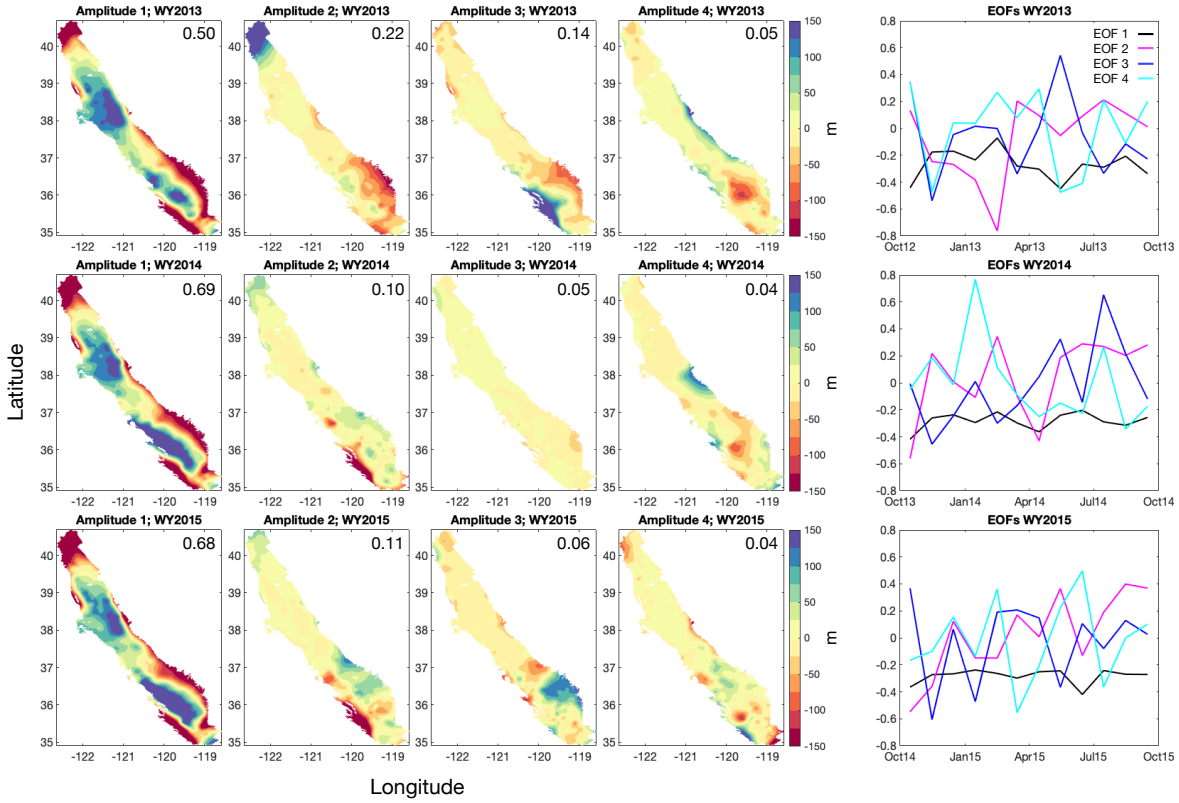

Figure 4.15: Spatial amplitude maps and temporal behavior of gridded GWL as estimated using empirical orthogonal function (EOF) analysis for each water year (WY2013-WY2015). Rows of panels correspond to a particular water year. The first four columns of panels correspond to the first four components estimated during the EOF analysis. The values in the top right of each panel is the fractional variance each component explains. The panels in the last column are the temporal functions associated with each component.

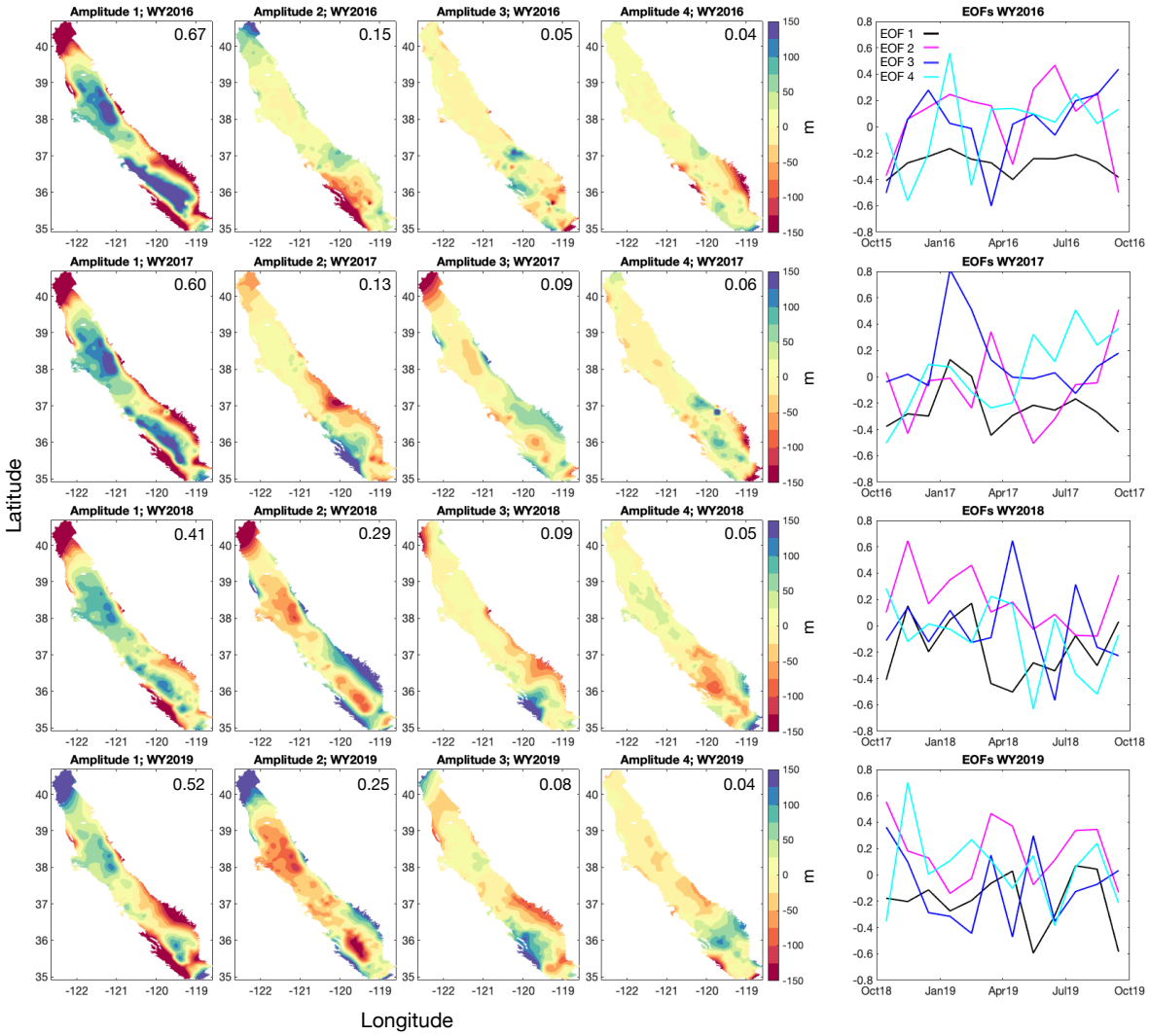

Figure 4.16: Spatial amplitude maps and temporal behavior of gridded GWL as estimated using empirical orthogonal function (EOF) analysis for each water year (WY2016-WY2019). Rows of panels correspond to a particular water year. The first four columns of panels correspond to the first four components estimated during the EOF analysis. The values in the top right of each panel is the fractional variance each component explains. The panels in the last column are the temporal functions associated with each component.

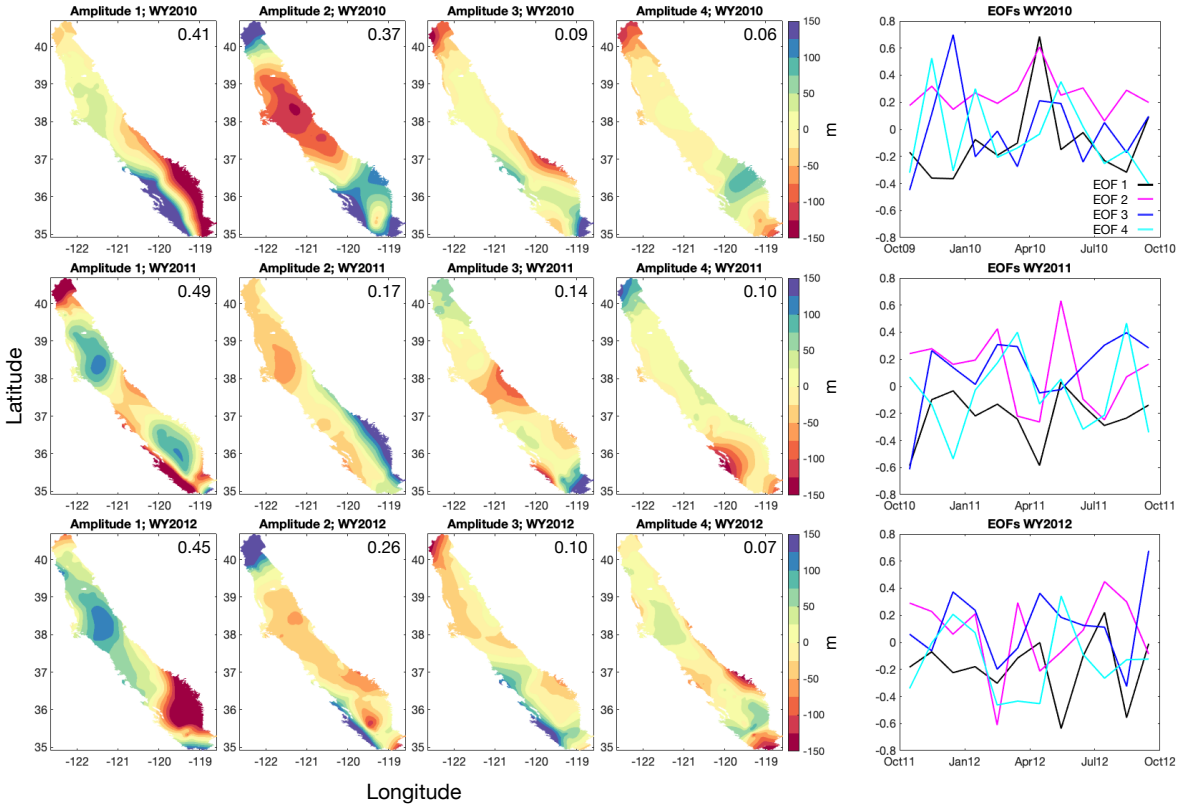

Figure 4.17: Spatial amplitude maps and temporal behavior of gridded GWL using "shallow" wells as estimated using empirical orthogonal function (EOF) analysis for each water year (WY2010-WY2012). Rows of panels correspond to a particular water year. The first four columns of panels correspond to the first four components estimated during the EOF analysis. The values in the top right of each panel is the fractional variance each component explains. The panels in the last column are the temporal functions associated with each component.

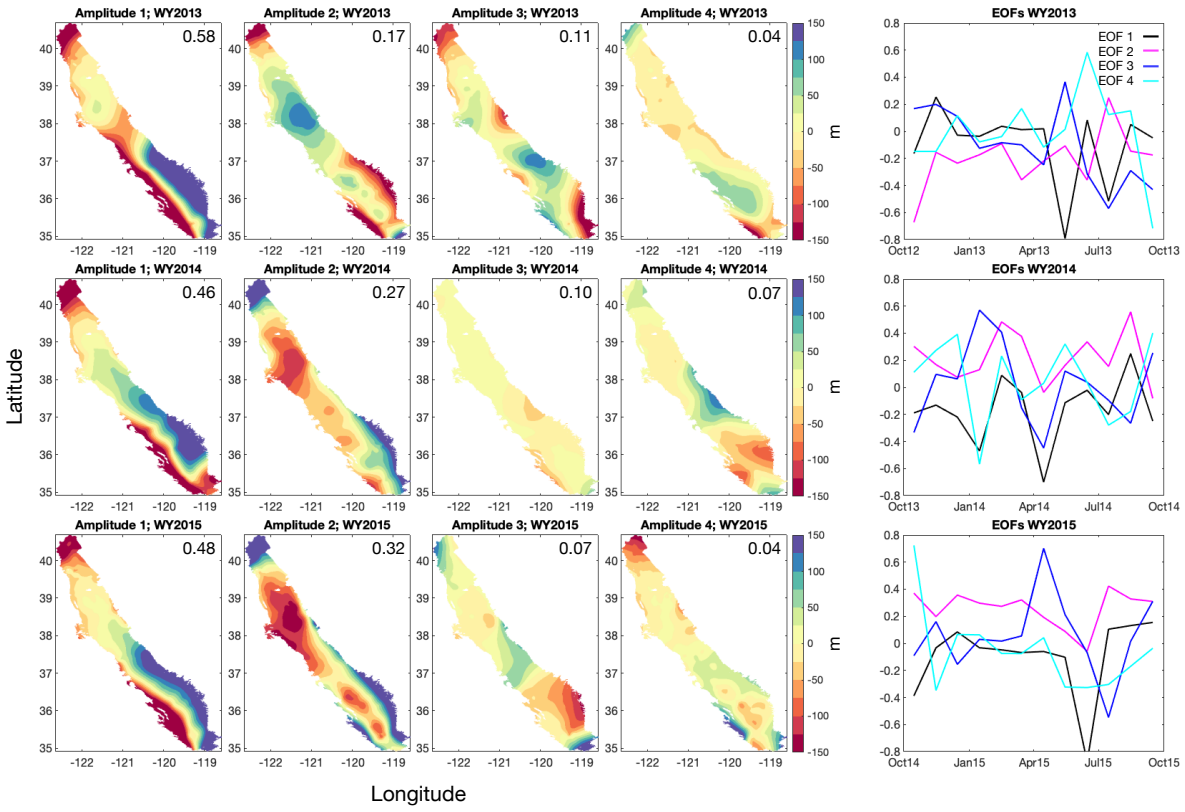

Figure 4.18: Spatial amplitude maps and temporal behavior of gridded GWL using "shallow" wells as estimated using empirical orthogonal function (EOF) analysis for each water year (WY2013-WY2015). Rows of panels correspond to a particular water year. The first four columns of panels correspond to the first four components estimated during the EOF analysis. The values in the top right of each panel is the fractional variance each component explains. The panels in the last column are the temporal functions associated with each component.

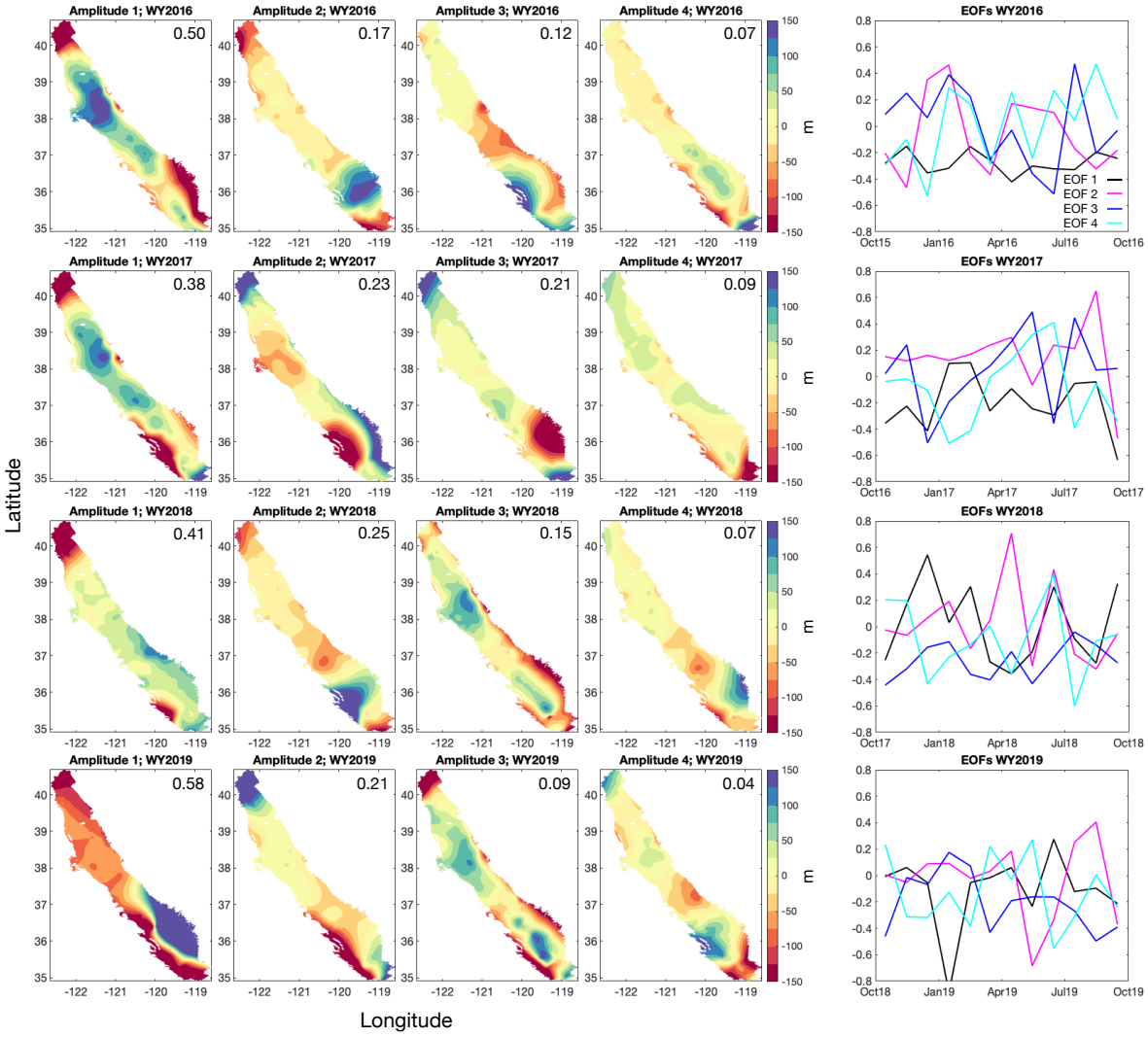

Figure 4.19: Spatial amplitude maps and temporal behavior of gridded GWL using "shallow" wells as estimated using empirical orthogonal function (EOF) analysis for each water year (WY2016-WY2019). Rows of panels correspond to a particular water year. The first four columns of panels correspond to the first four components estimated during the EOF analysis. The values in the top right of each panel is the fractional variance each component explains. The panels in the last column are the temporal functions associated with each component.

References

Abdi, H., and L. J. Williams (2010), Principal component analysis, *WIREs Computational Statistics*, *2*(4), 433–459, doi:10.1002/wics.101.

Bagheri-Gavkosh, M., S. M. Hosseini, B. Ataie-Ashtiani, Y. Sohani, H. Ebrahimian, F. Morovat, and S. Ashrafi (2021), Land subsidence: A global challenge, *Science of The Total Environment*, *778*, 146,193, doi:10.1016/j.scitotenv.2021.146193.

Berardino, P., G. Fornaro, R. Lanari, and E. Sansosti (2002), A new algorithm for surface deformation monitoring based on small baseline differential SAR interferograms, *IEEE Transactions on Geoscience and Remote Sensing*, *40*(11), 2375–2383, doi:10.1109/TGRS.2002.803792.

Borsa, A. A., J.-B. Minster, B. G. Bills, and H. A. Fricker (2007), Modeling long-period noise in kinematic GPS applications, *Journal of Geodesy*, *81*(2), 157–170, doi:10.1007/s00190-006-0097-x.

California Department of Water Resources (2021), Bulletin 132.

Chaussard, E., and T. G. Farr (2019), A New Method for Isolating Elastic From Inelastic Deformation in Aquifer Systems: Application to the San Joaquin Valley, CA, *Geophysical Research Letters*, *46*(19), 10,800–10,809, doi:10.1029/2019GL084418.

Chen, C. W., and H. A. Zebker (2000), Network approaches to two-dimensional phase unwrapping: intractability and two new algorithms, *Journal of the Optical Society of America A*, *17*(3), 401–414, doi:10.1364/JOSAA.17.000401.

D'Errico, J. (2005), Surface fitting using gridfit.

Famiglietti, J. S., M. Lo, S. L. Ho, J. Bethune, K. J. Anderson, T. H. Syed, S. C. Swenson, C. R. de Linage, and M. Rodell (2011), Satellites measure recent rates of groundwater depletion in California's Central Valley, *Geophysical Research Letters*, *38*(3), L03,403, doi:10.1029/2010GL046442.

Farr, T. G., P. A. Rosen, E. Caro, R. Crippen, R. Duren, S. Hensley, M. Kobrick, M. Paller, E. Rodriguez, L. Roth, D. Seal, S. Shaffer, J. Shimada, J. Umland, M. Werner, M. Oskin, D. Burbank, and D. Alsdorf (2007), The Shuttle Radar Topography Mission, *Reviews of Geophysics*, *45*(2), RG2004, doi:10.1029/2005RG000183.

Faunt, C. C. (Ed.) (2009), *Groundwater availability of the Central Valley Aquifer, California*, no. 1766 in U.S. Geological Survey professional paper, U.S. Geological Survey, Reston, Va.

Faunt, C. C., M. Sneed, J. Traum, and J. T. Brandt (2016), Water availability and land subsidence in the Central Valley, California, USA, *Hydrogeology Journal*, *24*(3), 675–684, doi:10.1007/s10040-015-1339-x.

Galili, E., and Y. Nir (1993), The submerged Pre-Pottery Neolithic water well of Atlit-Yam, northern Israel, and its palaeoenvironmental implications, *The Holocene*, *3*(3), 265–270, doi:10.1177/095968369300300309.

Hanson, R. T., L. E. Flint, A. L. Flint, M. D. Dettinger, C. C. Faunt, D. Cayan, and W. Schmid (2012), A method for physically based model analysis of conjunctive use in response to potential climate changes, *Water Resources Research*, *48*(6), W00L08, doi:10.1029/2011WR010774.

Herring, T. A., T. I. Melbourne, M. H. Murray, M. A. Floyd, W. M. Szeliga, R. W. King, D. A. Phillips, C. M. Puskas, M. Santillan, and L. Wang (2016), Plate Boundary Observatory and related networks: GPS data analysis methods and geodetic products, *Reviews of Geophysics*, *54*(4), 2016RG000,529, doi:10.1002/2016RG000529.

Howitt, R., D. MacEwan, J. Medellín-Azuara, J. Lund, and D. Sumner (2015), Economic Analysis of the 2015 Drought For California Agriculture, p. 31.

Ireland, R., J. Poland, and F. Riley (1984), Land subsidence in the San Joaquin Valley, California, as of 1980, *USGS Numbered Series 437-l*.

Jasechko, S., and D. Perrone (2020), California's Central Valley Groundwater Wells Run Dry During Recent Drought, *Earth's Future*, *8*(4), e2019EF001,339, doi:https://doi.org/10.1029/2019EF001339.

Kim, K. H., Z. Liu, M. Rodell, H. Beaudoing, E. Massoud, J. Kitchens, M. Dudek, P. Saylor, F. Corcoran, and J. T. Reager (2020), An Evaluation of Remotely Sensed and In Situ Data Sufficiency for SGMA-Scale Groundwater Studies in the Central Valley, California, *JAWRA Journal of the American Water Resources Association*, doi:https://doi.org/10.1111/1752-1688.12898.

Kummu, M., H. de Moel, P. J. Ward, and O. Varis (2011), How Close Do We Live to Water? A Global Analysis of Population Distance to Freshwater Bodies, *PLoS ONE*, *6*(6), doi:10.1371/journal.pone.0020578.

Leake, S. A. (1990), Interbed storage changes and compaction in models of regional groundwater flow, *Water Resources Research*, *26*(9), 1939–1950, doi:10.1029/WR026i009p01939.

Liu, Z., P.-W. Liu, E. Massoud, T. G. Farr, P. Lundgren, and J. S. Famiglietti (2019), Monitoring Groundwater Change in California's Central Valley Using Sentinel-1 and GRACE Observations, *Geosciences*, *9*(10), 436, doi:10.3390/geosciences9100436.

Lund, J. R., J. Medellin-Azuara, J. Durand, and K. Stone (2018), Lessons from California's 2012-2016 drought, *Journal of Water Resources Planning and Management*, *144*(10), 04018,067, doi:10.1061/(ASCE)WR.1943-5452.0000984.

Murray, K. D., and R. B. Lohman (2018), Short-lived pause in Central California subsidence after heavy winter precipitation of 2017, *Science Advances*, *4*(8), eaar8144, doi:10.1126/sciadv.aar8144.

Neely, W. R., A. A. Borsa, and F. Silverii (2020), GInSAR: A cGPS Correction for Enhanced InSAR Time Series, *IEEE Transactions on Geoscience and Remote Sensing*, *58*(1), 136–146, doi:10.1109/TGRS.2019.2934118.

Neely, W. R., A. A. Borsa, J. A. Burney, M. C. Levy, F. Silverii, and M. Sneed (2021), Characterization of Groundwater Recharge and Flow in California's San Joaquin Valley From InSAR-Observed Surface Deformation, *Water Resources Research*, *57*(4), e2020WR028,451, doi:https://doi.org/10.1029/2020WR028451.

Ojha, C., M. Shirzaei, S. Werth, D. F. Argus, and T. G. Farr (2018), Sustained Groundwater Loss in California's Central Valley Exacerbated by Intense Drought Periods, *Water Resources Research*, *54*(7), 4449–4460, doi:10.1029/2017WR022250.

Ojha, C., S. Werth, and M. Shirzaei (2019), Groundwater Loss and Aquifer System Compaction in San Joaquin Valley During 2012–2015 Drought, *Journal of Geophysical Research: Solid Earth*, *124*(3), 3127–3143, doi:10.1029/2018JB016083.

Page, R. W. (1986), *Geology of the Fresh Ground-water Basin of the Central Valley, California: With Texture Maps and Sections*, U.S. Government Printing Office.

Poland, J. F., and G. H. Davis (1969), Land Subsidence Due To Withdrawal Of Fluids, in *Reviews in Engineering Geology*, vol. 2, pp. 187–270, Geological Society of America, doi:10.1130/REG2-p187.

Prats-Iraola, P., R. Scheiber, L. Marotti, S. Wollstadt, and A. Reigber (2012), TOPS Interferometry With TerraSAR-X, *IEEE Transactions on Geoscience and Remote Sensing*, *50*(8), 3179–3188, doi:10.1109/TGRS.2011.2178247.

San Joaquin Valley Drainage Program (1990), A Management Plan For Agricultural Subsurface Drainage and Related Problems on the Westside San Joaquin Valley, *Tech. rep.*, U.S. Department of the Interior and California Resources Agency, Sacramento, CA.

Sandwell, D., R. Mellors, X. Tong, M. Wei, and P. Wessel (2011), Open radar interferometry software for mapping surface Deformation, *Eos, Transactions American Geophysical Union*, *92*(28), 234–234, doi:10.1029/2011EO280002.

Sandwell, D. T., Y. Zeng, Z.-K. Shen, B. Crowell, J. Murray, R. McCaffrey, and X. Xu (2016), The SCEC community geodetic model V1: Horizontal velocity grid, *SCEC Annu. Meeting*.

Scanlon, B. R., R. C. Reedy, D. A. Stonestrom, D. E. Prudic, and K. F. Dennehy (2005), Impact of land use and land cover change on groundwater recharge and quality in the southwestern US, *Global Change Biology*, *11*(10), 1577–1593, doi:10.1111/j.1365-2486.2005.01026.x.

Scanlon, B. R., C. C. Faunt, L. Longuevergne, R. C. Reedy, W. M. Alley, V. L. McGuire, and P. B. McMahon (2012), Groundwater depletion and sustainability of irrigation in the US High Plains and Central Valley, *Proceedings of the National Academy of Sciences*, *109*(24), 9320–9325, doi:10.1073/pnas.1200311109.

Schmidt, D. A., and R. Bürgmann (2003), Time-dependent land uplift and subsidence in the Santa Clara valley, California, from a large interferometric synthetic aperture radar data set, *Journal of Geophysical Research: Solid Earth*, *108*(B9), 2416, doi:10.1029/2002JB002267.

Smith, R. G., R. Knight, J. Chen, J. A. Reeves, H. A. Zebker, T. Farr, and Z. Liu (2017), Estimating the permanent loss of groundwater storage in the southern San Joaquin Valley, California, *Water Resources Research*, *53*(3), 2133–2148, doi:10.1002/2016WR019861.

Terzaghi, K. (1925), Structure and Volume of voids in soils, translated from Erdbaumechanik auf bodenphysikalischer grundlage, in *From Theory to Practice in Soil Mechanics*, John Wiley, New York.

Wang, J., Y. Deng, R. Wang, P. Ma, and H. Lin (2019), A Small-Baseline InSAR Inversion Algorithm Combining a Smoothing Constraint and L_1-Norm Minimization, *IEEE Geoscience and Remote Sensing Letters*, pp. 1–5, doi:10.1109/LGRS.2019.2893422.

Wei, M., and D. T. Sandwell (2010), Decorrelation of L-Band and C-Band Interferometry Over Vegetated Areas in California, *IEEE Transactions on Geoscience and Remote Sensing*, *48*(7), 2942–2952, doi:10.1109/TGRS.2010.2043442.

Weissmann, G. S., G. L. Bennett, and A. L. Lansdale (2005), Factors controlling sequence development on Quaternary fluvial fans, San Joaquin Basin, California, USA, in *Alluvial Fans: Geomorphology, Sedimentology, Dynamics*, vol. 251, pp. 169–186, Geological Society of London.

Williamson, A. K., D. E. Prudic, and L. A. Swain (1989), *Ground-Water Flow in the Central Valley, California: Regional aquifer-system analysis - Central Valley, California*, vol. 1401-D, U.S. Geological Survey Professional Paper.

Yevjevich, V. (1992), Water and Civilization, *Water International*, *17*(4), 163–171, doi:10.1080/02508069208686135.